Compressive Failure Mechanisms in Layered Materials

PhD Thesis Defended in public at Aalborg University (120808)

Sørensen, Kim Dalsten

Publication date:
2008

Document Version
Publisher's PDF, also known as Version of record

Compressive Failure Mechanisms in Layered Materials

PhD Thesis
Defended in public at Aalborg University
(120808)

Kim Dalsten Sørensen

ISSN 1901-7294
DCE Thesis No. 14

AALBORG UNIVERSITY
Department of Civil Engineering

Aalborg University
Department of Civil Engineering
Division of Structural Mechanics

DCE Thesis No. 14

Compressive Failure Mechanisms in Layered Materials

PhD Thesis defended in public at Aalborg University (120808)

by

Kim Dalsten Sørensen

August 2008

Scientific Publications at the Department of Civil Engineering

Technical Reports are published for timely dissemination of research results and scientific work carried out at the Department of Civil Engineering (DCE) at Aalborg University. This medium allows publication of more detailed explanations and results than typically allowed in scientific journals.

Technical Memoranda are produced to enable the preliminary dissemination of scientific work by the personnel of the DCE where such release is deemed to be appropriate. Documents of this kind may be incomplete or temporary versions of papers—or part of continuing work. This should be kept in mind when references are given to publications of this kind.

Contract Reports are produced to report scientific work carried out under contract. Publications of this kind contain confidential matter and are reserved for the sponsors and the DCE. Therefore, Contract Reports are generally not available for public circulation.

Lecture Notes contain material produced by the lecturers at the DCE for educational purposes. This may be scientific notes, lecture books, example problems or manuals for laboratory work, or computer programs developed at the DCE.

Theses are monograms or collections of papers published to report the scientific work carried out at the DCE to obtain a degree as either PhD or Doctor of Technology. The thesis is publicly available after the defence of the degree.

Latest News is published to enable rapid communication of information about scientific work carried out at the DCE. This includes the status of research projects, developments in the laboratories, information about collaborative work and recent research results.

Published 2008 by
Aalborg University
Department of Civil Engineering
Sohngaardsholmsvej 57,
DK-9000 Aalborg, Denmark

Printed in Aalborg at Aalborg University

ISSN 1901-7294
DCE Thesis No. 14

Preface

The present thesis has been written to fulfill the requirements for obtaining the PhD degree. The work was carried out at the Department of Civil Engineering, Aalborg University, Denmark, and the Material Research Department, Risø, Denmark, between November 2004 and June 2008. The PhD project has been financially supported by the Danish Technical Research Council through the project Interface Design of Composite Materials (STVF fund no. 26-03-0160). Supervisors were Dr. techn. Henrik Myhre Jensen and PhD Lars Pilgaard Mikkelsen and I would like to express my gratitude for their qualified guidance. I would also like to thank Filip Westarp, Kristian Holm-Jørgensen and Johan Clausen at Aalborg University for inspiration and valuable discussions.

Finally, I would like to thank my fiancée Emily Taylor for all her support and understanding during the writing of this thesis.

Abstract

Compressive Failure Mechanisms in Layered Materials.

Two important failure modes in fiber reinforced composite materials including layers and laminates occur under loading conditions dominated by compression in the layer direction. These two distinctly different failure modes are

1. buckling driven delamination
2. failure by strain localization into kink bands.

The present thesis falls into two parts dealing with the two failure modes. In the first part of the thesis the effects of system geometry on buckling driven delamination is investigated. Previous work has focused on buckling driven delamination of surface layers on flat substrates or on cylindrical substrates modeling the delamination as an interface fracture mechanical problem. Here attention is directed towards double-curved substrates, which introduces a new non-dimensional combination of geometric parameters. It is shown for a wide range of parameters that by choosing the two non-dimensional parameters suitably, one of them plays a very insignificant role on the fracture mechanical parameters such as normalized energy release rate and mode mixity, which has obvious impact on the presentation of the results. In some cases, the local curvatures of the system is so high compared to the extent of the delamination that it may be better modeled as a sharp corner. The effects of sharp corners on buckling driven delamination have been studied and are shown to have a significant effect on the fracture mechanical parameters. One effect of the substrate corner is a decreased range of parameters for which the interface crack remains open and as a consequence a study of the effects of crack closure has been carried out.

The other part of the thesis analyzes failure by kink band formation. More specifically a constitutive model developed to study kink band formation has been implemented into the finite element code ABAQUS. The analysis focuses on the performance of ABAQUS in terms of reliability and rate of convergence. Good agreement with previously obtained results is demonstrated. The constitutive model has no intrinsic length scale for which

reason the width of the band is mesh dependent. This has some impact on the convergence rate for decreasing mesh size in the load *vs.* end shortening response for a rectangular block of material. Especially in the immediate post critical range the convergence rate may be slow. The capabilities of the model to deal with more complicated structural and geometrical effects are demonstrated by analyzing kink band formation in composite materials where the load and fiber directions are misaligned.

Abstrakt (in Danish)

Skadesmekanismer i lagdelte materialer udsat for kompressionsbelastninger.

To vigtige skadesmekanismer i fiberforstærkede kompositmaterialer herunder lagdelte materialer og laminater forekommer under belastningsforhold, der domineres af trykspændinger i fiberretningen. Disse to skadesmekanismer er

1. bulingsdrevet delaminering
2. skade og brud som følge af tøjningslokalisering i såkaldte kinkbånd.

Denne afhandling falder i to dele som analyserer de to skadesmekanismer. I den første del af afhandlingen studeres effekterne af systemgeometrien på bulingsdrevet delaminering. Tidligere arbejder har fokuseret på bulingsdrevet delaminering af overfladelag på flade substrater eller på cylindriske substrater idet delamineringen er modelleret som et brudmekanisk problem med en revne i en skilleflade. Her fokuseres der på dobbeltkrumme flader, hvilket introducerer en ny dimensionsløs kombination af geometriske parametre. Det vises for et stort område af parametre, at hvis de to dimensionsløse vælges hensigtsmæssigt, har den ene ingen praktisk betydning for de brudmekaniske parametre såsom energifrigørelsesraten og forholdet mellem modus 1 og 2, hvilket har indlysende betydning for præsentation af resultater. I visse tilfælde er den lokale krumning af substratet så stor, sammenlignet med udstrækningen af delamineringen, at den bedre modelleres som et skarpt hjørne. Effekterne af et skarpt hjørne på bulingsdrevet delaminering er studeret og er vist at have væsentlig betydning på de brudmekaniske parametre. En effekt af hjørnet i substratet er et aftagende område for hvilket revnen forbliver åben og som en konsekvens heraf, er betydningen af kontakt mellem brudfladerne undersøgt.

Den anden del af afhandligen analyserer skade ved kinkbåndsdannelse. Mere specifikt, er en konstitutiv model udviklet til at studere kinkbåndsdannelse blevet implementeret i finite element programmet ABAQUS. Analysen fokuserer på resultaterne opnået med ABAQUS i forhold til pålidelighed og konvergenshastighed. God overensstemmelse med tidligere resultater er

opnået. Den konstitutive model har ingen indbygget længdeskala hvorfor bredden af kinkbåndet er netafhængigt. Dette har nogen indflydelse på konvergenshastigheden med aftagende netstørrelse af last-deformationsresponset for en rektangulær blok materiale. Specielt i det umiddelbare postkritiske område kan konvergenshastigheden været noget langsom. Modellens evne til at håndtere mere komplicerede strukturelle og geometriske effekter er demonstreret ved at analysere kinbåndsdannelse i et kompositmateriale, hvor belastnings- og fiberretning er forskellige.

Publications

[P1] Sørensen, K.D. and Jensen, H.M, 2007. *Buckling-driven Delamination in Layered Spherical Shells*, Journal of the Mechanics and Physics of Solids, **56**, 230-240.

[P2] Sørensen, K.D., Jensen, H.M. and Clausen, J., 2008. *Delamination of Compressed Thin Layers at Corners*, accepted for publication in International Journal of Solids and Structures.

[P3] Sørensen, K.D., Mikkelsen, L.P. and Jensen, H.M., 2007. *On the Simulation of Kink Bands in Fiber Reinforced Composites*, Proceedings of the 28th Risø International Symposium on Materials Science, 2007.

[P4] Sørensen, K.D., Mikkelsen, L.P. and Jensen, H.M., 2008. *Implementation of a Constitutive Model in ABAQUS*, manuscript to be submitted.

Contents

Chapter 1

Delamination of Thin Films

1.1 Introduction

Buckling-driven delamination is an important failure mechanism in material combinations where layers of different thickness and different elastic and thermal properties are joined. Examples of such material combinations include turbine engine blades with thermal barrier coatings, sandwich structures where a polymer foam core is bonded to thin cover plates, tools with hard coatings applied for increased wear resistance, material combinations with applications in the electronic industry, and diamond-like coatings on materials for hip joint implants.

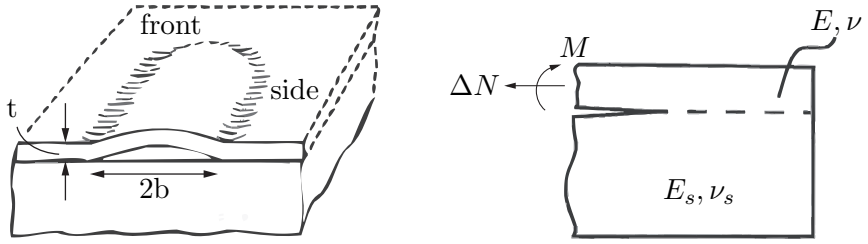

Figure 1.1: Straight sided blister on a plane substrate.

To describe the concept of delamination, consider a system consisting of a thin film attached to a plane substate, as in Fig. 1.1. The thin layer is subject to a uniform, bi-axial compressive stress, σ_0. This stress may be an intrinsic stress from the manufacturing process or thermal stress due to the difference in thermal expansion coefficient. Suppose a small region exists in which the bonding between the two materials is poor or non-existing; if the compressive stress σ_0 exceeds a critical value σ_c, the film will buckle away from the substrate and this buckling will cause the interface crack to be loaded by stresses and moments, as shown in Fig. 1.1. If the combination of these loads lead to an energy release rate that exceeds the fracture toughness

of the interface, the bonding between the thin film and the substrate will break and the delaminated area, or blister, may increase in size.

Many problems concerning propagation of cracks can be treated using the concept of steady-state crack growth, which entails a considerable simplification of the problem, see Kyriakides (1994). Steady-state crack growth implies that the front of the crack assumes a certain shape that remains stationary during propagation, which means that the energy release rate will not depend on the length of the crack or the geometry of the crack front.

Different types of delaminations have been observed, among these the circular blister, the telephone cord blister, and the straight-sided blister. In the present work, the analysis will be restricted to the steady-state propagation of the straight-sided blister, which is characterized by the fact that it grows at one of the ends while the sides remain stationary.

Buckling-driven delamination of thin layers on flat surfaces has previously been studied in a number of works. The mechanism was described initially in Chai *et al.* (1981) with applications to composite plates in mind. Thin film buckling driven delamination was formulated in a fracture mechanics based framework in Evans and Hutchinson (1984). The analysis was based on a combination of plate theory and fracture mechanics treating the boundary between the delaminated and bonded region as a crack front. Results for the energy release rate and stress intensity factors were obtained for circular delaminations at bifurcation and in the post-bifurcation regime. Thin film delamination treated in the framework of interface fracture mechanics taking into account the mixed mode interface fracture toughness of an interface crack was introduced in Jensen *et al.* (1990). The significance of the energy release rate as well as phase angles of loading along the crack front was emphasized. The concept of steady-state propagation of buckling-driven delamination was introduced in Hutchinson and Suo (1992).

Buckling-driven delamination of thin films on curved substrates has been studied to a lesser extent. Hutchinson (2001) initially quantified the effect by studying buckling-driven delamination of a thin film on a cylindrical substrate, while Storåkers and Nilsson (1993) studied the effects of initial geometrical imperfections for the planar case on the energy release rate at buckling driven delamination. The imperfections cause the energy release rate to be non-zero at infinitesimal stresses, as a bifurcation stress does not exist.

In the present work results for delamination from spherical substrates and around sharp corners are presented. The analysis is carried out under the assumptions, that the size of the delaminated area is large relative to the thickness of the film and that there exists a sharp boundary between the delaminated region of the film and the bonded region. As a consequence of these assumptions the boundary between the film and the bonded region can be treated as an interface crack and the stresses in the delaminated region can be obtained from the theory of thin shells.

1.2 Fracture Mechanics

In this section a summary of the theory of fracture mechanics will be presented. For a more detailed description, see Hutchinson and Suo (1992).

A crack in a homogenous material subject to the three different loading modes is shown in Fig. 1.2 and crack tip conventions are shown in Fig. 1.3. The stress field at a crack tip is given by

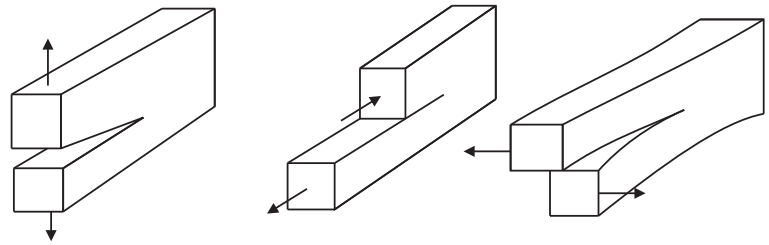

Figure 1.2: The three loading modes.

$$\sigma_{ij}(r,\theta) = \frac{1}{\sqrt{2\pi r}}\left(K_I\sigma_{ij}^{I}(\theta) + K_{II}\sigma_{ij}^{II}(\theta) + K_{III}\sigma_{ij}^{III}(\theta)\right) \tag{1.1}$$

where K_I, K_{II} and K_{III} are the stress intensity factors. This expression is derived from the biharmonic equation which Airy's stress function must satisfy.

In the following only situations where $K_{III} = 0$ will be considered, i.e. all loadings are combinations of mode I and II. The measure of mode II to mode I loading, the phase angle ψ, is defined by

$$\psi = \arctan\left(\frac{K_{II}}{K_I}\right) \tag{1.2}$$

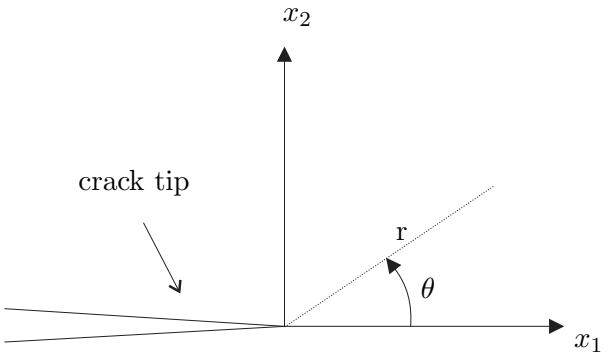

Figure 1.3: Crack tip.

The relative displacements of the crack faces is given by

$$(u_1, u_2) = \left(4/\bar{E}\right) \sqrt{\frac{2r}{\pi}} \left(K_{II}, K_I\right) \tag{1.3}$$

where E is Young's modulus and

$$\begin{aligned} \bar{E} &= E \quad / \left(1 - \nu^2\right) \quad \text{(plane strain)} \\ \bar{E} &= E \qquad \text{(plane stress)} \end{aligned} \tag{1.4}$$

The relation between the energy release rate G and the stress intensity factors is given by Irwin's relation

$$G = \left(K_I^2 + K_{II}^2\right) / \bar{E} \tag{1.5}$$

Irwin's relation results from combining the definition of the energy release rate G with the asymptotic expressions for the stress state and displacement state at the crack tip, and integration of the resulting expression

$$G = \lim_{x \to 0} \frac{1}{2x} \int \left(\sigma_{22}\left(r\right) u_2\left(x - r\right) + \sigma_{12}\left(r\right) u_1\left(x - r\right)\right) \mathrm{d}r \tag{1.6}$$

Consider an interface where two isotropic, linear elastic materials are joined along the x_1-axis as shown in Fig. 1.4, where μ_i, E_i and ν_i $(i = 1, 2)$ denote the shear modulus, Young's modulus and Poisson's ratio of the two materials. Furthermore let $\kappa_i = 3 - 4\nu_i$ for plane strain and $\kappa_i = \left(3 - \nu_i\right) / \left(1 + \nu_i\right)$ for plane stress.

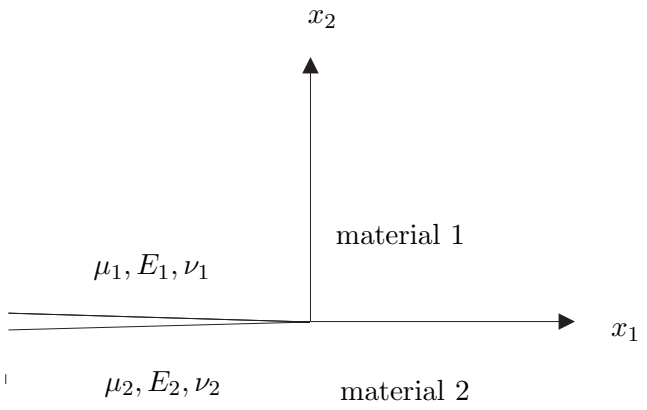

Figure 1.4: Interface crack.

Dundurs' parameters are

$$\alpha = \frac{\mu_1\left(\kappa_2 + 1\right) - \mu_2\left(\kappa_1 + 1\right)}{\mu_1\left(\kappa_2 + 1\right) + \mu_2\left(\kappa_1 + 1\right)} \text{ and } \beta = \frac{\mu_1\left(\kappa_2 - 1\right) - \mu_2\left(\kappa_1 - 1\right)}{\mu_1\left(\kappa_2 + 1\right) + \mu_2\left(\kappa_1 + 1\right)} \tag{1.7}$$

Dundurs' parameters are dimensionless combinations of the elastic moduli and it was shown in Dundurs (1969) that many problems depend on only two parameters rather than three, for instance ν_1, ν_2 and E_1/E_2. An alternative expression for α is

$$\alpha = \frac{\bar{E}_1 - \bar{E}_2}{\bar{E}_1 + \bar{E}_2} \tag{1.8}$$

From this expression it is evident that $-1 < \alpha < 1$. Furthermore α and β both vanish when the two materials are identical. The crack tip stresses are given by

$$\sigma_{22} + i\sigma_{12} = \frac{1}{\sqrt{2\pi r}} \left(K_I + iK_{II}\right) r^{i\varepsilon} \tag{1.9}$$

or

$$\sigma_{22} = \frac{1}{\sqrt{2\pi r}} \Re\big(K r^{i\varepsilon}\big) \text{ and } \sigma_{12} = \frac{1}{\sqrt{2\pi r}} \Im\big(K r^{i\varepsilon}\big) \tag{1.10}$$

where $K = K_I + iK_{II}$ is the complex interface stress intensity factor, and the bimaterial index is

$$\varepsilon = \frac{1}{2\pi} \ln\left(\frac{1-\beta}{1+\beta}\right) \tag{1.11}$$

The relative displacements of the crack flanks close to crack tip are

$$u_2 + iu_1 = \frac{1}{(1+2i\varepsilon)\cosh(\pi\varepsilon)} \frac{4Kr^{i\varepsilon}}{E_*} \sqrt{\frac{2r}{\pi}} \tag{1.12}$$

where

$$\frac{1}{E_*} = \frac{1}{2}\left(\frac{1}{\bar{E}_1} + \frac{1}{\bar{E}_2}\right) \tag{1.13}$$

The energy release rate for crack advance, see Malyshev and Salganik (1965), is

$$G = \frac{\left(1-\beta^2\right)}{E_*} \left(K_I^2 + K_{II}^2\right) \tag{1.14}$$

which reduces to (1.5) when the two materials are identical.

Consider a crack in a layered material where the edges are loaded as shown in Fig. 1.5 with forces and moments per unit width. For a system like this the following results are obtained from simple beam theory. The position of the neutral axis is Δh from the bottom, where

$$\Delta = \frac{1 + 2\Sigma\eta + \Sigma\eta^2}{2\eta\left(1 + \Sigma\eta\right)} \tag{1.15}$$

and

$$\Sigma \equiv \frac{\bar{E}_1}{\bar{E}_2} = \frac{1+\alpha}{1-\alpha} \text{ and } \eta = \frac{h}{H} \tag{1.16}$$

The energy release rate is obtained by calculating the difference in strain energy ahead of and behind the crack tip,

$$G = \frac{1}{2\bar{E}_1}\left(\frac{P_1^2}{h} + 12\frac{M_1^2}{h^3}\right) + \frac{1}{2\bar{E}_2}\left(\frac{P_2^2}{H} + 12\frac{M_2^2}{H^3} - \frac{P_3^2}{Ah} - \frac{M_3^2}{Ih^3}\right) \tag{1.17}$$

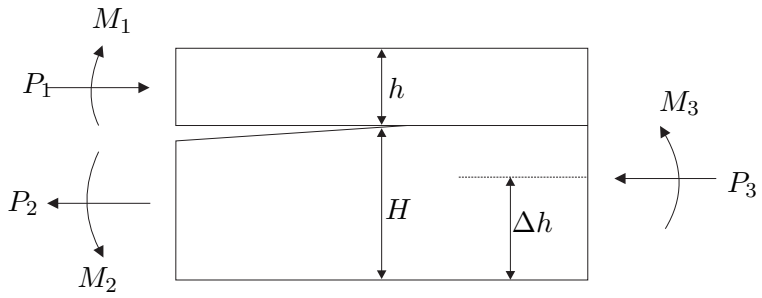

Figure 1.5: Crack in a layered material.

where the dimensionless cross-section A and moment of inertia I are

$$A = \frac{1}{\eta} + \Sigma \tag{1.18}$$

and

$$I = \Sigma \left[\left(\Delta - \frac{1}{\eta} \right)^2 - \left(\Delta - \frac{1}{\eta} \right) + \frac{1}{3} \right] + \frac{\Delta}{\eta} \left(\Delta - \frac{1}{\eta} \right) + \frac{1}{3\eta^3} \tag{1.19}$$

The expression for G can also be calculated from the J-integral.

The complex stress intensity factor is

$$K = h^{-i\varepsilon} \left(\frac{1-\alpha}{1-\beta^2} \right)^{1/2} \left(\frac{P}{\sqrt{2hU}} - ie^{i\gamma} \frac{M}{\sqrt{2h^3 V}} \right) e^{i\omega} \tag{1.20}$$

where P and M are linear combinations of the edge loads

$$P = P_1 - C_1 P_3 - C_2 \frac{M_3}{h} \tag{1.21}$$

and

$$M = M_1 - C_3 M_3 \tag{1.22}$$

The geometric factors are

$$C_1 = \frac{\Sigma}{A} \quad , \quad C_2 = \frac{\Sigma}{I} \left(\frac{1}{\eta} + \frac{1}{2} - \Delta \right) \quad , \; C_3 = \frac{\Sigma}{12I} \tag{1.23}$$

and

$$\frac{1}{U} = 1 + \Sigma\eta \left(4 + 6\eta + 3\eta^2 \right), \quad \frac{1}{V} = 12 \left(1 + \Sigma\eta^3 \right), \quad \frac{\sin\gamma}{\sqrt{UV}} = 6\Sigma\eta^2 \left(1 + \eta \right) \tag{1.24}$$

In (1.20), ω is a function tabulated in Suo and Hutchinson (1990). For no elastic mismatch, i.e. $\alpha = \beta = 0$, a good approximation is $\omega \approx 52.1^\circ - 3^\circ\eta$. In the following only systems consisting of thin films attached to thick layers

will be considered, i.e. $h << H$. By letting $\eta = 0$ in the above equations we get

$$G = \frac{P_1^2}{2\bar{E}_1 h} + \frac{6M_1^2}{\bar{E}_1 h^3} \tag{1.25}$$

and

$$\tan\psi \equiv \frac{\Im\left(Kh^{i\varepsilon}\right)}{\Re\left(Kh^{i\varepsilon}\right)} = \frac{\sqrt{12}M_1 + hP_1\tan\omega}{-\sqrt{12}M_1\tan\omega + hP_1} \tag{1.26}$$

and furthermore, $\omega = 52.1^\circ$ which will be used in the following numerical calculations.

1.3 Shell Theory

This section contains a review of the shell theory as described by Niordson (1985). In the following, subscripts and superscripts denote covariant and contravariant indices respectively and the summation convention is adopted. For a detailed description of concepts from tensor analysis, see Borisenko and Tarapov (1979).

In a cartesian coordinate system the middle surface of a shell is given by the functions

$$x^i = f^i\left(u^1, u^2\right) \tag{1.27}$$

where u^α are coordinates on the surface. The partial derivatives $f^i_{,1}$ and $f^i_{,2}$ are tangent vectors to the coordinate curves of the surface and the metric tensor of the surface is

$$a_{\alpha\beta} = f^i_{,\alpha} f^i_{,\beta} \tag{1.28}$$

The normal vector to the middle surface is given by

$$X^i = \frac{1}{\sqrt{a}} e_{ijk} f^j_{,1} f^k_{,2} \tag{1.29}$$

where a is the determinant of the metric tensor and e_{ijk} is the permutation tensor. Defined this way, the normal vector X^i will be a unit vector. The tensor of curvature of the surface is

$$d_{\alpha\beta} = X^i f^i_{,\alpha\beta} \tag{1.30}$$

It follows immediately from the definitions that the metric tensor $a_{\alpha\beta}$ and the tensor of curvature $d_{\alpha\beta}$ are symmetrical.

The deformation of the middle surface is described by the displacement vector

$$\overline{v}^i = f^i_{,\alpha} v^\alpha + X^i w \tag{1.31}$$

i.e., $v^\alpha\left(u^1, u^2\right)$ are the displacements in the direction of the tangents and $w\left(u^1, u^2\right)$ is the displacement in the direction of the normal.

In the following we will use the Donnell-Mushtari-Vlasov (DMV) theory in which the approximate expressions for the strain-displacement relations are

$$E_{\alpha\beta} = \tfrac{1}{2}\left(D_\alpha v_\beta + D_\beta v_\alpha\right) - d_{\alpha\beta} w + \tfrac{1}{2} D_\alpha w D_\beta w \tag{1.32}$$

and

$$K_{\alpha\beta} = D_\alpha D_\beta w \tag{1.33}$$

where D_α denotes covariant differentiation. The DMV theory is based on the assumptions that the tangential displacements v^α are small compared to the normal displacement w, the wavelength of the deformation is small compared to the smallest principal radius of curvature and the deformation gradients are small.

The stress state in the shell is described by an effective force and an effective moment acting on the middle surface of the shell. These quantities are represented by the two symmetrical tensors, the effective membrane stress tensor $N^{\alpha\beta}$ and the effective moment tensor $M^{\alpha\beta}$.

The two in-plane equilibrium equations are given by

$$D_\alpha N^{\alpha\beta} = 0 \tag{1.34}$$

and the out-of-plane equilibrium equation is

$$D_\alpha D_\beta M^{\alpha\beta} - \left(d_{\alpha\beta} + K_{\alpha\beta}\right) N^{\alpha\beta} = 0 \tag{1.35}$$

These equations result from the application of the principle of virtual work to an arbitrary part of the shell.

The linear elastic constitutive relations are

$$N^{\alpha\beta} = \frac{Et}{1-\nu^2}\left[\left(1-\nu\right) E^{\alpha\beta} + \nu a^{\alpha\beta} E^\gamma_\gamma\right] \tag{1.36}$$

and

$$M^{\alpha\beta} = D\left[\left(1-\nu\right) K^{\alpha\beta} + \nu a^{\alpha\beta} K^\gamma_\gamma\right] \tag{1.37}$$

where the bending stiffness D is given by

$$D = \frac{Et^3}{12\left(1-\nu^2\right)} \tag{1.38}$$

and the strain-energy density is

$$\begin{aligned} W &= \frac{1}{2Et}\left[\left(1+\nu\right) N^\beta_\alpha N^\alpha_\beta - \nu N^\alpha_\alpha N^\beta_\beta\right] \\ &\quad + \frac{Et^3}{24\left(1-\nu^2\right)}\left[\left(1-\nu\right) K^\beta_\alpha K^\alpha_\beta + \nu K^\alpha_\alpha K^\beta_\beta\right] \end{aligned} \tag{1.39}$$

Along a given curve the normal vector is n^α which is a unit vector, i.e. $a_{\alpha\beta} n^\alpha n^\beta = a^{\alpha\beta} n_\alpha n_\beta = 1$. Along a boundary with normal vector n^α the force

is $N = N^{\alpha\beta} n_\alpha n_\beta$ and the moment $M = M^{\alpha\beta} n_\alpha n_\beta$. With the application of the shell theory in mind, the constitutive equations (1.36) are modified so that the undeformed shell is subject to a bi-axial prestress, $-\sigma_0$, i.e. the effective force is

$$N = N^{\alpha\beta} n_\alpha n_\beta = -\sigma_0 t \tag{1.40}$$

from where

$$N^{\alpha\beta} = -a^{\alpha\beta}\sigma_0 t \tag{1.41}$$

The modified constitutive relations (1.36) due to residual stress then become

$$N^{\alpha\beta} = \frac{Et}{1-\nu^2}\left[(1-\nu)\, E^{\alpha\beta} + \nu a^{\alpha\beta} E^{\gamma}_{\gamma}\right] - a^{\alpha\beta}\sigma_0 t \tag{1.42}$$

or

$$N^{\alpha\beta} = \Delta N^{\alpha\beta} - a^{\alpha\beta}\sigma_0 t \tag{1.43}$$

1.4 Summary of Results

This section contains results for delamination in layered spherical shells and at corners as presented in the papers [P1] and [P2]. In addition, some basic results from delamination from a plane substrate, see Hutchinson and Suo (1992), will be given.

1.4.1 Delamination From a Plane Substrate

A straight-sided blister on a plane surface is shown in Fig. 1.1. Before any buckling of the film occurs, the film is subject to a bi-axial stress $\sigma_{11} = \sigma_{22} = -\sigma_0$ and the stress intensity factors at the crack front are zero. When the pre-stress exceeds a critical value σ_c, buckling occurs and the complex stress intensity factor (1.20) will be a function of the local bending moment M and the change of resulting stress ΔN. The energy release rate along the sides of the blister is

$$G = \frac{\left(1-\nu^2\right) t}{2E}\, \sigma_0^2 \left(1 - \frac{\sigma_c}{\sigma_0}\right)\left(1 + 3\frac{\sigma_c}{\sigma_0}\right) \tag{1.44}$$

where

$$\sigma_c = \frac{\pi^2 D}{b^2 t} \tag{1.45}$$

is the classical buckling load of a clamped-clamped plate of width $2b$. If b_0 denotes the half-width at which buckling occurs when the pre-stress is σ_0 we find

$$\frac{\sigma_0}{\sigma_c} = \left(\frac{b}{b_0}\right)^2 \tag{1.46}$$

For large values of σ_0/σ_c, G approaches

$$G_0 \equiv \frac{\left(1-\nu^2\right) t}{2E}\ \sigma_0^2 \tag{1.47}$$

The amplitude of buckling deflection ξ, defined so that the deflection in the middle of the blister, $w\left(0\right) = \xi t$, is

$$\xi = \left[\frac{4}{3}\left(\frac{\sigma_0}{\sigma_c} - 1\right)\right]^{\frac{1}{2}} \tag{1.48}$$

and the phase angle (1.26) is

$$\tan\psi = \frac{4\cos\omega + \sqrt{3}\ \xi \sin\omega}{-4\sin\omega + \sqrt{3}\ \xi\cos\omega} \tag{1.49}$$

The steady-state energy release rate is found by calculating the difference in energy density in front of and behind the crack front,

$$G_{ss} = \frac{1}{b}\int_0^b \left(W_2 - W_1\right) \mathrm{d}y \tag{1.50}$$

which in case of plane substrate yields

$$G_{ss} = \left(1 - \frac{\sigma_c}{\sigma_0}\right)^2 G_0 \tag{1.51}$$

From (1.25) and (1.47) the normalized energy release rate under plane strain conditions is

$$\frac{G}{G_0} = \left(\frac{\Delta N}{\sigma_0 t}\right)^2 + 12\left(\frac{M}{\sigma_0 t^2}\right)^2 \tag{1.52}$$

which will be used in the following sections.

1.4.2 Spherical Surface

In paper [P1] it is shown that the equilibrium equations (1.34) and (1.35) for the case of the spherical surface, see Fig. 1.6, lead to two coupled differential equations which can be integrated numerically to find the displacements v and w.

From the strain-displacement relations (1.32) and (1.33) the strains are determined and stresses and moments can then be calculated from the linear elastic constitutive relations (1.36) and (1.37). Once the stresses and moments are determined the energy release rates along the sides and at the front together with the phase angle can be found from (1.25), (1.50) and (1.26), respectively.

In Fig. 1.7 the variation of the energy release rate along the sides of the delamination is shown for four different values of η where the results

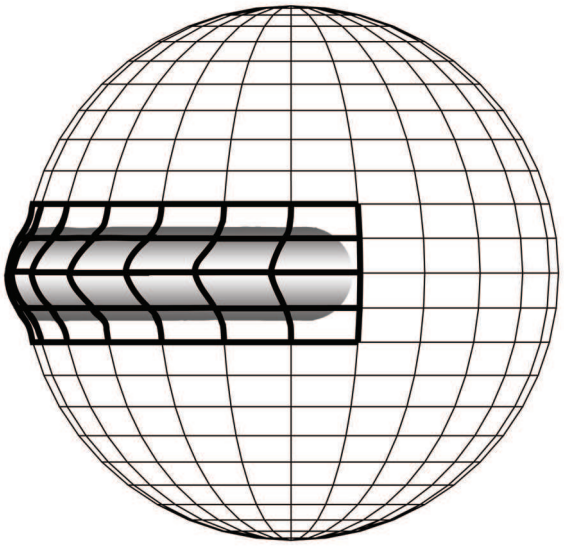

Figure 1.6: Delamination on a spherical surface.

for $\eta = 0$ correspond to the planar case. An essential difference between results obtained for curved substrates and planar substrates is that the energy release rate is zero in the planar case until the bifurcation point is reached at $b = b_0$. Curvature of the substrate acts in a way similar to a geometrical imperfection, by triggering out-of-plane deformations of the delaminated area for infinitesimal stresses. This results in effective bending moments and membrane forces along the crack front and thus finite values of the energy release rate. Included in Fig. 1.7 for comparison are the results for the cylindrical case, see Hutchinson (2001), for $\eta = 1$. By comparison of the results for the cylinder and the sphere, one can see that the shape of the shell has a significant influence especially at low levels of residual stress. As a consequence, the results for the cylindrical shell do not quantify the effect of substrate curvature on buckling-driven delamination, i.e. the shape of the substrate has profound influence on the energy release rate especially at relatively low stress levels. However, the dimensionless combination of geometrical parameters $\eta = b^2/(Rt)$, which is the only combination entering the equilibrium equations for the cylinder, is also shown to be the most significant combination for the sphere. As the value of the parameter η is increased, the peak value of the energy release rate increases and the peak shifts towards smaller stress levels.

In Fig. 1.8 the variation of the phase angle of loading, ψ, calculated numerically by 1.26 is shown. It is a characteristic feature for buckling-driven delamination that the phase angle of loading along the sides of the crack

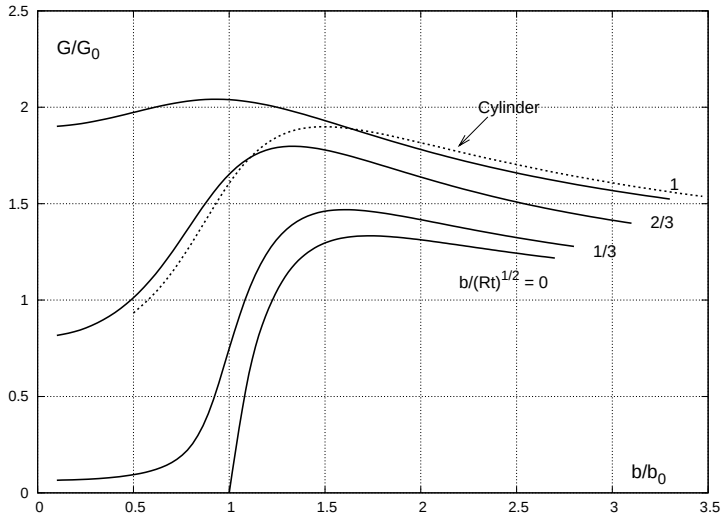

Figure 1.7: Normalized energy release rate along the sides of the delaminated region as a function of residual stress level for different values of $\eta = b^2/(Rt)$. Results for a cylindrical substrate for $\eta = 1$ is included for comparison.

front becomes increasingly more mode II dominated. At a characteristic stress, the crack tip loading becomes purely mode II, i.e. $\psi = -90°$. The curves in Fig. 1.7 are terminated at the transition to pure mode II loading since large-scale crack face contact occurs beyond that point, which is not taken into account in the present analysis. Qualitatively the trends in these curves are similar to the trends observed for a cylindrical substrate. Again as for the results in Fig. 1.7 for the energy release rate, the largest deviations between the spherical, the planar and the cylindrical cases occur at the smallest stress levels. However at larger stress levels deviations become smaller. Effects of the phase angle of loading are most pronounced as the crack tip loading becomes mode II dominated, see Jensen *et al.* (1990). As a consequence, less influence of substrate curvature on mixed mode interface fracture toughness effects is observed than the direct influence of curvature on the energy release rate in Fig. 1.7. For the results presented in Fig. 1.8, an assumption regarding the value of the angle ω appearing in (1.26) has to be made, which in turn depends on the elastic mismatch in the system through the Dundurs' parameters (1.7). All other results presented are independent of the elastic mismatch. As stated in Section 1.2, ω has been tabulated in Suo and Hutchinson (1990). The variation of ω is rather modest, typically it varies in the range $45° < \omega < 65°$. Here, $\omega = 52.1°$ is assumed corresponding, for instance, to the case of no elastic mismatch.

In Fig. 1.9, the steady-state energy release rate along the propagating part of the interface crack is shown as a function of residual stresses. The

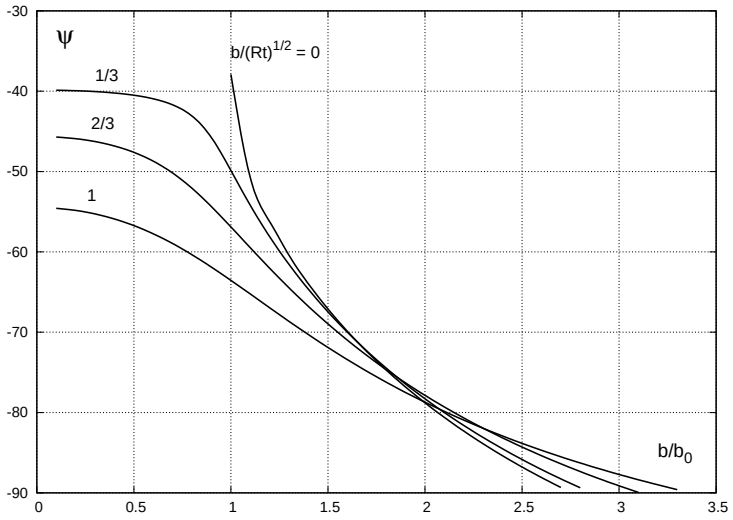

Figure 1.8: Variation of phase angle of loading along the sides of the delaminated region as a function of residual stress level for different values of $\eta = b^2/(Rt)$.

results are obtained by numerical integration of (1.50), which only requires knowledge of states far in front and far behind the propagating front. As a consequence, details such as the shape of the propagating part of the crack front cannot be resolved. These details were studied in Jensen and Sheinman (2001) by a complete finite element modeling of the delaminated region for a planar substrate. The effect of substrate curvature is considerably more pronounced than for the cylindrical case studied in Hutchinson (2001). At the value $\eta = 1$, the energy release rate at small stress levels is almost a factor of 3 higher for the spherical than the cylindrical case, thus making a spherical shell much more prone to buckling driven delamination.

1.4.3 Corner delamination

The geometry of the corner delamination is sketched in Fig. 1.10. From the governing differential equations and boundary conditions the deflection w is found to be

$$\frac{w(y)}{t} = \eta\left(\frac{1-\cos(\pi\sqrt{n})}{\pi\sqrt{n}\sin(\pi\sqrt{n})}\left(1-\cos\left(\frac{\pi\sqrt{n}y}{b}\right)\right)+\frac{1}{\pi\sqrt{n}}\sin\left(\frac{\pi\sqrt{n}y}{b}\right)-\frac{y}{b}\right) \tag{1.53}$$

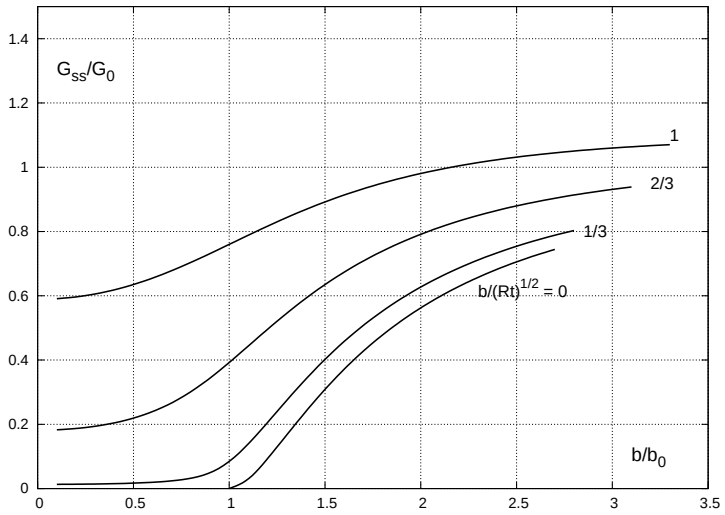

Figure 1.9: Normalized steady state energy release rate along the propagating front of the delamination as a function of residual stress level for different values of $\eta = b^2/(Rt)$.

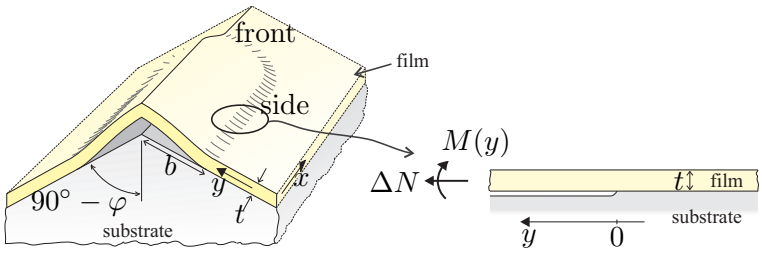

Figure 1.10: Sketch of problem analyzed. A thin layer covering a substrate with a sharp corner fails by buckling driven delamination. The sides and the front of the delaminated region are indicated.

where the following non-dimensional combinations have been introduced

$$\begin{aligned} \eta &= \frac{b}{t}\tan\varphi \\ \frac{n}{s} &= -\frac{N_{22}}{\sigma_0 t} \\ s &= \frac{\sigma_0}{\sigma_c} = \left(\frac{b}{b_0}\right)^2 \end{aligned} \tag{1.54}$$

Here, b_0 denotes the half-width of the flat layer when buckling initially occurs for a fixed residual stress, σ_0. The buckling stress for a clamped flat plate of width $2b$ is given by

$$\sigma_c = \frac{\pi^2 E t^2}{12\left(1-\nu^2\right)b^2} \tag{1.55}$$

From the governing equations the following expressions are derived. The parameter n is calculated from the implicit equation

$$\frac{n}{s} = 1 - \frac{6}{\pi^2 s}\eta^2 \frac{\sin\left(\pi\sqrt{n}\right) - \pi\sqrt{n}\cos\left(\pi\sqrt{n}\right)}{\pi\sqrt{n}\left(1+\cos\left(\pi\sqrt{n}\right)\right)} \tag{1.56}$$

and change of stress and moment are found from

$$\frac{\Delta N}{\sigma_0 t} = 1 - \frac{n}{s} \tag{1.57}$$

and

$$\frac{M}{\sigma_0 t^2} = \frac{\eta}{\pi^2 s}\frac{\pi\sqrt{n}\left(1-\cos\left(\pi\sqrt{n}\right)\right)}{\sin\left(\pi\sqrt{n}\right)} \tag{1.58}$$

The steady-state energy release rate is

$$\frac{G_{ss}}{G_0} = 1 - \left(\frac{n}{s}\right)^2 - \frac{12\eta^2}{\pi^4 s^2}\frac{\pi\sqrt{n}}{1+\cos\left(\pi\sqrt{n}\right)}\left(\pi\sqrt{n} - \sin\left(\pi\sqrt{n}\right)\right) \tag{1.59}$$

The results for G, ψ and G_{ss} are shown in figures 1.11, 1.12 and 1.13, respectively, for different values of the angle φ and $\eta = 10$. When φ is zero, the problem corresponds to delamination on a flat substrate, where the stress in the layer has to exceed the critical value, σ_c, before any deflection of the layer can occur. When φ assumes a non-zero value, the problem is no longer a bifurcation problem and solutions exist for stresses below the critical stress for buckling of a plate, σ_c. It is important to emphasize that the two sets of curves for G and G_{ss} in Figs. 1.11 and 1.13 correspond to different mode mixities. It is noted that the mode mixity along the front is considerably lower than along the crack sides, that the crack tip along the propagating front never closes, and that crack closure occurs corresponding to $\psi = -90^\circ$ along the sides. By Fig. 1.12, it is clear that the angle φ has a pronounced influence on the mode mixity especially on the conditions for crack closure.

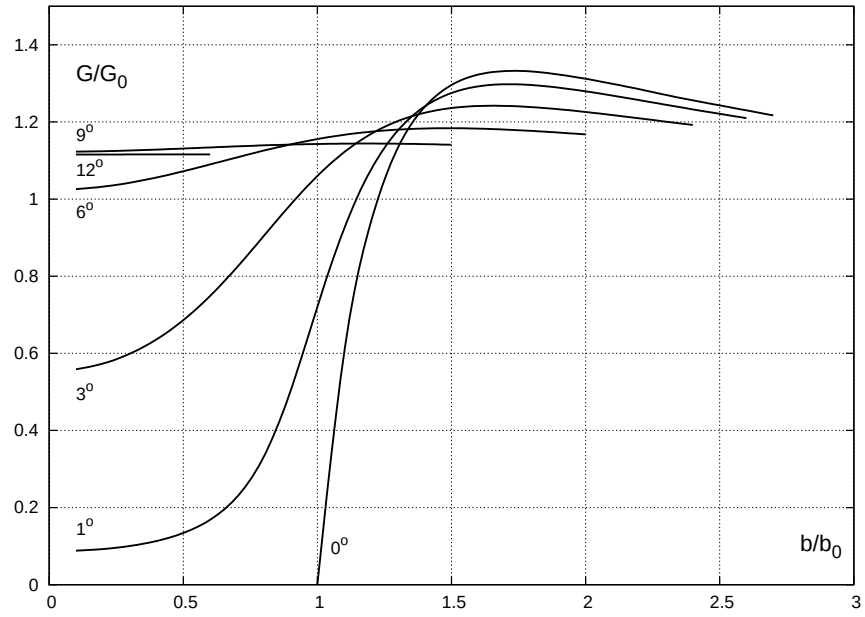

Figure 1.11: Energy release rate at the sides of the delaminated region as a function of the delamination width. Substrate is subject to uniform strain.

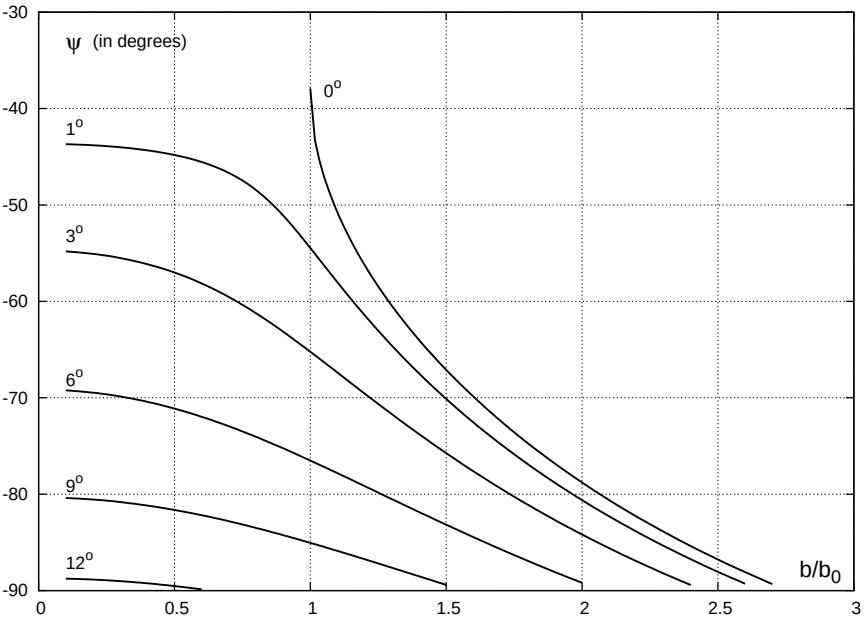

Figure 1.12: Mode mixity along the sides of the delaminated region and the front using the results for a full circular delamination. Substrate is subject to uniform strain.

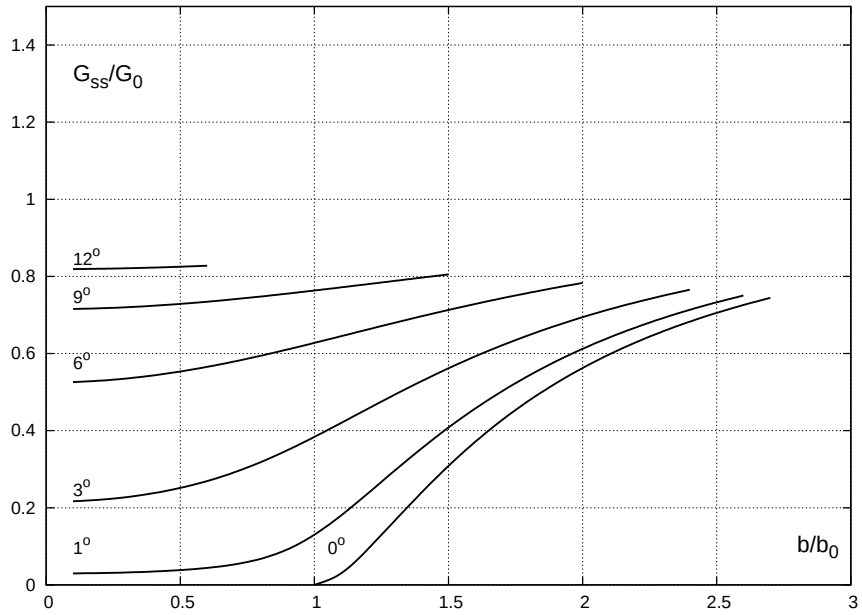

Figure 1.13: Energy release rate along the front of the delaminated region.

The results in Figs. 1.11 - 1.13 are valid for other combinations of the angle φ and the crack length b/t provided the value of η in (1.54) is the same.

A mixed mode fracture criterion prior to crack closure has been invoked by introducing the criterion in Jensen *et al.* (1990)

$$G = G_c \left(1 - (\lambda_2 - 1)\sin^2\psi\right)^{-1} \tag{1.60}$$

where the factor λ_2 adjusts the relative contribution of mode 2 to the fracture criterion. Experimental support for the fracture criterion may be found in Cao and Evans (1989), Jensen *et al.* (1990) and Liechti and Chai (1991). A discussion of the relation between the fracture criterion (1.60) and detailed micro-mechanical models of contact and friction along the crack faces may be found in Evans and Hutchinson (1989) and Jensen (1990). Specifically, the parameter λ_2 could be associated with microscopic parameters for the interface such as the height and angle of surface asperities, coefficient of friction etc. In Tvergaard and Hutchinson (1993) it was shown that also plastic deformation in the layers can explain the mode dependent interface fracture toughness. The effect of imposing a mixed mode interface fracture criterion prior to crack closure will be demonstrated after introduction of an exact asymptotic expression for the fracture mechanical parameters. In the limit $\sigma_0/\sigma_c \to 0$ the expressions for the energy release rates along the sides, G, and along the propagating front, G_{ss}, and the mode mixity at the sides,

ψ, can be obtained in closed form as

$$\frac{G}{G_0} = \frac{\eta^2\left(3+\eta^2\right)}{\left(1+\eta^2\right)^2},\ \frac{G_{ss}}{G_0} = \frac{\eta^2}{1+\eta^2},\ \tan\psi = \frac{\eta\tan\omega+\sqrt{3}}{\eta-\sqrt{3}\tan\omega} \tag{1.61}$$

which are used in paper [P2] to illustrate effects of contacting crack faces. The ratio b/t has to exceed some specified value, say 5, for the shell solutions to be reasonably accurate, which for specific values of φ restricts how small η can be. By (1.61) it is seen that the mode mixity exceeds -90° indicating that the crack faces are in contact over distances comparable to the layer thickness if the crack length exceeds a critical value

$$\frac{b}{t} \geq \frac{\sqrt{3}\tan\omega}{\tan\varphi} \tag{1.62}$$

Whether this critical value is in the range where the shell solution is valid depends both on the elastic mismatch and the angle φ.

1.5 Discussion

In the papers [P1] and [P2] buckling-driven delamination on a spherical surface and at a sharp corner has been analyzed. The analysis was carried out by considering initial delamination and steady-state propagation of a narrow layer bonded to a substrate. The delaminated layer propagates in a self-similar fashion along the crack front leaving behind unloaded crack faces. In the analysis the boundary between the delaminated region and the substrate was treated as an interface crack front, which is loaded under mixed mode conditions. Small-scale yielding conditions and small-scale contact of the crack faces at the crack front were assumed.

For the spherical surface, results for the energy release rate and phase angle of loading along the sides of the delaminated region and the energy release rate for steady-state delamination were compared to results from the literature for delamination of thin films on planar and cylindrical substrates. The major effect of substrate curvature for the cylindrical substrate compared to the planar substrate is that it acts in a way much similar to the effect of geometrical imperfections in the sense that normal deflections and crack driving forces can be present for any small residual stress state in the film. In the planar case, the crack driving force is zero until a bifurcation point is passed. Delamination growth will take place in the post-buckling regime provided it occurs at all. For the case of a curved substrate there is a bifurcation point only in the case where the film is applied to the inside of the substrate so that contact between the film and the substrate prevents the film from deflecting to the side it would naturally deflect if it was applied to the outside of the substrate.

The effects of a double curved substrate, such as the spherical substrate, compared to the cylindrical substrate is that an additional non-dimensional combination of geometrical parameters enters the formulation. It has been shown that this additional combination of geometrical parameters play a minor role on the energy release rate and phase angle of loading for the range of parameters considered here. This result is believed to be key to the present study since this implies, for any doubly curved substrate, that the non-dimensional combination of geometrical parameters identified for the cylindrical substrate is the only parameter required in addition to material parameters when mapping the energy release rate and the phase angle of loading.

In the case of corner delamination, when the corner angle φ is zero, the problem corresponds to delamination on a flat substrate, where the stress in the layer has to exceed a certain critical value before any deflection of the layer can occur and thus result in loading of the crack front. When φ assumes a non-zero value, the problem is no longer a bifurcation problem and solutions exist for stresses below the critical load for a plate. Semi-analytical results for the energy release rate and the mode mixity along the crack front have been obtained by coupling the theory of thin shells to elastic interface fracture mechanics. The results require numerical solution of an implicit equation. Solutions are verified by comparing to pure numerical results using an incremental loading scheme. It has also been checked that bifurcation into non-symmetric deformations at the corner are not expected.

It has been shown that mode dependent interface fracture toughness can explain the existence of steady state delamination.

Chapter 2

Kink Band Formation

2.1 Introduction

Kink band formation in fiber reinforced composite materials is the subject of the papers [P3] and [P4].

Failure by kinking in fiber reinforced composites has been the subject of a number of recent investigations. It has been found that the compressive failure strength is considerably lower than the tensile strength, typically in the order of 50 to 60 percent for carbon fiber composites (Kyriakides *et al.* (1995)). It has also been found that the compressive strength is governed by plastic yielding in the matrix (Budiansky (1983)), and furthermore, that small misalignments of the fibers have a large influence on the compressive strength, see Kyriakides *et al.* (1995). Several investigations of compression of a fiber reinforced material under the assumption of perfectly aligned fibers have predicted bifurcations stresses much higher than results obtained from experiments. Liu *et al.* (2004) include the effect of random waviness of the fibers using a Cosserat smeared-out finite element model.

In Kyriakides *et al.* (1995) the problem of predicting compressive strength for fiber reinforced materials is approached through an idealized model composite, with individual discretization of fiber and matrix material, and this two-dimensional micro-mechanical model was later extended to a three dimensional model in Hsu *et al.* (1998). In these investigations the post-buckling response is also studied, and it is shown that deformation localizes into well-defined bands of bent fibers.

Kink band formation in fiber reinforced materials was investigated in Christoffersen and Jensen (1996) and in Jensen and Christoffersen (1997), where a plane constitutive model for perfectly bonded layered materials was introduced. It was found that this model contains essentially the same information in one point of the material as a complete finite element discretization of a representative volume element, like the model introduced in Kyriakides

et al. (1995), and furthermore, that the critical stress is highly influenced by fiber volume fraction and the constitutive behavior of the constituents. Another conclusion is that the kink stress is reduced by taking non-linearity of the fibers into account compared to the predicted critical stress assuming linear elastic fibers.

In the present study, a smeared-out plane constitutive model, as formulated by Christoffersen and Jensen (1996), is implemented as a user subroutine in the finite element program ABAQUS. Effects of fiber misalignment for elastic and plastic response are studied, and qualitatively compared to earlier results.

2.2 A Plane Constitutive Model for Fiber Reinforced Composites

The constitutive relations are formulated as the relation between nominal stress rates and displacement gradient $v_{i,j}$ (with a comma denoting partial differentiation) in the form

$$\dot{s}_{ij} = C_{ijkl} v_{l,k}, \quad i,\ j,\ k,\ l \in \{1,2\} \tag{2.1}$$

The following relations hold between L_{ijkl} and C_{ijkl}

$$L_{ijkl} = C_{ijkl} + \tfrac{1}{2}\delta_{il}\sigma_{kj} + \tfrac{1}{2}\delta_{ik}\sigma_{lj} + \tfrac{1}{2}\sigma_{il}\delta_{kj} - \tfrac{1}{2}\sigma_{ik}\delta_{lj}, \quad i,\ j,\ k,\ l \in \{1,2\} \tag{2.2}$$

where σ_{ij} denotes the Cauchy stress tensor and L_{ijkl} denotes the tensor of instantaneous moduli. The constitutive equations (2.1) are written in the following alternative notation

$$\dot{\boldsymbol{s}}_\alpha = \boldsymbol{C}_{\alpha\beta} \boldsymbol{v}_{,\beta}, \quad \alpha, \beta \in \{1,2\} \tag{2.3}$$

so that the vectors $\dot{\boldsymbol{s}}_\alpha$ and $\boldsymbol{v}$ contain the components of the nominal stress rates and the displacements according to

$$\dot{\boldsymbol{s}}_1 = \begin{pmatrix} \dot{s}_{11} \\ \dot{s}_{12} \end{pmatrix} \quad , \quad \dot{\boldsymbol{s}}_2 = \begin{pmatrix} \dot{s}_{21} \\ \dot{s}_{22} \end{pmatrix} \quad , \quad \boldsymbol{v} = \begin{pmatrix} v_1 \\ v_2 \end{pmatrix} \tag{2.4}$$

and the matrices $\boldsymbol{C}_{\alpha\beta}$ are given by

$$\begin{aligned} \boldsymbol{C}_{11} &= \begin{pmatrix} C_{1111} & C_{1112} \\ C_{1211} & C_{1212} \end{pmatrix} \quad \boldsymbol{C}_{12} = \begin{pmatrix} C_{1121} & C_{1122} \\ C_{1221} & C_{1222} \end{pmatrix} \\ \boldsymbol{C}_{21} &= \begin{pmatrix} C_{2111} & C_{2112} \\ C_{2211} & C_{2212} \end{pmatrix} \quad \boldsymbol{C}_{22} = \begin{pmatrix} C_{2121} & C_{2122} \\ C_{2221} & C_{2222} \end{pmatrix} \end{aligned} \tag{2.5}$$

It was shown in Christoffersen and Jensen (1996) that the composite moduli can be written in the form

$$\boldsymbol{C}_{\alpha\beta} = c^f \boldsymbol{C}^f_{\alpha\beta} + c^m \boldsymbol{C}^m_{\alpha\beta} - c^f c^m \left(\boldsymbol{C}^f_{\alpha 2} - \boldsymbol{C}^m_{\alpha 2} \right) \boldsymbol{C}^{*-1}_{22} \left(\boldsymbol{C}^f_{2\beta} - \boldsymbol{C}^m_{2\beta} \right) \tag{2.6}$$

where

$$\boldsymbol{C}_{22}^{*} = \left(c^m \boldsymbol{C}_{22}^{f} + c^f \boldsymbol{C}_{22}^{m} \right) \tag{2.7}$$

Each constituent may now be described by arbitrary time-independent plasticity theories. Here, J_2-flow theory is used to model the behavior of both the fibers and the matrix material. Experimental results in Kyriakides *et al.* (1995) showed indications of relative weak fiber nonlinearities. The effects of this were investigated in Jensen and Christoffersen (1997) showing some influence on the critical stress for kink band initiation. The J_2-flow theory for the matrix can be formulated as the following incrementally linear relation between Jaumann rates of Kirchhoff stresses and strains (McMeeking and Rice (1975))

$$\begin{aligned} \hat{\tau}_{ij} &= L_{ijkl}\varepsilon_{kl} \\ L_{ijkl} &= G\left(\delta_{ik}\delta_{jl} + \delta_{il}\delta_{jk}\right) + \left(K - \tfrac{2}{3}G\right)\delta_{ij}\delta_{kl} - \tfrac{4}{3}\left(G - G_t\right) m_{ij} m_{kl} \end{aligned} \tag{2.8}$$

where superscript $()^m$ for the matrix has been omitted and δ_{ij} denotes the Kronecker delta. In (2.8), G and K are the elastic shear modulus and bulk modulus and G_t is the shear tangent modulus, which along with m_{ij} are given by

$$G = \frac{E}{2\left(1+\nu\right)} \quad , \quad K = \frac{E}{3\left(1-2\nu\right)} \quad , \quad \frac{1}{G_t} = \frac{3}{E_t} - \frac{1-2\nu}{E} \tag{2.9}$$

and

$$m_{ij} = \frac{1}{2\sigma_{eq}} \left(\sigma_{ij} - \frac{1}{3}\delta_{ij}\sigma_{kk} \right) \tag{2.10}$$

Here, E_t is the uniaxial tangent modulus, which requires a uniaxial true stress *vs.* logarithmic strain to be specified. This is given by

$$\epsilon = \begin{cases} \dfrac{\sigma}{E} & , \ \sigma \leq \sigma_y \\ \dfrac{\sigma_y}{E}\left[\dfrac{1}{n}\left(\dfrac{\sigma}{\sigma_y} \right)^n - \dfrac{1}{n} + 1 \right] & , \ \sigma > \sigma_y \end{cases} \tag{2.11}$$

Furthermore, in (2.9) the effective von Mises' stress is given by

$$\sigma_{eq} = \sqrt{\frac{3}{2}\sigma_{ij}\sigma_{ij} - \frac{1}{2}\sigma_{ii}\sigma_{jj}} \tag{2.12}$$

2.3 ABAQUS Implementation

The subroutine UMAT (User MATerial) is written in FORTRAN and is used to define the constitutive behavior of a material. ABAQUS provides the deformation gradient, total strains and strain increments and the subroutine

must then return the material Jacobian matrix $\partial\Delta\sigma/\partial\Delta\varepsilon$ for the constitutive model along with updated stresses. In this case the material behavior of the composite is simulated by mixing the properties of 2 materials each described by a power-hardening law.

The UMAT subroutine used in the present work contains the following steps:

1. Calculate the gradient of velocity from deformation gradient. The deformation gradient F is provided by ABAQUS and the velocity gradient, which describes the spatial rate of the velocity, is found from $v_{i,j} = \dot{F}_{ik}F^{-1}_{kj}$
2. Calculate the effective von Mises' stress for matrix and fiber according to (2.12)
3. Calculate tangent modulus from the uniaxial true stress *vs.* logarithmic strain curve, see (2.11)
4. Calculate L^f_{ijkl} and L^m_{ijkl} according to (2.8)
5. Calculate C_{ijkl} from (2.2) and (2.6)
6. Calculate stress increments, see Jensen and Christoffersen (1997)

$$\dot{\sigma_{ij}} = C_{ijkl}v_{l,k} - \sigma_{ij}v_{k,k} + v_{i,k}\sigma_{kj} \tag{2.13}$$

7. Update stresses
8. Update yield stress
9. Update plastic strains
10. Return state variables, see the following subsection
11. Return material Jacobian matrix $\partial\Delta\sigma/\partial\Delta\varepsilon$

All variables are updated using a forward Euler procedure.

The solution-dependent variables are variables that are updated as the analysis progresses. For instance, in order to be able to return the material Jacobian and to update the overall stresses in the composite material, it is necessary to keep track of the individual stresses in the fiber and matrix material. The UMAT subroutine utilizes a total of 16 state variables, passed from ABAQUS through the array STATEV(NSTATV), each containing information about every integration point. The state variables are:

- The updated yield stresses of the fiber and matrix materials - both modeled as power hardening materials

- The effective plastic strain in fiber and matrix
- β^f and β^m - two variables which will have the value 1 or 0 depending on if the material is yielding or not
- The stresses in the matrix material, σ^m_{11}, σ^m_{22}, σ^m_{33}, σ^m_{12}
- The stresses in the fiber material, σ^f_{11}, σ^f_{22}, σ^f_{33}, σ^f_{12}
- The initial direction of the fibers and the current rotation

To the matrix and fiber material 9 material properties are associated: 2 Young's moduli, E^m and E^f, 2 Poisson's ratios, ν^m and ν^f, 2 initial yield stresses, σ^m_y and σ^f_y, 2 hardening parameters, n^m and n^f and finally the fiber volume fraction c^f. These properties are passed to UMAT by ABAQUS in the array PROPS(NPROPS). In the input file, the keyword *USER MATERIAL is used to specify material constants. In the present study, the fiber volume fraction is assumed to remain constant $c^f = 0.6$ throughout the deformation.

For a more detailed description on how to implement a constitutive model in ABAQUS, see Dunne and Petrinic (2005).

2.4 Summary of Results

This section contains a summary of the results presented in the papers [P3] an [P4].

The kink band geometry is sketched in Fig. 2.1. A block of material is subject to compressive stresses under plane strain conditions. The block has the dimensions height $H = 3$ and length $L = 10$ and in a band of width b and at an angle β the direction of the fibers is given a small imperfection. The direction of the fibers outside the band is given by the angle α and inside the kink band the fibers are assumed to be at an angle ϕ, and this angle is given by the expression

$$\phi\left(x_1, x_2\right) = \tfrac{1}{2}\phi_m \left[\cos\left(\frac{2\pi\cos\beta}{b}\left(x_1 + x_2\tan\beta\right)\right) + 1\right] + \alpha \tag{2.14}$$

so that a small imperfection is added to the fiber angle α inside the band, and ϕ_m is the value of the imperfection in the middle of the kink band. Furthermore, the displacements u_1 and u_2 satisfy the boundary conditions

$$u_1 = 0 \text{ on } x_1 = -\tfrac{L}{2} \tag{2.15}$$

$$u_2 = 0 \text{ on } (x_1, x_2) = \left(-\tfrac{L}{2}, -\tfrac{H}{2}\right) \tag{2.16}$$

In the following, the width of the kink band has the value $b = 2$, and in all simulations the fiber volume fraction is 0.6. Furthermore, analysis has been

restricted to two different fiber/matrix stiffness ratios, $E^f/E^m = 35$ and $E^f/E^m = 100$, which qualitatively correspond to a glass-fiber reinforced polymer and a carbon-fiber reinforced polymer, respectively.

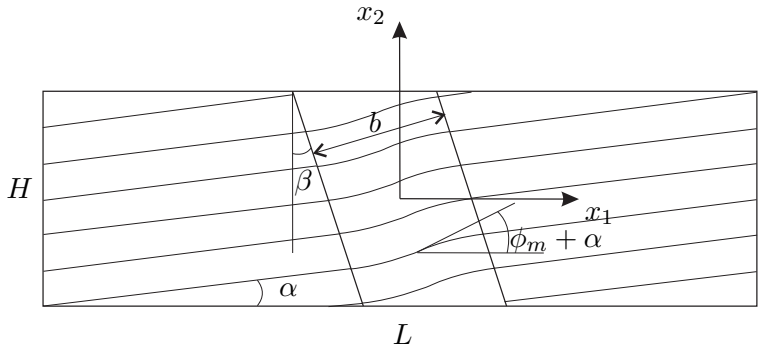

Figure 2.1: Kink band geometry.

In Fig. 2.2 normalized load *vs.* end shortening curves are shown for the low fiber to matrix ratio , i.e. glass fibers and the high ratio, carbon fibers. Calculations are carried out for different values of the fiber imperfection angle ϕ_m and outside the band the fibers are aligned with the x_1-axis, i.e. $\alpha = 0$. As also shown in previous studies, the peak load is highly sensitive to the misalignment of the fibers. At a sufficiently large imperfection angle, the peak load disappears and the composite fails by another mechanism. After the peak load material softening occurs and the curves eventually converge and the previous load history has insignificant effects.

A contour plot of the plastic strain in the kink band for the case $E^f/E^m = 35$ is shown in Fig. 2.3. The figure shows the tendency for strains to localize into a band inclined relative to the load and fiber direction. The deformations remain almost homogeneous outside the localized band.

The peak load is sensitive to a number of parameters. The sensitivity to the misalignment has been demonstrated and the non-linear response of the matrix material can also play a role. In Fig. 2.4, load *vs.* end shortening curves are shown for different values of the hardening exponent n^m for the matrix. The peak stress and the post critical response is seen to be sensitive to the hardening exponent in certain regimes. The peak stress as a function of the hardening exponent n^m is shown in Fig. 2.5, where the peak load initially drops by a large amount until convergence towards an elastic-perfectly plastic response of the matrix is achieved. Critical load as a function of n^m is shown in Fig. 2.5 for the misalignment angle $\phi_m = 3°$.

The peak load is less sensitive to the kink band inclination angle, β. In Fig. 2.6, the critical load as a function of β is shown for three different misalignment angles. The peak stress is seen to vary only moderately with the angle, β, while the angle ϕ_m plays a more significant role.

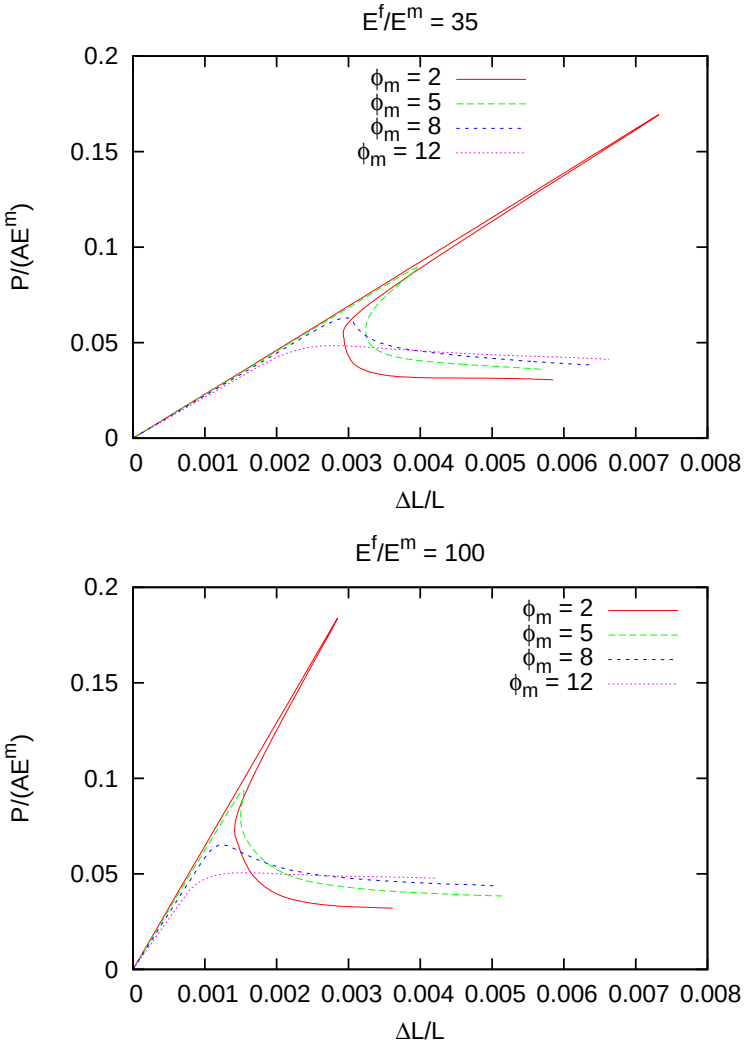

Figure 2.2: Plastic deformation, kink band formation.

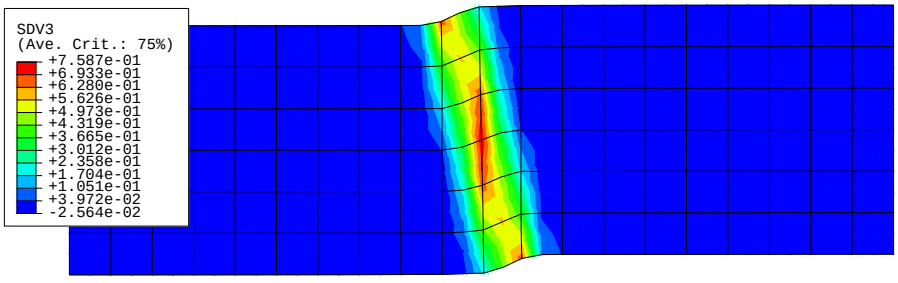

Figure 2.3: Contour plot of plastic strain.

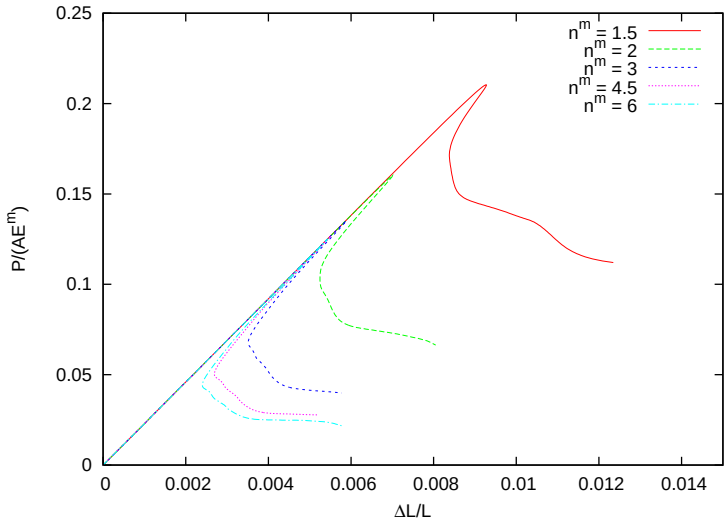

Figure 2.4: Load *vs.* end shortening curves for different values of matrix hardening parameter n^m.

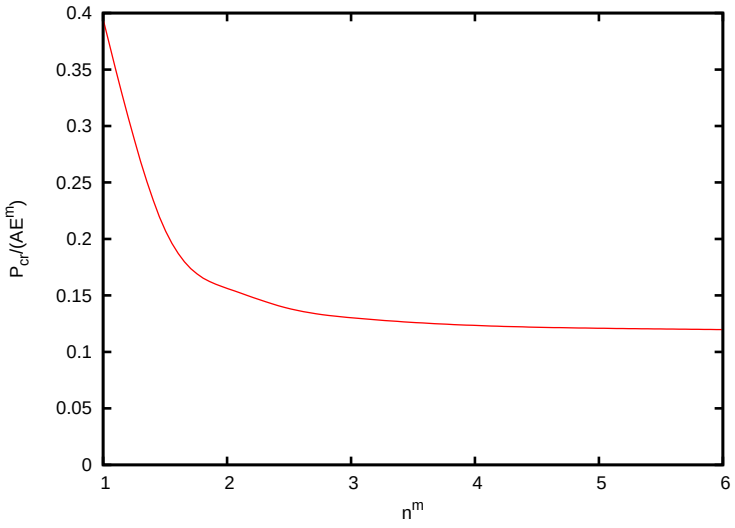

Figure 2.5: Critical load *vs.* n^m.

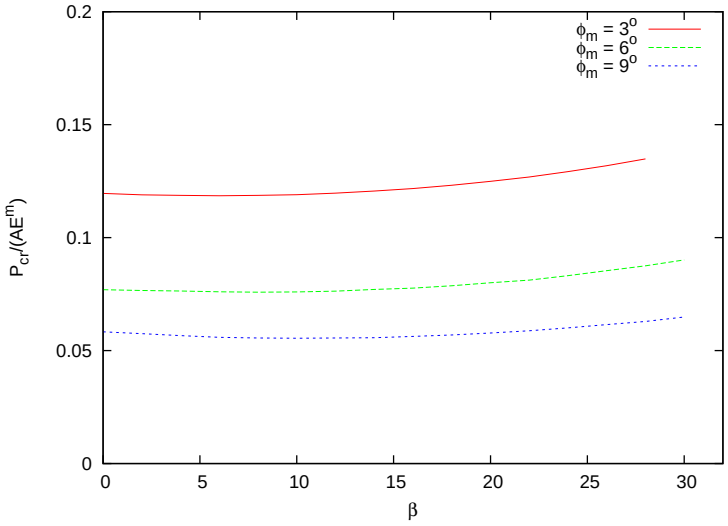

Figure 2.6: Critical load *vs.* β.

The effect of the applied load not being in the same direction as the fibers is studied by changing the value of α. Load-deformation curves for various α are given in Fig. 2.7. It is seen that the snap-back effect only exists for small angles and that the load-deformation curves cease to have a peak value when the value of α increases.

A material length-scale is not included in the implementation of the constitutive model and as a consequence, the width of the kink band is undetermined and mesh dependent. As a result of this, the rate of convergence of load *vs.* end-shortening curves, see Fig. 2.8, with decreasing element size in the mesh is somewhat slow, especially in the immediate post kinking regime. The peak stress and the response far into the post critical regime seem to converge faster.

Fig. 2.9 shows contour plots of the effective plastic strain in the 4 different meshes used in the mesh-dependency studies. It is seen how the width of the localized band decreases as the size of the elements decreases. Up until this point all results have been produced using a mesh consisting of rectangular elements. To investigate how results are affected by a different meshing, a mesh as shown in Fig. 2.10 is introduced. The elements, 12*40 CPE8R elements, are aligned with the initial imperfection at an angle of $\beta = 8°$. The results are shown in Fig. 2.11 and Fig. 2.12 where the load-deformation curves for a 'regular' and a 'distorted' mesh are compared.

In Fig. 2.11 the fiber misalignment angle is $\phi = 4°$ and $E^f/E^m = 35$, in Fig. 2.12 the fiber angle is $\phi = 5°$ and $E^f/E^m = 100$. The critical load is apparently unaffected by the change of the mesh but the immediate post-kinking behavior is seen to be different.

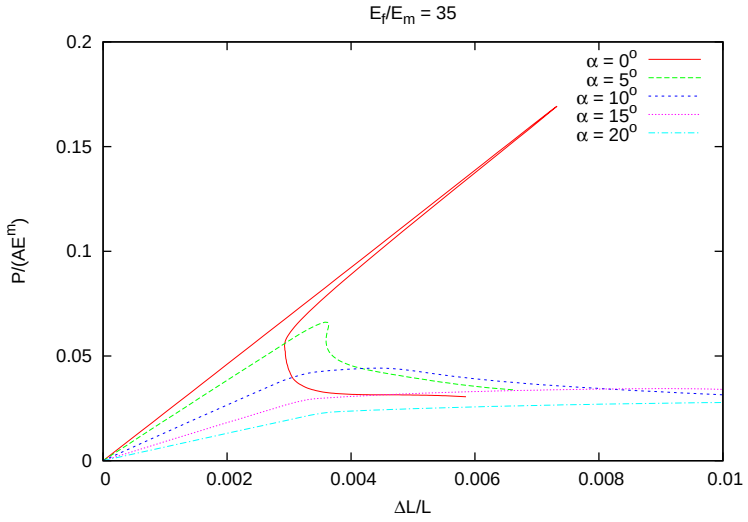

Figure 2.7: Load-deformation curves for various α.

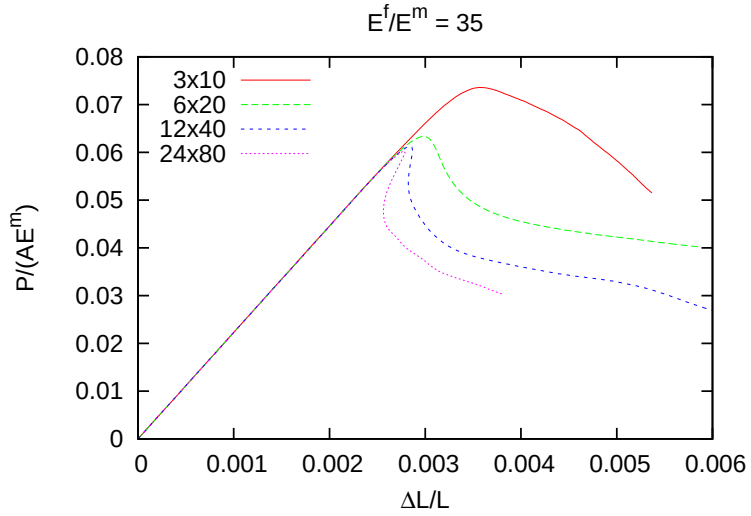

Figure 2.8: Load *vs.* end shortening curves for different element sizes.

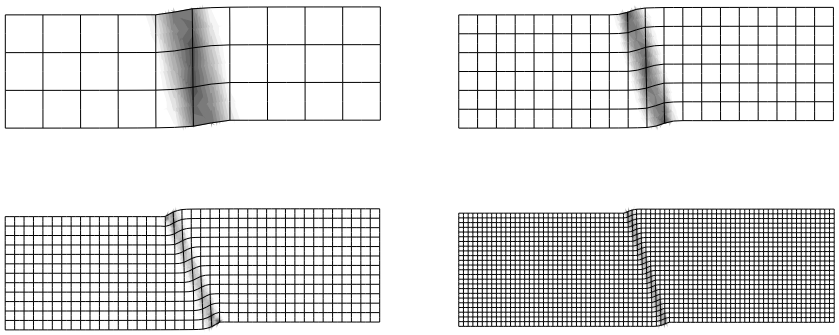

Figure 2.9: Four different deformed meshes with contour plot of effective plastic s

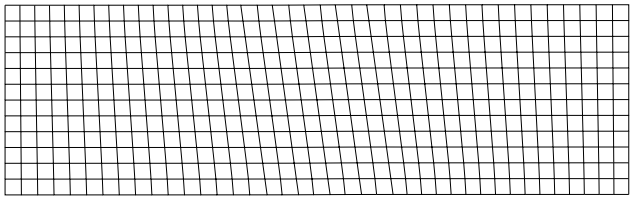

Figure 2.10: 'Distorted' mesh.

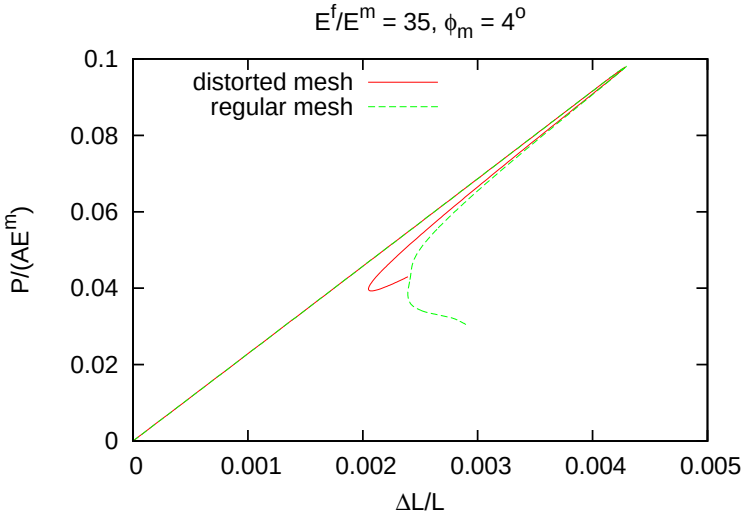

Figure 2.11: Load *vs.* deformation for regular and distorted mesh.

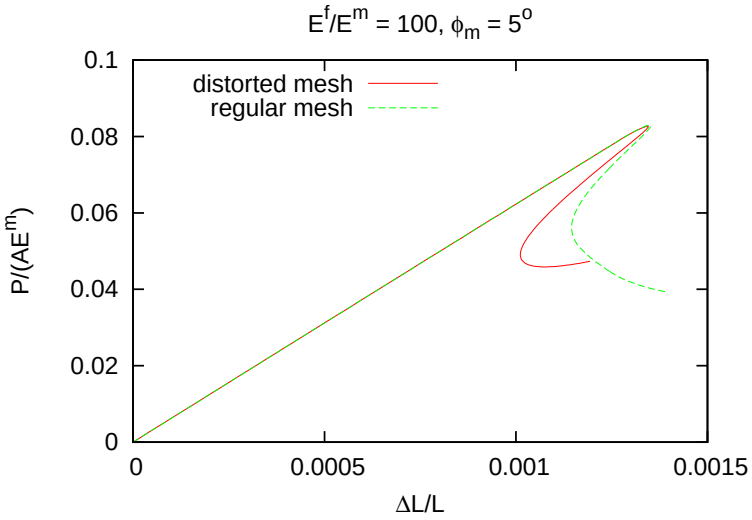

Figure 2.12: Load *vs.* deformation for regular and distorted mesh.

2.5 Discussion

A plane constitutive model for fiber reinforced composites has been implemented in ABAQUS as a user subroutine. The model has been tested under cases where failure by kink band formation is a relevant mechanism. The behavior of a rectangular block of material divided into a number of finite elements is investigated. The focus in this study is on the performance of the model when implemented in ABAQUS with respect to reliability and rate of convergence. In agreement with previous results, it is seen that the critical stress for kink band formation is rather insensitive to the initial kink band orientation and that the kink band undergoes a distinct rotation in the post critical regime. In the model a continuous field may be specified for the initial fiber orientation. This field can vary with the spatial components to mimic real defects in the production of laminated structures. The imperfection of the composite material applied in the present study is an assumed band of material of a specified width in which the fiber orientation gradually changes from the orientation outside the band to a maximum deviation from this and back to the original orientation again. The band may be arbitrarily oriented relative to the fiber direction. No variation of fiber rotations has been assumed in the direction of the band although this is not a general restriction in the model.

The constitutive model has no intrinsic length scale and consequently the width of the kink band is undetermined and mesh dependent. As a result the rate of convergence of load *vs.* end-shortening curves with decreasing finite element mesh size is somewhat slow especially in the immediate post kinking regime. The peak stress and the response far into the post critical

regime seem to converge faster. It is demonstrated that an initial alignment of the finite element mesh in the direction of the orientation of the kink band may have the effect of increasing the rate of convergence.

The model is applied in a study of the effect of initial misalignment of the fiber and load direction. This effect has previously been studied in an approximate manner by imposing a fixed linear combination of compressive and shear stresses out side the kink band. The effect of initial misalignments is very distinct on the peak stress where the critical stress at 10° misalignment is reduced to roughly 1/4 the critical stress for compression in the fiber direction at a fixed band of imperfections. At a misalignment of 15° and above the peak in the stress *vs.* end shortening response vanishes and the composite structure fails by another mechanism.

The model is expected to have some immediate applications such as kink band formation in plates with holes or other more complex structural components. The model can also be used to study competing compressive failure mechanisms such as buckling and kink band formation in fiber composite based structures.

Chapter 3

Conclusion

Two failure modes in compression of layered composite materials were considered: buckling driven delamination and kink band formation.

Effects of substrate curvature on buckling-driven delamination of thin films or layers were studied by considering initial delamination and steady-state propagation of a narrow layer bonded to a spherical substrate. The delaminated layer propagates in a self-similar fashion along the crack front leaving behind unloaded crack faces. The analysis was carried out by treating the boundary between the delaminated region and the substrate as an interface crack front, which is loaded under mixed mode conditions. Small-scale yielding conditions and small-scale contact of the crack faces at the crack front were assumed. Results for the energy release rate and phase angle of loading along the sides of the delaminated region and the energy release rate for steady-state delamination were compared to results from the literature for delamination of thin films on planar and cylindrical substrates. The major effect of substrate curvature for the cylindrical substrate compared to the planar substrate is that it acts in a way much similar to the effect of geometrical imperfections in the sense that normal deflections and crack driving forces can be present for any small residual stress state in the film. In the planar case, the crack driving force is zero until a bifurcation point is passed. Delamination growth will take place in the post-buckling regime provided it occurs at all. For the case of a curved substrate there is no bifurcation point only when the film is applied to the outside. The effects of a double curved substrate, such as the spherical substrate, compared to the cylindrical substrate is that an additional non-dimensional combination of geometrical parameters enters the formulation. It has been shown that this additional combination of geometrical parameters play a minor role on the energy release rate and phase angle of loading for the range of parameters considered here. The shape of the substrate also affects the energy release rate and the phase angle of loading. For the spherical substrate the shape affects the energy release rate most significantly at small values of

normalized residual stress levels where the tendency is that the higher the substrate curvature, the higher the peak value of the energy release rate along the sides of the delamination, and this peak moves towards smaller values of residual stress.

An analysis of buckling driven delamination at a sharp corner was also carried out. Semi-analytical results for the energy release rate and the mode mixity along the crack front have been obtained by coupling the theory of thin shells to elastic interface fracture mechanics. The results require numerical solution of an implicit equation. Solutions are verified by comparing to pure numerical results using an incremental loading scheme. It has also been checked that bifurcation into non-symmetric deformations at the corner are not expected. The energy release rate along the propagating crack front was obtained by an assumed path independent integral leading the crack from an initial state far in front of the propagating front to its final state far behind. The path independence relies on an assumption that the released energy during crack propagation is independent of the loading history bringing the crack from its initial to its final state. Steady state crack propagation along the front compared to crack propagation at the sides takes place for the case where the energy release rate is highest. In the limit of infinitely small stresses, analytical results for the energy release rate and mode mixity along the sides as well as the steady state energy release rate along the front have been obtained. It was been shown that mode dependent interface fracture toughness can explain the existence of steady state delamination. It has been shown that crack closure takes place at sufficient high stress levels like the case for the flat substrate. The analytical results for the fracture mechanical parameters in the limit of small stresses were combined with previously obtained results for the effects of friction between the crack faces when crack closure occurs. By these results it was shown that effects of frictional sliding of the contacting crack faces in these cases can explain a transition in failure mode from crack propagation along the sides to crack propagation along the front. This means that such failure modes may exist also in systems where the fracture criterion prior to crack closure is mode independent.

A plane constitutive model for fiber reinforced composites has been implemented in ABAQUS as a user subroutine. The model has been tested under cases where failure by kink band formation is a relevant mechanism. At first it is verified that the model predicts a reasonable behavior for a single finite element. The behavior of a rectangular block of material divided into a number of finite elements is then investigated. The focus in this study is on the performance of the model when implemented in ABAQUS with respect to reliability and rate of convergence. In agreement with previous results, it is seen that the critical stress for kink band formation is rather insensitive to the initial kink band orientation and that the kink band undergoes a distinct rotation in the post critical regime. In the model, a continuous field may be

specified for the initial fiber orientation. This field can vary with the spatial components to mimic real defects in the production of laminated structures. The imperfection of the composite material applied in the present study is an assumed band of material of a specified width in which the fiber orientation gradually changes from the orientation outside the band to a maximum deviation from this and back to the original orientation again. The band may be arbitrarily oriented relative to the fiber direction. No variation of fiber rotations has been assumed in the direction of the band although this is not a general restriction in the model. The constitutive model has no intrinsic length scale and consequently the width of the kink band is undetermined and mesh dependent. As a result the rate of convergence of load *vs.* end-shortening curves with decreasing finite element mesh size is somewhat slow especially in the immediate post kinking regime. The peak stress and the response far into the post critical regime seem to converge faster. It is demonstrated that an initial alignment of the finite element mesh in the direction of the orientation of the kink band may have the effect of increasing the rate of convergence. The model is expected to have some immediate applications such as kink band formation in plates with holes or other, more complex, structural components. Also, the model can be used to study competing compressive failure mechanisms such as buckling and kink band formation in fiber composite based structures.

Acknowledgements

The work has been financial supported by the Danish Technical Research Counsil through the project 'Interface Design of Composite Materials' (STVF fund no. 26-03-0160).

Bibliography

Borisenko, A.I. and I.E. Tarapov (1979). *Vector and Tensor Analysis with Applications*. Dover Publications, Inc.

Budiansky, B. (1983). Micromechanics. *Computers and Structures* **16**, 3–12.

Cao, H.C. and A.G. Evans (1989). An experimental study of the fracture resistance of bimaterial interface. *Mechanics of Materials* **7**, 295–305.

Chai, H., C.D. Babcock and W.G. Knauss (1981). One dimensional modelling of failure in laminated plates by delamination buckling. *International Journal of Solids and Structures* **17**, 1069–1083.

Christoffersen, J. and H.M. Jensen (1996). Kink band analysis accounting for the microstructure of fiber reinforced materials. *Mechanics of Materials* **24**, 305–315.

Dundurs, J. (1969). Edge-bonded dissimilar orthogonal elastic wedges. *Journal of Applied Mechanics* **36**, 650–652.

Dunne, Fionn and Nik Petrinic (2005). *Introduction to Computational Plasticity*. Oxford University Press.

Evans, A.G. and J.W. Hutchinson (1984). On the mechanics of delamination and spalling in compressed films. *International Journal of Solids and Structures* **20**, 455–466.

Evans, A.G. and J.W. Hutchinson (1989). Effects of non-planarity on the mixed mode fracture resistance of bimaterial interfaces. *Acta Materialia* **37**, 909–916.

Hsu, S.Y., T.J. Vogler and S. Kyriakides (1998). Compressive strength predictions for fiber composites. *Journal of Applied Mechanics* **65**, 7–16.

Hutchinson, J.W. (2001). Delamination of compressed films on curved substrates. *Journal of the Mechanics and Physics of Solids* **49**, 1847–1864.

Hutchinson, J.W. and Z. Suo (1992). Mixed mode cracking in layered materials. *Advances in Applied Mechanics* **29**, 63–191.

Jensen, H.M. (1990). Mixed mode interface fracture criteria. *Acta Metallurgia et Materialia* **38**, 2637–2644.

Jensen, H.M. and J. Christoffersen (1997). Kink band formation in fiber reinforced materials. *Journal of the Mechanics and Physics of Solids* **45**, 1121–1136.

Jensen, H.M., J.W. Hutchinson and K.-S. Kim (1990). Decohesion of a cut prestressed film on a substrate. *International Journal of Solids and Structures* **26**, 1099–1114.

Kyriakides, S. (1994). Propagating instabilities in structures. *Advances in Applied Mechanics* **30**, 67–189.

Kyriakides, S., R. Arseculeratne, E.J. Perry and K.M. Liechti (1995). On the compressive failure of fiber reinforced composites. *International Journal of Solids and Structures* **32**, 689–738.

Liechti, K.M. and Y.-S. Chai (1991). Biaxial loading experiments for determining interfacial fracture toughness. *Journal of Applied Mechanics* **58**, 680–687.

Liu, D., N.A. Fleck and M.P.F. Sutcliffe (2004). Compressive strength of fibre composites with random fibre waviness. *Journal of the Mechanics and Physics of Solids* **52**, 1481–1505.

Malyshev, B.M. and R.L. Salganik (1965). The strength of adhesive joints using the theory of cracks. *International Journal of Fracture* **5**, 114–128.

McMeeking, R.M. and J.R. Rice (1975). Finite-element formulations for problems of large elastic-plastic deformation. *International Journal of Solids and Structures* **11**, 601–616.

Niordson, F. (1985). *Shell Theory*. North-Holland.

Storåkers, B. and K.F. Nilsson (1993). Imperfection sensitivity at delamination buckling and growth. *International Journal of Solids and Structures* **30**, 1057–1074.

Suo, Z. and J.W. Hutchinson (1990). Interface crack between two elastic layers. *International Journal of Fracture* **43**, 1–18.

Tvergaard, V. and J.W. Hutchinson (1993). The influence of plasticity on mixed mode interface toughness. *Journal of the Mechanics and Physics of Solids* **41**, 1119–1135.

Available online at www.sciencedirect.com
ScienceDirect
Journal of the Mechanics and Physics of Solids 56 (2008) 230–240
JOURNAL OF THE MECHANICS AND PHYSICS OF SOLIDS
www.elsevier.com/locate/jmps

Buckling-driven delamination in layered spherical shells

Kim D. Sørensen, Henrik M. Jensen*

Department of Civil Engineering, Aalborg University, DK-9000 Aalborg, Denmark

Received 26 October 2006; received in revised form 15 March 2007; accepted 17 March 2007

Abstract

An analysis of buckling-driven delamination of a layer in a spherical, layered shell has been carried out. The effects of the substrate having a double curvature compared to previous studies of delamination on cylindrical substrates turn out to be non-trivial in the sense that additional to the effect of the shape of the substrate, a new non-dimensional geometrical parameter enters the conditions for steady-state delamination. It is shown that this additional geometrical parameter in most cases of practical relevance has insignificant influence on the fracture mechanical parameters involved for the problem. The consequence is that solutions need to be mapped as a function of one rather than two dimensionless parameters. Furthermore, the shape of the substrate has profound influence especially on initiation of delamination growth.

Keywords: Delamination; Layered materials; Fracture mechanics; Thin shells; Curved substrates

1. Introduction

Buckling-driven delamination is known to be an important failure mechanism in material combinations where layers of different thickness and different elastic and thermal properties are joined. Examples of such material combinations could be turbine engine blades with thermal barrier coatings, sandwich structures where a polymer foam core is bonded to thin cover plates, tools with hard coatings applied for increased wear resistance, material combinations with applications in the electronic industry, and diamond-like-coatings on materials for hip joint implants. In such systems, the substrate may be curved and only little attention has been directed towards studying the effects of substrate curvature on buckling-driven delamination.

Combinations of external loading, intrinsic stresses from the manufacturing process, thermal stresses and stresses developing in corrosive layers at high temperature may lead to large compressive stresses in the layers resulting in buckling and delamination. Typical sites for initiation of delamination are at stress concentrations such as edges and corners or at system defects.

Buckling-driven delamination of compressed thin films or layers on flat substrates has been studied in a number of previous works. The mechanism was described initially in Chai et al. (1981) with applications to composite plates in mind. Thin film buckling-driven delamination was formulated in a fracture mechanics

*Corresponding author. Tel.: +45 9635 8570; fax.: +45 9814 8243.
E-mail address: hmj@civil.aau.dk (H.M. Jensen).

0022-5096/$ - see front matter © 2007 Elsevier Ltd. All rights reserved.
doi:10.1016/j.jmps.2007.03.006

based framework in Evans and Hutchinson (1984). The analysis was based on a combination of plate theory and fracture mechanics treating the boundary between the delaminated and bonded region as a crack front. Results for the energy release rate and stress intensity factors were obtained for circular delaminations at bifurcation and in the post-bifurcation regime. Thin film delamination treated in the framework of interface fracture mechanics taking into account the mixed mode interface fracture toughness of an interface crack was introduced in Jensen et al. (1990). The significance of the energy release rate as well as phase angles of loading along the crack front was emphasised. In Hutchinson and Suo (1992) the concept of steady-state propagation of buckling-driven delamination was introduced. Closed form results for the energy release rate and phase angle of loading were obtained. Various analyses such as Jensen (1993), Ortiz and Gioia (1994), Audoly (1999), Jensen and Sheinman (2001,2002) and Moon et al. (2002) have been devoted to studying the most commonly observed mode of buckling-driven delamination on flat substrates; the so-called 'telephone cord' mode. Two fundamentally different effects may result in a transition from simple to wavy crack front morphology; (i) perturbations of the crack front leading to higher released energy, Hutchinson et al. (1992) or (ii) buckling of the delaminated region resulting in a perturbation of the crack tip loads, Jensen and Thouless (1995). A comprehensive study of buckling-driven delamination involving analyses of morphology can be found in Gioia and Ortiz (1997).

Buckling-driven delamination of thin films on curved substrates has been studied to a lesser extent. Hutchinson (2001) initially quantified the effect by studying buckling-driven delamination of a thin film on a cylindrical substrate, while Storåkers and Nilsson (1993) studied the effects of initial geometrical imperfections for the planar case on the energy release rate at buckling-driven delamination. The imperfections cause the energy release rate to be non-zero at infinitesimal stresses, as a bifurcation stress does not exist. In Hutchinson et al. (2000) the effects of a geometrically imperfect interface on buckling-driven delamination and initiation of delamination were studied. Recent experimental observations of buckling-driven delamination in compressed films on cylindrical substrates in Moon et al. (2006) indicate that the telephone cord mode is also commonly observed in curved thin film systems.

The geometry of the system considered in this work is a spherical layered shell containing a surface layer, which has delaminated. A sketch of the geometry of the problem is presented in Fig. 1 where a surface layer of width $2b$ is indicated by lines of larger thickness. The layer buckles or deflects away from the shell due to a combination of external loads and residual stresses. When the crack front propagates it does so in the equatorial direction leaving behind unloaded crack faces. It is emphasised that the shape of the substrate outside the delaminated region has no influence on the results in the following analysis. Also, the thickness of the shell has no influence on the analysis provided it is larger than the thickness of the delaminated layer. Due to the steady-state nature of buckling-driven delamination, stresses and deformations behind the propagating crack front are independent of the coordinate in the direction of propagation, which will be utilised in the analysis. The shape of the propagating part of the crack front, which is shown in Fig. 1 as if it follows co-ordinate lines on the surface of the sphere, is unknown and does not enter the analysis in the following.

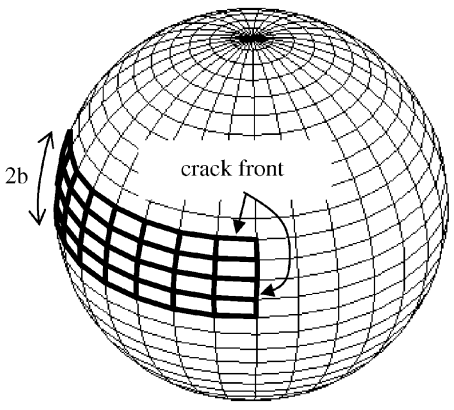

Fig. 1. Sketch of a strip of a delaminated surface layer of width $2b$ in a composite spherical shell. The delamination propagates in the equatorial direction leaving behind unloaded crack sides.

2. Fracture mechanics

The boundary of the delaminated layer in Fig. 1 is treated as an interface crack front both at the part that is propagating and the unloaded crack sides left behind. A basic geometry for the fracture mechanics of the problem consists of a layer of thickness t bonded to a thick substrate. The layer is subject to a local normal membrane force, N, a shear force, T, and an effective bending moment, M, at the boundary between the bonded and the delaminated part of the system. The combined mode I/II and the mode III energy release rate can be obtained by applying the J-integral (Jensen et al., 1990)

$$G = \mathrm{G}_{\mathrm{I/II}} + G_{\mathrm{III}}, \quad G_{\mathrm{I/II}} = \frac{1-\nu^2}{2Et^3}(12M^2 + t^2N^2), \quad \mathrm{G}_{\mathrm{III}} = \frac{1}{2\mu t}T^2. \tag{1}$$

Here, E, ν and μ are Young's modulus, the Poisson ratio and the elastic shear modulus of the film. The separation of the energy release rate into mode I, II and III stress intensity factors (K_{I}, K_{II} and K_{III}) is done via the phase angles of loading ψ and ϕ introduced in Suo and Hutchinson (1990) and Jensen et al. (1990):

$$\tan\psi = \frac{\mathrm{Im}((K_{\mathrm{I}} + \mathrm{i}K_{\mathrm{II}})t^{\mathrm{i}\varepsilon_{\mathrm{b}}})}{\mathrm{Re}((K_{\mathrm{I}} + \mathrm{i}K_{\mathrm{II}})t^{\mathrm{i}\varepsilon_{\mathrm{b}}})} = \frac{\sqrt{12}M\cos\omega + tN\sin\omega}{-\sqrt{12}M\sin\omega + tN\cos\omega},$$
$$\cos\phi = \sqrt{\frac{G_{\mathrm{III}}}{G}}. \tag{2}$$

The in-plane crack tip fields governed by K_{I} and K_{II} are coupled due to the oscillating crack tip singularity. In the definition of the phase angle ψ in (2), $\tan\psi$ is given as the ratio of shear to normal stress a distance t ahead of the crack tip. The angle ω is tabulated in Suo and Hutchinson (1990) as a function of the Dundurs (1969) parameters α and β:

$$\alpha = \frac{\bar{E} - \bar{E}_{\mathrm{s}}}{\bar{E} + \bar{E}_{\mathrm{s}}}, \quad 2\beta = \frac{\mu(1-2\nu_{\mathrm{s}}) - \mu_{\mathrm{s}}(1-2\nu)}{\mu(1+\nu_{\mathrm{s}}) + \mu_{\mathrm{s}}(1+\nu)}, \tag{3}$$

where subscript $()_{\mathrm{s}}$ refers to the substrate and $\bar{E} = E/(1-\nu^2)$. In (2) the bi-material index, ε_{b}, is defined by

$$\varepsilon_{\mathrm{b}} = \frac{1}{2\pi}\ln\left(\frac{1-\beta}{1+\beta}\right). \tag{4}$$

The relationship between energy release rate and stress intensity factors is given by the Irwin relation evaluated by the work done by stresses on opening the crack faces

$$G = (1-\beta^2)\frac{K_{\mathrm{I}}^2 + K_{\mathrm{II}}^2}{2}\left(\frac{1}{\bar{E}} + \frac{1}{\bar{E}_{\mathrm{s}}}\right) + \frac{K_{\mathrm{III}}^2}{4}\left(\frac{1}{\mu} + \frac{1}{\mu_{\mathrm{s}}}\right). \tag{5}$$

The family of interface fracture criteria formulated in Jensen et al. (1990) can be written as

$$G\Gamma_{\mathrm{c}}(\psi,\phi) = G_{\mathrm{Ic}}, \tag{6}$$

where G_{Ic} is the mode I toughness, and $\Gamma_{\mathrm{c}}(\psi,\phi)$ is the toughness function $\Gamma_{\mathrm{c}}(0,\pi/2) = 1$. If the toughness function is identical to 1, Eq. (6) reduces to the Griffith fracture criterion, but otherwise it takes effects of small-scale plasticity and crack face contact into account. As an alternative to this approach, the mixed mode fracture toughness could be obtained by a detailed micromechanical analysis accounting for crack face contact and frictional sliding (Evans and Hutchinson, 1989) or crack tip plasticity (Tvergaard and Hutchinson, 1993).

The calculation of energy release rates for cracks propagating under steady-state conditions can be carried out in a simplified formulation when it is utilised that the stresses and deformations behind the propagating front are independent of the coordinate in which direction, the front propagates.

3. Shell theory

Stresses and deformations in the delaminated region are found by treating this as a thin shell clamped to the substrate along the crack front. The shell theory described by Niordson (1985) is reviewed in the

following where a subscript denotes a covariant index, a superscript denotes a contravariant index and repeated indices denote summation. In a Cartesian coordinate system, x^i, the mid-surface of the shell is described by

$$x^i = f^i(u^1, u^2), \tag{7}$$

where u^α are the surface coordinates. The displacements, $\bar{v}^i$, in the Cartesian coordinate system are written in terms of in-plane displacements, v^α, and the normal displacement, w, for the mid-surface according to the Kirchhoff–Love hypothesis

$$\bar{v}^i = f^i_{,\alpha} v^\alpha + X^i w, \tag{8}$$

where a comma denotes partial differentiation with respect to u^α , and X^i are the Cartesian components of the surface normal vector. The in-plane equilibrium equations are given as

$$D_\alpha N^{\alpha\beta} = 0, \tag{9}$$

where D_α denotes covariant differentiation and $N^{\alpha\beta}$ are the contravariant components of the membrane stress tensor. The out-of-plane equilibrium equation is given by

$$D_\alpha D_\beta M^{\alpha\beta} - (d_{\alpha\beta} + K_{\alpha\beta}) N^{\alpha\beta} = 0, \tag{10}$$

where $M^{\alpha\beta}$ are the components of the tensor of bending moments, $d_{\alpha\beta}$ is the curvature tensor and $K_{\alpha\beta}$ is the bending strain tensor.

The strain energy density is given by

$$W = \frac{Et}{2(1-\nu^2)}[(1-\nu)E^\beta_\alpha E^\alpha_\beta + \nu E^\alpha_\alpha E^\beta_\beta] + \frac{Et^3}{24(1-\nu^2)}[(1-\nu)K^\beta_\alpha K^\alpha_\beta + \nu K^\alpha_\alpha K^\beta_\beta]. \tag{11}$$

The components of the mid-surface in-plane strain and bending strain tensors, $E_{\alpha\beta}$ and $K_{\alpha\beta}$, are related to the membrane stresses and the bending moments by

$$N^{\alpha\beta} = \frac{Et}{1-\nu^2}[(1-\nu)E^{\alpha\beta} + \nu a^{\alpha\beta} E^\gamma_\gamma], \tag{12}$$

$$M^{\alpha\beta} = D[(1-\nu)K^{\alpha\beta} + \nu a^{\alpha\beta} K^\gamma_\gamma], \tag{13}$$

where $a^{\alpha\beta}$ are the contravariant components of the metric tensor for the mid-surface. In (13), the bending stiffness D is given by

$$D = \frac{Et^3}{12(1-\nu^2)}. \tag{14}$$

Utilising (12), (11) can be written in a form more convenient in the following as

$$W = \frac{1}{2Et}[(1+\nu)N^\beta_\alpha N^\alpha_\beta - \nu N^\alpha_\alpha N^\beta_\beta] + \frac{Et^3}{24(1-\nu^2)}[(1-\nu)K^\beta_\alpha K^\alpha_\beta + \nu K^\alpha_\alpha K^\beta_\beta]. \tag{15}$$

The non-linear strain–displacement relations allowing for large deformations of the delaminating layer are given by the Donnell–Mushtari–Vlasov approximations. These are valid for moderately large rotations and small characteristic wavelengths of the deformation pattern compared to the smallest principal radius of curvature of the mid-surface and are given by

$$E_{\alpha\beta} = \tfrac{1}{2}(D_\alpha v_\beta + D_\beta v_\alpha) - d_{\alpha\beta} w + \tfrac{1}{2} D_\alpha w D_\beta w, \tag{16}$$

$$K_{\alpha\beta} = D_\alpha D_\beta w. \tag{17}$$

Finally, the stresses are written as a sum of the prestresses, σ_0, and the difference from these in the form

$$N^{\alpha\beta} = \Delta N^{\alpha\beta} - a^{\alpha\beta}\sigma_0 t. \tag{18}$$

The calculations below are carried out assuming that the only stresses are caused by residual stresses, but this is not a general restriction of the formulation. Introducing n_α as the components of the unit normal vector to

the crack front, the membrane force and the bending moment in (1) and (2) are

$$N = \Delta N^{\alpha\beta} n_\alpha n_\beta, \quad M = M^{\alpha\beta} n_\alpha n_\beta. \tag{19}$$

Far in front and far behind the propagating crack front, $T = 0$.

The equations listed in this section are in the following specialised to a delaminated layer in a spherical shell.

4. Spherical shell

Introducing coordinates $(u^1, u^2) = (\varphi, \theta)$, a spherical mid-surface of radius R is represented by

$$\begin{aligned} x^1 &= R\cos\theta\cos\varphi, \\ x^2 &= R\cos\theta\sin\varphi, \\ x^3 &= -R\sin\theta, \end{aligned} \tag{20}$$

where a complete sphere is represented by $-\pi/2 < \theta < \pi/2$ and $0 \leqslant \varphi < 2\pi$. For a delaminated layer of width $2b$, the crack propagates in the equatorial φ-direction, and in the transverse direction the notation

$$y = \varepsilon b = \theta R, \quad -1 \leqslant \varepsilon \leqslant 1 \tag{21}$$

is introduced. The unloaded crack sides are represented by $\varepsilon = 1$ and -1, respectively.

Far in front and far behind the propagating part of the crack front the displacements are φ-independent and there is no displacement in the direction of crack propagation, i.e.

$$v^1 = 0, \quad v^2 = v^2(y), \quad w = w(y). \tag{22}$$

The strain–displacement relations under these conditions are

$$\begin{aligned} E_{11} &= -\cos\theta\sin\theta \cdot v_2 + R\cos^2\theta \cdot w, \\ E_{12} &= 0, \\ E_{22} &= v_{2,2} + Rw + \tfrac{1}{2}(w_{,2})^2 \end{aligned} \tag{23}$$

and the bending strain measures are

$$\begin{aligned} K_{11} &= -\cos\theta\sin\theta \cdot w_{,2}, \\ K_{12} &= 0, \\ K_{22} &= w_{,22}. \end{aligned} \tag{24}$$

Furthermore, one of the in-plane equilibrium equation (9) results in $N^{11} = \text{constant}$, while the other reduces to

$$N^{22}_{,2} - \tan\theta \cdot N^{22} + \cos\theta\sin\theta \cdot N^{11} = 0 \tag{25}$$

and the out-of-plane equilibrium equation (10) becomes

$$\begin{aligned} &\frac{D}{R^4}(w_{,2222} - 2\tan\theta \cdot w_{,222} - (1 + \nu + \tan^2\theta)\, w_{,22} + \tan\theta\,(\nu - 2 - \tan^2\theta)\, w_{,2}) \\ &\quad - \frac{Et}{(1-\nu^2)R^4} \begin{pmatrix} (w_{,22} - R)(v_{2,2} - \nu\tan\theta \cdot v_2 - R(1+\nu)w + \tfrac{1}{2}(w_{,2})^2) \\ -(R + \tan\theta \cdot w_{,2})(-\tan\theta \cdot v_2 - R(1+\nu)w + \nu v_{2,2} + \tfrac{1}{2}\nu(w_{,2})^2) \\ -\dfrac{R^2(1-\nu^2)}{E}(w_{,22} - 2R - \tan\theta \cdot w_{,2})\sigma_0 \end{pmatrix} = 0. \end{aligned} \tag{26}$$

Non-dimensional equations are introduced according to (21) and

$$\tilde{v} = \frac{b}{t^2} v_2, \quad \tilde{w} = \frac{w}{t}, \quad \eta = \frac{b^2}{Rt}, \quad \theta_0^2 = \eta\frac{t}{R}, \quad \frac{\sigma_0}{\sigma_c} = \frac{\sigma_0 t b^2}{\pi^2 D}. \tag{27}$$

Eq. (25) then becomes

$$\tilde{v}'' = \theta_0^2(v + \tan^2(\varepsilon\theta_0))\tilde{v} - \eta(1+v)\tilde{w}' - \tilde{w}'\tilde{w}'' + \theta_0 \tan(\varepsilon\theta_0)(\tilde{v}' + \tfrac{1}{2}(1-v)(\tilde{w}')^2). \tag{28}$$

where the notation $()' = \mathrm{d}()/\mathrm{d}\varepsilon$ is introduced. Furthermore, (26) becomes

$$\begin{aligned}\tilde{w}^{(IV)} = {} & 2\theta_0 \tan(\varepsilon\theta_0)\tilde{w}''' - \theta_0^2(1 + v + \tan^2(\varepsilon\theta_0))\tilde{w}'' + \theta_0^3 \tan(\varepsilon\theta_0)(v - 2 - \tan^2(\varepsilon\theta_0))\tilde{w}' \\ & + 12(\tilde{w}'' - \eta)(\tilde{v}' - v\theta_0 \tan(\varepsilon\theta_0)\tilde{v} + \eta(1+v)\tilde{w} + \tfrac{1}{2}(\tilde{w}')^2) \\ & - 12(\theta_0 \tan(\varepsilon\theta_0)\tilde{w}' + \eta)(v\tilde{v}' - \theta_0 \tan(\varepsilon\theta_0)\tilde{v} + \eta(1+v)\tilde{w} + \tfrac{1}{2}v(\tilde{w}')^2) \\ & + (\theta_0 \tan(\varepsilon\theta_0)\tilde{w}' - \tilde{w}'' + 2\eta)\pi^2\left(\frac{\sigma_0}{\sigma_c}\right).\end{aligned} \tag{29}$$

For specified values of $\theta_0, \eta, \sigma_0/\sigma_c$, these two coupled, non-linear differential equations are most conveniently integrated numerically. The boundary conditions are taken to be clamped along $\varepsilon = 1$ and -1. Once a solution for displacements has been obtained, (23) and (24) give the strains and (12) and (13) give the stresses and moments. The energy release rate and phase angle of loading along the sides of the delaminated region is in turn given by (1) and (2) using (19) and the energy release rate along the propagating front is obtained by combining (15) with

$$G_{ss} = \frac{1}{b}\int_0^b (W_2 - W_1)\,\mathrm{d}y, \tag{30}$$

where W_2 and W_1 denote the strain energy density far behind and far in front of the propagating crack front. The integral in (30) is evaluated numerically as the stress σ_0/σ_c is increased utilising the relationship between b and σ_0/σ_c given in (27).

5. Results and discussion

Comparing the governing equations for buckling-driven delamination in spherical systems (28) and (29) to the governing equations for the cylindrical case Hutchinson (2001), one observes that two rather than one dimensionless combinations of the geometrical parameters b, R, t enter these. The combination of the three parameters for the cylindrical case is η defined in (27). By (27)–(29) any two combinations of η, θ_0 and t/R can be chosen as independent variables. The two dimensionless combinations η and t/R are chosen as independent variables and the energy release rate is plotted in Fig. 2 as a function of t/R for selected values of η. When plotting results for different levels of prestress, σ_0, it is convenient to introduce the half-width, b_0, required to make a delamination on a flat substrate initially buckle at the residual stress, $\sigma_0 = \sigma_c$. The relation between the width of delamination and the residual stresses are

$$\frac{b}{b_0} = \left(\frac{\sigma_0}{\sigma_c}\right)^{1/2}. \tag{31}$$

As can be seen by Fig. 2 for the range of parameters selected, the parameter η is the dominating dimensionless geometrical parameter, while t/R has a practically negligible influence on the energy release rate. Similar observations can be made for the influence of geometrical parameters on the phase angle of loading ψ. As a consequence of the observation, energy release rate and phase angle of loading are shown as a function of the parameter η only i.e. they are taken to be independent of t/R. The variation of the fracture mechanical parameters are thus only shown as function of one rather than two dimensionless combinations of t, R and b in the following. The energy release rate in Fig. 2 is normalised by a value, G_0, which can be interpreted as the energy release rate of a plane strain edge crack propagating under steady-state conditions i.e.

$$G_0 = \frac{(1-v^2)t\sigma_0^2}{2E}. \tag{32}$$

In Fig. 3 the variation of the energy release rate along the sides of the delamination are shown for four different values of η where the results for $\eta = 0$ corresponds to the planar case. An essential difference between

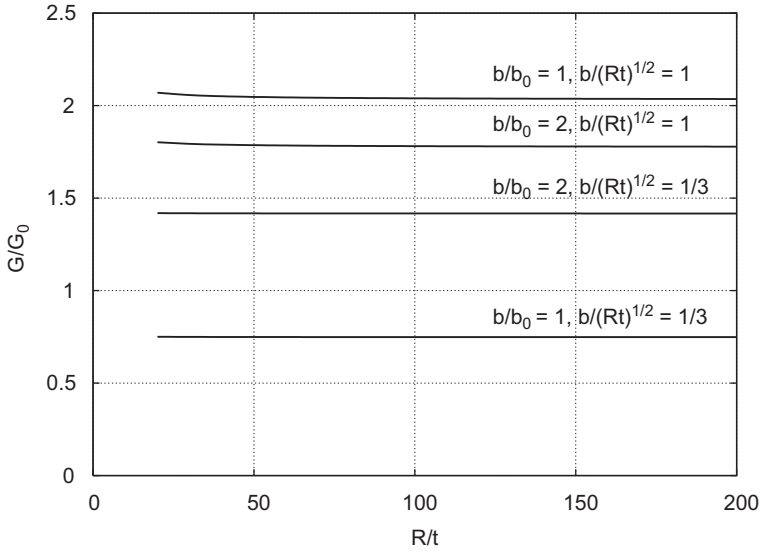

Fig. 2. Energy release rate along the sides of the delaminated region as a function of R/t for fixed values of $\eta = b^2/(Rt)$.

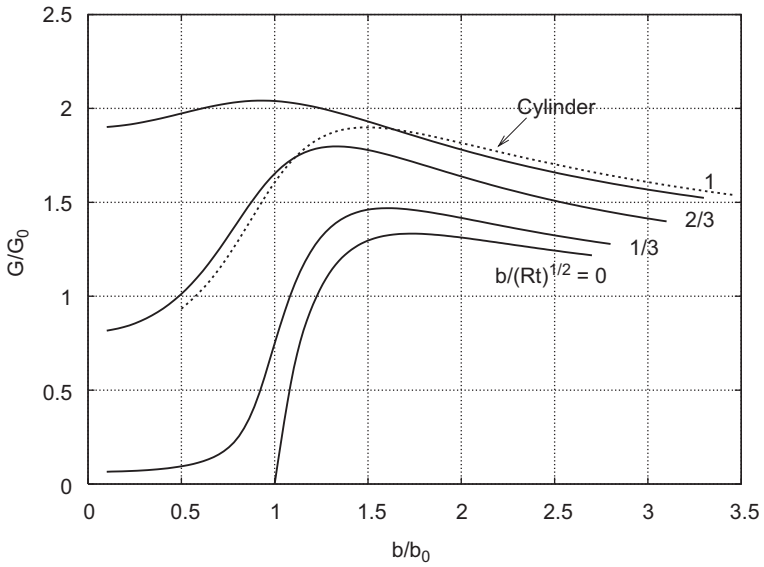

Fig. 3. Normalised energy release rate along the sides of the delaminated region as a function of residual stress level for different values of $\eta = b^2/(Rt)$. Results for a cylindrical substrate for $\eta = 1$ is included for comparison.

results obtained for curved substrates and planar substrates is that the energy release rate is zero in the planar case until the bifurcation point is reached at $b = b_0$. Curvature of the substrate acts in a way similar to a geometrical imperfection, by triggering out-of-plane deformations of the delaminated area for infinitesimal stresses. This results in effective bending moments and membrane forces along the crack front and thus finite values of the energy release rate through (1). Included in Fig. 3 for comparison are the results for the cylindrical case (Hutchinson, 2001) for $\eta = 1$. By comparison of the results for the cylinder and the sphere, one can see that the shape of the shell has a significant influence especially at low levels of residual stress. As a consequence, although the dimensionless combination of geometrical parameters η, which is the only

combination entering the equilibrium equations for the cylinder, also is shown to be the most significant combination for the sphere, the results for the cylindrical shell do not quantify the effect of substrate curvature on buckling-driven delamination. I.e. the shape of the substrate has profound influence on the energy release rate especially at relatively low stress levels. As the parameter η is increased, the peak value of the energy release rate increases and the peak shifts towards smaller stress levels.

In Fig. 4 the variation of the phase angle of loading, ψ, calculated numerically by (2) is shown. It is a characteristic feature for buckling-driven delamination that the phase angle of loading along the sides of the crack front becomes increasingly more mode II dominated. At a characteristic stress, the crack tip loading becomes purely mode II, i.e. $\psi = -90^\circ$. The curves in Fig. 3 are terminated at the transition to pure mode II loading since large-scale crack face contact occurs beyond that point, which is not taken into account in the present analysis. Qualitatively the trends in these curves are similar to the trends observed for a cylindrical substrate. Again as for the results in Fig. 3 for the energy release rate, the largest deviations between the spherical, the planar and the cylindrical cases occur at the smallest stress levels. However, at larger stress levels deviations become smaller. Effects of the phase angle of loading are most pronounced as the crack tip loading becomes mode II dominated (Jensen et al., 1990). As a consequence, less influence of substrate curvature on mixed mode interface fracture toughness effects is observed than the direct influence of curvature on the energy release rate in Fig. 3. For the results presented in Fig. 4, an assumption regarding the value of the angle ω appearing in (2) has to be made, which in turn depends on the elastic mismatch in the system through the Dundurs' parameters (3). All other results presented are independent of the elastic mismatch is stated in Section 2, ω has been tabulated in Suo and Hutchinson (1990). The variation of ω is rather modest, typically it varies in the range $45^\circ < \omega < 65^\circ$. Here, $\omega = 52.1^\circ$ is assumed corresponding, for instance, to the case of no elastic mismatch.

In Fig. 5, the steady-state energy release rate along the propagating part of the interface crack is shown as a function of residual stresses. The results are obtained by numerical integration of (29), which only requires knowledge of states far in front and far behind the propagating front. As a consequence, details such as the shape of the propagating part of the crack front cannot be resolved. These details were studied in Jensen and Sheinman (2001) by a complete finite element modelling of the delaminated region for a planar substrate. The effect of substrate curvature is considerably more pronounced than for the cylindrical case studied in Hutchinson (2001). At the value $\eta = 1$, the energy release rate at small stress levels is almost factor of 3 higher

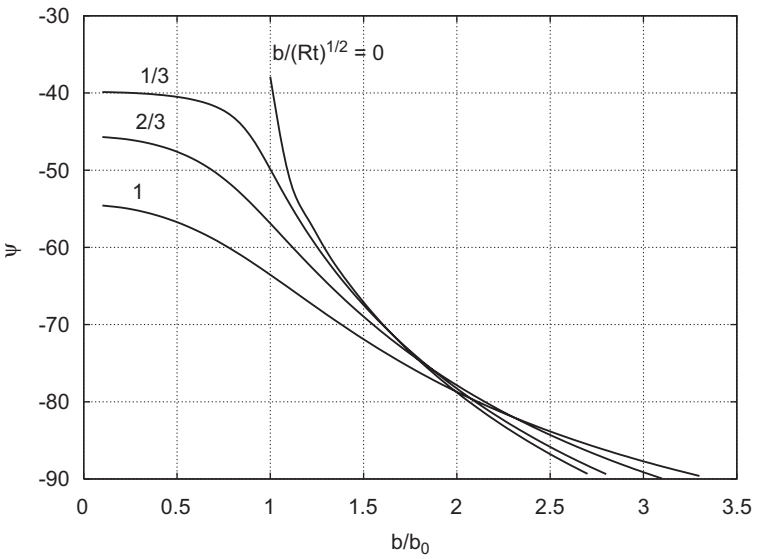

Fig. 4. Variation of phase angle of loading along the sides of the delaminated region as a function of residual stress level for different values of $\eta = b^2/(Rt)$.

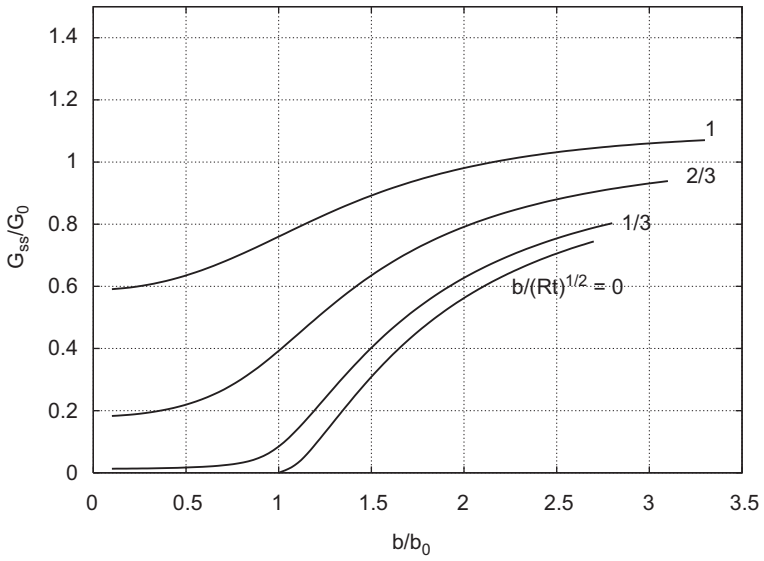

Fig. 5. Normalised steady-state energy release rate along the propagating front of the delamination as a function of residual stress level for different values of $\eta = b^2/(Rt)$.

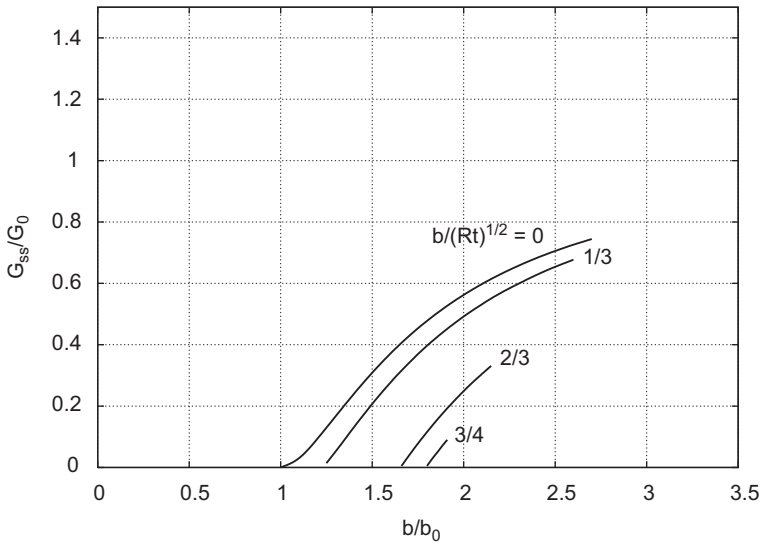

Fig. 6. Normalised steady-state energy release rate along the propagating front of the delamination for a thin surface layer on the inside of the spherical shell as a function of residual stress level for different values of $\eta = b^2/(Rt)$.

for the spherical than the cylindrical case, thus making a spherical shell much more prone to buckling-driven delamination.

In Fig. 6, the steady-state energy release rate along the propagating part of the interface crack is shown as a function of residual stresses in the case where the thin layer is located on the *inside* of the sphere. Numerical solutions to (28) and (29) can be found for negative values of the normal deflection w. This indicates an inward deflection of the layer as dictated by the presence of the substrate. The solutions are plotted in the range where they are meaningful, i.e. in the range where $G_{ss} > 0$ and $\psi < -90^\circ$. As expected, the probability of buckling-driven delamination of a thin layer occurring on the inside of the sphere is much less than for it occurring at the outside.

6. Conclusion

Effects of substrate curvature on buckling-driven delamination of thin films or layers were studied by considering initial delamination and steady-state propagation of a narrow layer bonded to a spherical substrate. The delaminated layer propagates in a self-similar fashion along the crack front leaving behind unloaded crack faces. The analysis was carried out by treating the boundary between the delaminated region and the substrate as an interface crack front, which is loaded under mixed mode conditions. Small-scale yielding conditions and small-scale contact of the crack faces at the crack front were assumed.

Results for the energy release rate and phase angle of loading along the sides of the delaminated region and the energy release rate for steady-state delamination were compared to results from the literature for delamination of thin films on planar and cylindrical substrates. The major effect of substrate curvature for the cylindrical substrate compared to the planar substrate is that it acts in a way much similar to the effect of geometrical imperfections in the sense that normal deflections and crack driving forces can be present for any small residual stress state in the film. In the planar case, the crack driving force is zero until a bifurcation point is passed. Delamination growth will take place in the post-buckling regime provided it occurs at all. For the case of a curved substrate there is a bifurcation point only in the case where the film is applied to the inside of the substrate so that contact between the film and the substrate prevents the film from deflecting to the side it would naturally deflect if it was applied to the outside of the substrate.

The effects of a double curved substrate, such as the spherical substrate, compared to the cylindrical substrate is that an additional non-dimensional combination of geometrical parameters enters the formulation. It has been shown that this additional combination of geometrical parameters play a minor role on the energy release rate and phase angle of loading for the range of parameters considered here. This result is believed to be key to the present study since this implies, for any doubly curved substrate, that the non-dimensional combination of geometrical parameters identified for the cylindrical substrate is the only parameter required in addition to material parameters when mapping the energy release rate and the phase angle of loading.

The fact that only one non-dimensional combination of geometrical parameters appears to be of significance—namely that identified for the cylindrical substrate—does not imply, however, that results for the cylindrical substrate are representative for any double curved substrate. The *shape* of the substrate also affects the energy release rate and the phase angle of loading. This is a second key result of the present investigation. For the spherical substrate the shape affects the energy release rate most significantly at small values of normalised residual stress levels where the tendency is that the higher the substrate curvature, the higher the peak value of the energy release rate along the sides of the delamination, and this peak moves towards smaller values of residual stress.

Acknowledgements

Support from the Danish Technical Research Council through the Framework Programme "Interface Design of Composite Materials" (STVF fund no. 26-03-0160) is gratefully acknowledged.

References

Audoly, B., 1999. Stability of straight delamination blisters. Phys. Rev. Lett. 83, 4124–4127.

Chai, H., Babcock, C.D., Knauss, W.G., 1981. One dimensional modelling of failure in laminated plates by delamination buckling. Int. J. Solids Struct. 17, 1069–1083.

Dundurs, J., 1969. Edge-bonded dissimilar orthogonal elastic wedges. J Appl. Mech. 36, 650–652.

Evans, A.G., Hutchinson, J.W., 1984. On the mechanics of delamination and spalling in compressed films. Int. J. Solids Struct. 20, 455–466.

Evans, A.G., Hutchinson, J.W., 1989. Effects of non-planarity on the mixed mode fracture resistance of bimaterial interfaces. Acta Materialia 37, 909–916.

Gioia, G., Ortiz, M., 1997. Delamination of compressed thin films. Adv. Appl. Mech. 33, 119–190.

Hutchinson, J.W., 2001. Delamination of compressed films on curved substrates. J. Mech. Phys. Solids 49, 1847–1864.

Hutchinson, J.W., Suo, Z., 1992. Mixed mode cracking in layered materials. Adv. Appl. Mech. 29, 63–191.

Hutchinson, J.W., Thouless, M.D., Liniger, E.G., 1992. Growth and configurational stability of circular, buckling-driven film delaminations. Acta Metall. Matererialia 40, 295–308.

Hutchinson, J.W., He, M.Y., Evans, A.G., 2000. The influence of imperfections on the nucleation and propagation of buckling driven delaminations. J. Mech. Phys. Solids 48, 709–734.

Jensen, H.M., 1993. Energy release rates and stability of straight-sided, thin-film delaminations. Acta Mater. 41, 601–607.

Jensen, H.M., Sheinman, I., 2001. Straight-sided, buckling-driven delamination of thin films at high stress levels. Int. J. Fract. 110, 371–385.

Jensen, H.M., Sheinman, I., 2002. Numerical analysis of buckling-driven delamination. Int. J. Solids Struct. 39, 3373–3386.

Jensen, H.M., Thouless, M.D., 1995. Buckling instability of straight edge cracks. J. Appl. Mech. 62, 620–625.

Jensen, H.M., Hutchinson, J.W., Kim, K.-S., 1990. Decohesion of a cut prestressed film on a substrate. Int. J. Solids Struct. 26, 1099–1114.

Moon, M.-W., Jensen, H.M., Hutchinson, J.W., Oh, K.H., Evans, A.G., 2002. The characterization of telephone cord buckling of compressed thin films on substrates. J. Mech. Phys. Solids 50, 2355–2377.

Moon, M.-W., Chung, J.-W., Lee, K.-R., Oh, K.H., Hutchinson, J.W., Evans, A.G., 2006. Telephone cord buckling of thin compressed films on curved substrates. Harvard University Report.

Niordson, F.I., 1985. Shell Theory, North-Holland Publishers, Amsterdam.

Ortiz, M., Gioia, G., 1994. The morphology and folding patterns of buckling-driven thin-film blisters. J. Mech. Phys. Solids 42, 531–559.

Storåkers, B., Nilsson, K.F., 1993. Imperfection sensitivity at delamination buckling and growth. Int. J. Solids Struct. 30, 1057–1074.

Suo, Z., Hutchinson, J.W., 1990. Interface crack between two elastic layers. Int J. Fract. 43, 1–18.

Tvergaard, V., Hutchinson, J.W., 1993. The influence of plasticity on mixed mode interface toughness. J. Mech. Phys. Solids 41, 1119–1135.

Delamination of Compressed Thin Layers at Corners

Kim D. Sørensen Henrik M. Jensen* Johan Clausen

Department of Civil Engineering
Aalborg University
Sohngaardsholmsvej 57, DK-9000 Aalborg, Denmark

*Aarhus Graduate School of Engineering
University of Aarhus
Dalgas Avenue 4, DK-8000 Århus C, Denmark

Abstract

An analysis of delamination for a thin elastic layer under compression, attached to a substrate at a corner is carried out. The analysis is performed by combining results from interface fracture mechanics and the theory of thin shells. In contrast with earlier results for delamination on a flat substrate, the present problem is not a bifurcation problem. Crack closure at sufficiently high stress levels are shown to occur. Results show a very strong dependency on fracture mechanical parameters of the angle of the corner including the range of parameters where crack closure occurs. Analytical results for the fracture mechanical properties have been obtained, and these are applied in a study of the effect of contacting crack faces. Special attention has been given to analyse conditions under which steady state propagation of buckling driven delamination takes place.
Keywords: Delamination, Thin layers, Fracture mechanics, Crack closure, Steady state crack propagation.

1 Introduction

The influence of system curvature on buckling-driven delamination has been studied in Hutchinson (2001), Faulhaber *et al.* (2006) and Sørensen and Jensen (2008). The motivations for these studies have typically been applications like high temperature turbine blades with thermal barrier coatings Mumm and Evans (2000) or hip joint implants with biocompatible surface coatings Moon *et al.* (2002*b*) just to mention a few.

In a number of technically important applications, local curvatures are so high that they are better modelled as sharp corners. One example is shown

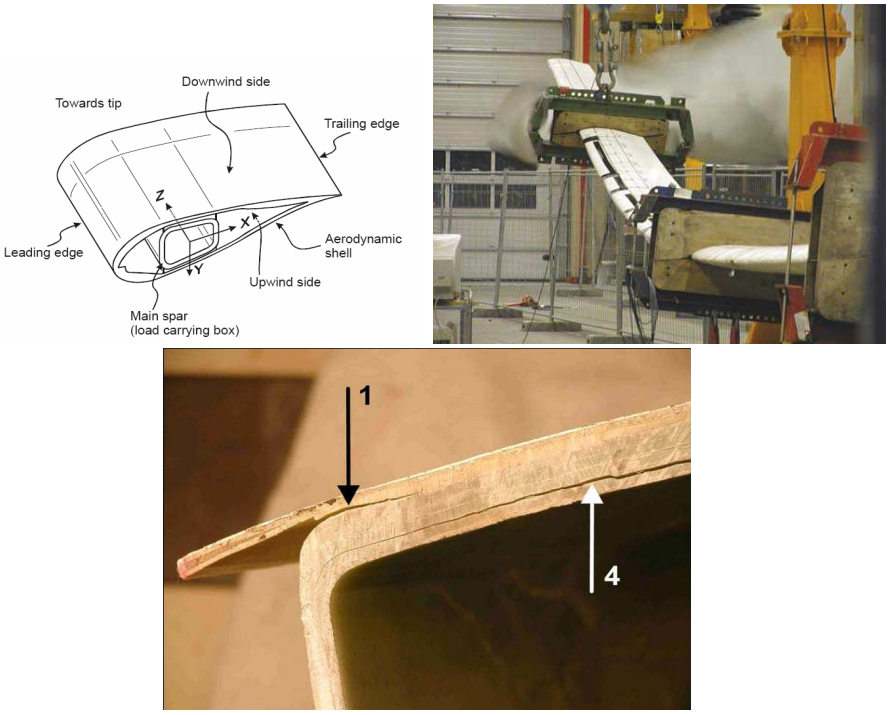

Figure 1: (a) Cross section of wind turbine blade, (b) test to failure and (c) cross section of load carrying main spar after failure showing delaminations close to the corners.

in Fig. 1, which is taken from Sørensen *et al.* (2004). Fig. 1(a) is a schematic view of a cross section of a wind turbine blade, Fig. 1(b) shows a picture of a blade at extreme load testing close to final failure, and Fig. 1(c) shows post failure cross sections of the load carrying main spar. Buckling driven delaminations in the layered glass fibre main spar are seen at the corners both on the inside and outside. Another example of delamination close to a sharp corner, but on a much smaller scale is at the edges of interconnecting plates in solid oxide fuel cells with layers of chromium oxide forming under compression in service Persson (2007). The present work focuses on studying buckling driven delamination at corners including the effects on the energy release rate and mode mixity, and the conditions for steady state propagation of such cracks. Buckling-driven delamination of thin layers on flat substrates has been studied in a number of previous works. The mechanism was described initially in Chai *et al.* (1981) with applications to composite plates in mind. In Hutchinson and Suo (1992) the steady-state propagation of buckling driven delamination was described. The phenomenon is a coupled problem of buckling of a thin, compressed layer on a substrate, and interface delamination between the layers. The buckling driven delamination is a commonly observed failure mode in layered materials and the

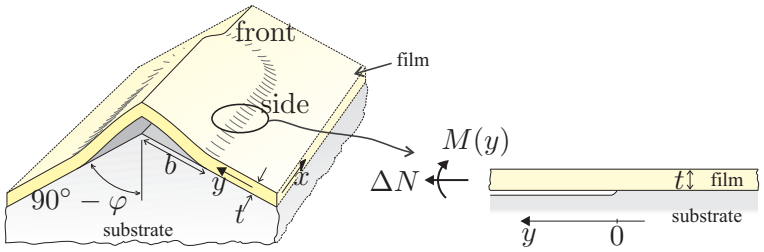

Figure 2: Sketch of problem analysed. A thin layer covering a substrate with a sharp corner fails by buckling driven delamination. The sides and the front of the delaminated region are indicated.

steady-state mode of propagation is normally the most critical resulting in the highest energy release rate. This mode of delamination is particularly critical since it, once initiated, propagates unhindered throughout the interface. In the following, the concept of buckling-driven delamination is explained in greater detail. Consider a thin layer attached to a substrate where the thin layer is subject to a uniform, biaxial compressive stress σ_0, see Fig. 2(a). The system contains a sharp corner defined by the angle φ. The case of $\varphi = 0°$ corresponds to a flat substrate. Suppose a small region exists, in which the bonding between the layer and the substrate is poor or nonexistent. If the compressive stress σ_0 exceeds a critical value σ_c, the layer will buckle away from the substrate and this buckling will have the effect, that the crack at the interface will be loaded by normal stresses and moments, as shown in Fig. 2(b). In case the energy release rate exceeds the mode adjusted fracture toughness of the interface, the bonding between the delaminated layer and the other layers (the substrate) will break and the size of the delaminated region may grow. For $\varphi \neq 0$ the delamination may initially be triggered by the stress singularity at the corner and crack tip loadings are present at all levels of compressive stresses.

Different types of buckling delaminations have been observed, among these the circular buckle, the 'telephone cord' buckle and the straight-sided buckle. In the present paper attention will be given to steady state propagation of the latter, which is characterized by the fact that it grows at one of the ends while the sides remain stationary, see Fig. 2(a).

Many problems concerning propagation of cracks or other types of instabilities can be treated using the concept of steady-state growth, see Kyriakides (1994), which entails a significant simplification of the problem. Steady-state crack growth implies that the front of the crack assumes a certain shape that will remain unchanged during propagation, which means that the energy release rate will not depend on the length of the crack or the geometry of the crack front. In the following, steady-state conditions will be assumed. Designing for safety against steady-state crack growth ensures

that wide spread cracking will not occur, assuming some limited damage may be accepted. If this is not the case, designing for safety against crack initiation will lead to a certain probability of failure.

For the propagation of a straight-sided delamination buckle on a plane substrate it is found, that even though the crack grows at its end, the energy release rate at the front is considerable lower than at the side. This is due to the fact that the fracture toughness of the interface depends strongly on the so-called mode mixity which again depends on the loads on the interface crack. Interface toughness laws, which describe this dependency, are formulated in Jensen *et al.* (1990). This effect is even more pronounced for the present geometry as it turns out that the presence of the corner induces a relatively larger mode 2 contribution to the energy release rate compared to the planar case. For that reason an analysis has been included, which explicitly treats the effects of contacting crack faces, and the influence of contact on buckling driven delamination has been addressed.

2 Corner stresses for perfect bonding

To further motivate the present analysis and emphasise some of the limitations, we at first present results for the case of perfect bonding between a thin layer and a substrate at a corner. Material data are chosen to be representative of oxide layers on chromium-steel substrates at elevated temperatures. The geometry is sketched in Fig. 3 with dimensions typical of the interconnect plates in solid oxide fuel cells studied in Persson (2007). An oxide layer of thickness $10\mu m$ has typically developed after 1000 hours service at 900°. For the steel substrate the Young's modulus at 900° is $E = 87GPa$, the Poisson's ratio is $\nu = 0.3$, the yield stress is $\sigma_y = 40MPa$ and the material does not work harden. For the oxide layer, $E_0 = 298GPa$, $\nu_0 = 0.29$, and the material is linear elastic. Compressive stresses build up in the oxide layer as it grows due to lattice mismatch. The strain, ε_0, is a measure of initial stresses; it is the strain in the layer relative to the unstressed state just when it is attached to the substrate, i.e. the stress in the layer if the substrate was infinitely rigid would be $\sigma_0 = E_0\varepsilon_0/(1-\nu_0)$. Finite element calculations based on the commercial code ABAQUS are carried out leading to the results in Fig. 4 for the shear stress, σ_{12}, measured in MPa. The sharp corner induces a stress singularity, which could lead to crack initiation at the interface close to the corner. The stress concentrations are seen to spread over distances several times the layer thickness. In Persson (2007) cases are seen where interface cracking between the oxide layer and the metal substrate occurs close to the corners. At the highest level of initial stresses, asymmetries in the stress profile develop due to the finite thickness of the plate. The analysis in the following sections assumes a symmetric stress profile at the corner. Plastic deformation under small scale yielding condi-

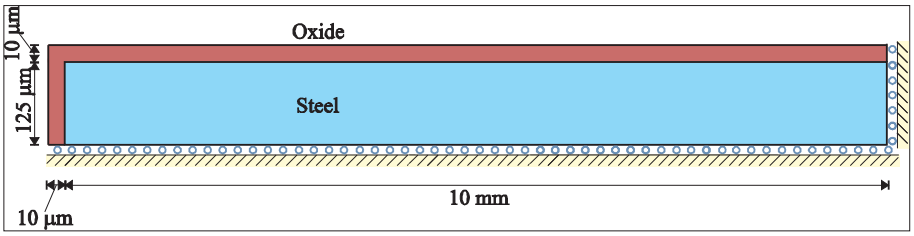

Figure 3: Sketch of geometry of connector plate in fuel cell with a thin oxide layer under compression.

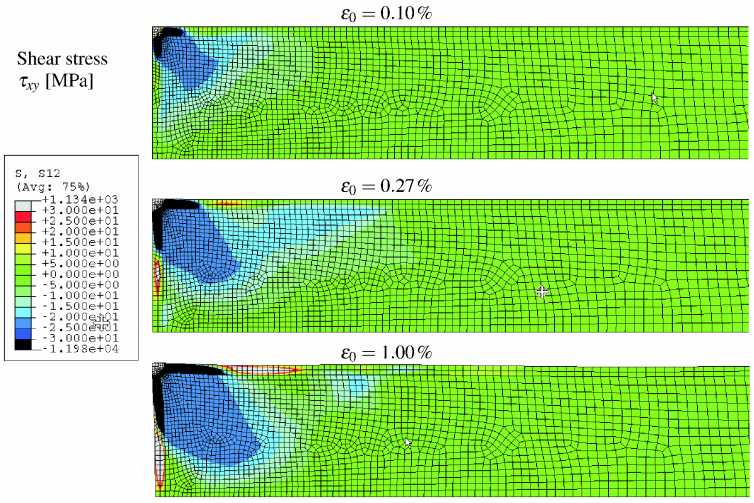

Figure 4: Shear stress, σ_{12}, in bonded bimaterial system for different values of initial stress.

tions is allowed for, and effects of plasticity in the substrate is specifically modelled by introducing a mixed mode interface fracture criterion, which reflects that the extent of the plastic zone and thus the amount of energy dissipated during crack growth depends strongly on the ratio between the crack tip loadings.

In Fig. 5 the equivalent plastic strain is shown for the same material parameters and initial stresses as in Fig. 4. The results demonstrate a long range effect of plasticity at the corner. This is due to general yielding of the substrate as the initial stress is increased, which reduces the effective stiffness of the substrate so that buckling of the compressed thin layer may take place, Biot (1965). The effect of layer buckling will be an undulation of the interface, which was studied in Hutchinson *et al.* (2000). It was shown that the effect has significant influence on the energy release rate for an interface crack. The effects of layer buckling prior to delamination are not studied in the present work. We emphasise that while the results presented

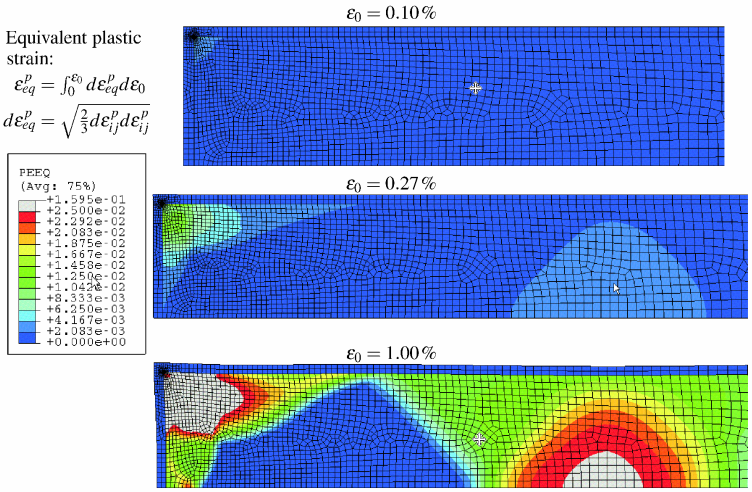

Figure 5: Effective plastic strain, ε_{eq}, for different values of initial stress. At highest stress levels indications of initial buckling of the compressed bonded layer are seen.

in Figs. 4 and 5 use specific material parameters and geometrical quantities for interconnect plates, the fracture mechanical analysis below is carried out in more general terms allowing for arbitrary elastic mismatch and other corner geometries.

3 Fracture Mechanics

It is assumed that the size of the delamination is large relative to the thickness of the layer. It is furthermore assumed that the transition between the delaminated region of the layer and the bonded region has a length comparable to, or smaller than, the layer thickness. As a consequence of these assumptions, the boundary between the layer and the bonded region can be treated as an interface crack and the stresses in the delaminated region can be obtained from shell theory.

Following Suo and Hutchinson (1990) by application of the J-integral, the energy release rate, G, for the problem in Fig. 2(b) can be obtained as a function of the change in membrane stress, ΔN, relative to the initial stress in the bonded layer and the bending moment, M, in the layer as

$$\frac{G}{G_0} = \left(\frac{\Delta N}{\sigma_0 t}\right)^2 + 12\left(\frac{M}{\sigma_0 t^2}\right)^2 \tag{1}$$

where σ_0 is the initial stress in the layer and t is the layer thickness. The quantity G_0 corresponds to all the elastic energy stored in the layer being

released under plane strain conditions, and is given by

$$G_0 \equiv \frac{\left(1-\nu^2\right) t}{2E}\,\sigma_0^2 \tag{2}$$

Here, E is the elastic modulus of the layer, and ν is the Poisson's ratio. By the definition, in the limit where the layer becomes completely detached from the substrate assuming plane strain in the layer, the energy release rate asymptotically approaches G_0. It should be emphasised that all the elastic energy stored in the layer is $2G_0/\left(1+\nu\right)$ i.e. at least 33% higher. This is important when discussing possible fracture modes, which release more energy than G_0 at high stress levels, see Jensen and Sheinman (2002) and Moon *et al.* (2002*a*).

Along the propagating crack front in Fig. 2(a), there will also be a shear stress component giving a mode 3 contribution to the energy release rate in addition to the mode 1 and 2 contributions due to ΔN and M. As explained below, however, when the crack front propagates under steady state conditions, the energy release rate along the front can be calculated by states far in front and far behind the propagating front where the shear stresses are zero. The mode mixity ψ giving the ratio between mode 1 and 2 stress intensity factors is related to the bending moment and the change in resultant stress by (Suo and Hutchinson (1990))

$$\tan\psi \equiv \frac{\sigma_{12}}{\sigma_{22}}\Big|_{r=t} = \frac{\Delta N t \sin\omega + \sqrt{12} M \cos\omega}{\Delta N t \cos\omega - \sqrt{12} M \sin\omega} \tag{3}$$

where ω is a function of the elastic mismatch between layer and substrate. It has been tabulated by numerical methods in Suo and Hutchinson (1990). Typical values of ω lie in the range $45^\circ < \omega < 75^\circ$ depending on the elastic mismatch, where the highest values correspond to stiff layers on compliant substrates, and $\omega = 52.1^\circ$ in the case of no elastic mismatch. In (3), σ_{12} and σ_{22} are shear and normal stresses in the plane of the crack a small distance r ahead of the tip. Since this ratio varies due to the oscillating crack tip singularity, the distance is specified to be equal to the layer thickness.

4 Stresses in delaminated layer

The effective membrane stress and bending moment required to calculate the fracture mechanical quantities listed in the previous section, are calculated from the theory of thin shells assuming the delaminated region to be clamped to the substrate along the crack front. For the present problem sketched in Fig. 2(b), the two halves on each side of the centre line of symmetry are planar problems, so plate theory is sufficient for calculating the stresses when imposing symmetry conditions at the centre line. Von Karman non-linear plate theory, see Niordson (1985), is applied allowing for large normal

deflections relative to the plate thickness. This geometrical non-linearity is essential since, for a flat substrate characterised by $\varphi = 0°$, the energy release rate is non-zero only a stress levels higher than the buckling stress.

The two in-plane and the out-of-plane equilibrium equations are given by

$$\begin{aligned} N_{\alpha\beta,\beta} &= 0 \\ M_{\alpha\beta,\alpha\beta} - N_{\alpha\beta} w_{,\alpha\beta} &= 0 \end{aligned} \tag{4}$$

where repeated index are summed over the values 1 and 2, and a comma denotes partial differentiation. The directions 1 and 2 are defined in Fig. 2(b) with $x_1 = x$ and $x_2 = y$. In (4), $N_{\alpha\beta}$ and $M_{\alpha\beta}$ are the tensors of membrane stresses and moments, respectively, and w is the out of plane deformation of the plate mid surface.

The strain-displacement relations in case of non-linear von Karman plate theory are

$$\begin{aligned} \varepsilon &= \frac{1}{2}\left(u_{\alpha,\beta} + u_{\beta,\alpha} + w_{,\alpha} w_{,\beta}\right) \\ \kappa_{\alpha\beta} &= w_{,\alpha\beta} \end{aligned} \tag{5}$$

where u_α are the in plane displacements, $\varepsilon_{\alpha\beta}$ is the strain tensor and $\kappa_{\alpha\beta}$ is the curvature tensor. The stress-strain relations assuming linear isotropic elasticity are

$$\begin{aligned} N_{\alpha\beta} &= \frac{Et}{1-\nu^2}\left(\left(1-\nu\right)\varepsilon_{\alpha\beta} + \nu\varepsilon_{\gamma\gamma}\delta_{\alpha\beta}\right) - \sigma_0 t \delta_{\alpha\beta} \\ M_{\alpha\beta} &= D\left(\left(1-\nu\right)\kappa_{\alpha\beta} + \nu\kappa_{\gamma\gamma}\delta_{\alpha\beta}\right) \end{aligned} \tag{6}$$

where $\delta_{\alpha\beta}$ is the Kronecker delta, and the bending stiffness D of the plate is

$$D = \frac{Et^3}{12\left(1-\nu^2\right)} \tag{7}$$

The energy release rate at the crack front G_{ss} is found by calculating the difference in energy density, W, in the non-deflected layer far in front of the crack front, W_2, and in the deflected layer far behind the crack front, W_1

$$G_{ss} = \frac{1}{b}\int_0^b \left(W_2 - W_1\right) \mathrm{d}y \tag{8}$$

The energy density, W, is a function of the stresses in the layer, and is obtained by Niordson (1985)

$$\begin{aligned} W &= \frac{1}{2Et}\left[\left(1+\nu\right)N_\alpha^\beta N_\beta^\alpha - \nu N_\alpha^\alpha N_\beta^\beta\right] \\ &\quad + \frac{Et^3}{24\left(1-\nu^2\right)}\left[\left(1-\nu\right)\kappa_\alpha^\beta \kappa_\beta^\alpha + \nu\kappa_\alpha^\alpha K_\beta^\beta\right] \end{aligned} \tag{9}$$

5 Results and discussion

For the present geometry, considerable simplifications follow the observation that far in front and far behind the propagating crack front, displacements and stresses are independent of $x = x_1$. So $()_{,1} = \partial() / \partial x_1 = 0$ and after introducing $()_{,2} = \partial() / \partial x_2 = \partial() / \partial y = y'$, two of the equilibrium equations in (4) are non-trivial and become

$$\begin{aligned} N_{22} &= const. \\ M''_{22} - N_{22} w'' &= 0 \end{aligned} \tag{10}$$

Combining (10) with (5) and (6) yields

$$\begin{aligned} N_{22} = \frac{Et}{1-\nu^2} \left(u'_2 + \frac{1}{2} \left(w' \right)^2 \right) - \sigma_0 t \\ w'''' - \frac{N_{22}}{D} w'' = 0 \end{aligned} \tag{11}$$

The boundary conditions corresponding to these non-linear, ordinary differential equations are specified at $y = 0$, which is at the crack front where the layer is clamped to the substrate and at $y = b$ which is at the centre line of symmetry.

$$\begin{aligned} w(0) = w'(0) = w'(b) = 0 \quad , \quad w'''(b) = \frac{N_{22}}{D} \tan\varphi \\ u_2(0) = 0 \quad , \quad u_2(b) = w(b) \tan\varphi \end{aligned} \tag{12}$$

The symmetry conditions at $y = b$ state that there is no rotation, that the projection of normal and shear forces parallel to the plane of symmetry is zero, and that the projection of normal and in plane displacements perpendicular to the plane of symmetry is zero. By (12), it is seen that for $\varphi = 0°$, the problem is homogeneous and a non-trivial solution exists beyond a bifurcation stress, only. The solution to the second equation in (11) with corresponding boundary conditions is

$$\frac{w(y)}{t} = \eta \left(\frac{1 - \cos\left(\pi\sqrt{n}\right)}{\pi\sqrt{n}\sin\left(\pi\sqrt{n}\right)} \left(1 - \cos\left(\frac{\pi\sqrt{n} y}{b} \right) \right) + \frac{1}{\pi\sqrt{n}} \sin\left(\frac{\pi\sqrt{n} y}{b} \right) - \frac{y}{b} \right) \tag{13}$$

where the following non-dimensional combinations have been introduced

$$\begin{aligned} \eta &= \frac{b}{t} \tan\varphi \\ \frac{n}{s} &= -\frac{N_{22}}{\sigma_0 t} \\ s &= \frac{\sigma_0}{\sigma_c} = \left(\frac{b}{b_0} \right)^2 \end{aligned} \tag{14}$$

Here, b_0 denotes the half-width of the flat layer when buckling initially occurs for a fixed residual stress, σ_0. The buckling stress for a clamped flat plate of width $2b$ is given by

$$\sigma_c = \frac{\pi^2 E t^2}{12\left(1-\nu^2\right) b^2} \tag{15}$$

The bending moment and membrane stress at the crack front giving the fracture mechanical properties are obtained by the constitutive relations

$$M = M_{22}\left(0\right) = Dw''\left(0\right) \quad , \quad \Delta N = \sigma_0 t + N_{22} \tag{16}$$

where the residual stress is defined positive in compression. In order to calculate n in (14), the first equation in (11) is integrated from 0 to b giving

$$N_{22} b = \frac{Et}{1-\nu^2}\int_0^b \left(\frac{1}{2}\left(w'\right)^2\right) \mathrm{d}y + \frac{Et}{1-\nu^2} w\left(b\right)\tan\varphi - \sigma_0 t b \tag{17}$$

where the boundary conditions (12) have been utilised. Next, an implicit equation for determining n is formulated by inserting the solution (13) into (17). After performing the integration and using (14) the following condition determines n

$$\frac{n}{s} = 1 - \frac{6}{\pi^2 s}\eta^2 \frac{\sin\left(\pi\sqrt{n}\right) - \pi\sqrt{n}\cos\left(\pi\sqrt{n}\right)}{\pi\sqrt{n}\left(1+\cos\left(\pi\sqrt{n}\right)\right)} \tag{18}$$

Solutions to (18) are obtained numerically for given η and s. Then (16) combined with (14) results in

$$\frac{M}{\sigma_0 t^2} = \frac{\eta}{\pi^2 s}\frac{\pi\sqrt{n}\left(1-\cos\left(\pi\sqrt{n}\right)\right)}{\sin\left(\pi\sqrt{n}\right)} \tag{19}$$

and

$$\frac{\Delta N}{\sigma_0 t} = 1 - \frac{n}{s} \tag{20}$$

The energy release rate G_l along the sides of the delamination far behind the propagating front is obtained by inserting (19) and (20) in (1) and the corresponding mode mixity, ψ_l, is obtained by (3). The energy release rate along the crack front G_{ss} is obtained by specialising the general expression for W in (9) to the present geometry where

$$W = \frac{1}{Et}\left(N_{11}^2 + N_{22}^2 - 2\nu N_{11}N_{22}\right) + \frac{D}{2}\left(w''\right)^2 \tag{21}$$

Since the membrane stresses are constant

$$\begin{aligned} G_{ss} &= \frac{1}{b}\int_0^b \left(W_2 - W_1\right) \mathrm{d}y \\ &= \frac{1-\nu^2}{2Et}\left(\sigma_0^2 t^2 + N_{22}^2\right) - \frac{D}{2b}\int_0^b \left(w''\right)^2 \mathrm{d}y \end{aligned} \tag{22}$$

Inserting the solution (13) in (22) results in

$$\frac{G_{ss}}{G_0} = 1 - \left(\frac{n}{s}\right)^2 - \frac{12\eta^2}{\pi^4 s^2}\frac{\pi\sqrt{n}}{1+\cos\left(\pi\sqrt{n}\right)}\left(\pi\sqrt{n} - \sin\left(\pi\sqrt{n}\right)\right) \qquad (23)$$

In Hutchinson and Suo (1992) the mode mixity, ψ_{ss}, along the propagating front was estimated using the results for a full circular crack. The accuracy of this approach was in Jensen and Sheinman (2001) shown to be good.

It should be noted that the method for determining G_{ss} is exact provided the energy released along the crack front is independent of the mixed mode 1, 2 and 3 loading history. Results discussing this assumption have not, to our knowledge, been published. However, the results in Jensen and Sheinman (2001) indicated that the mode 3 contribution to the energy release rate remained smaller than 1/5 times the mode 1 and 2 contributions, and that the mode 3 component was only significant on a small portion of the propagating crack front close to the transition between the propagating part and the sides left behind. A recent paper by Tvergaard and Hutchinson (2008) investigates the effect of mode 3 on interface toughness. They consider cases, which are mainly mode 1 dominated, while the present problem is mainly mode 2 dominated. Their results show cases where the toughness is sensitive to mode 3 components. However, in the present case where only a small portion of the crack front has a significant mode 3 component, path dependent effects not taken into account in the present approach are believed to play a secondary role. A verification of the assumption is beyond the scope of this investigation.

The results for G_l, ψ_l and G_{ss} are shown in figures 6, 7 and 8, respectively, for different values of b/b_0. When the angle φ is zero, the problem corresponds to delamination on a flat substrate, where the stress in the layer has to exceed the critical value, σ_c, before any deflection of the layer can occur. When assumes a non-zero value, the problem is no longer a bifurcation problem and solutions exist for stresses below the critical stress for buckling of a plate, σ_c.

It is important to emphasise that the two sets of curves for G_l and G_{ss} in Figs. 6 and 8 correspond to different mode mixities. In Fig. 7 the mode mixity along the propagating front using results for a full circular delamination from Hutchinson and Suo (1992) is also included. It is noted that the mode mixity along the front is considerably lower than along the crack sides, that the crack tip along the propagating front never closes, and that crack closure occurs corresponding to $\psi_l = -90^\circ$ along the sides. By Fig. 7, it is clear that the angle φ has a pronounced influence on the mode mixity especially on the conditions for crack closure. The results in Figs. 6-8 are valid for other combinations of the angle φ and the crack length b/t provided the value of η in (14) is the same.

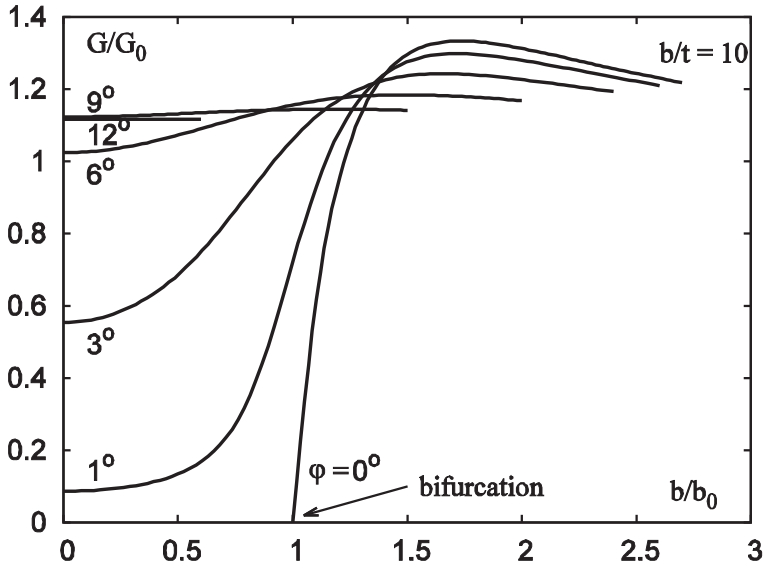

Figure 6: Energy release rate along the sides of the delaminated region.

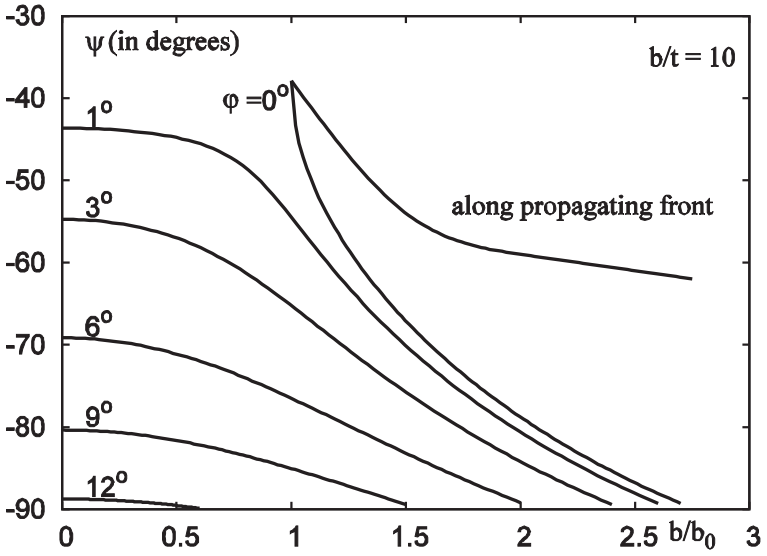

Figure 7: Mode mixity along the sides of the delaminated region and the front using the results for a full circular delamination.

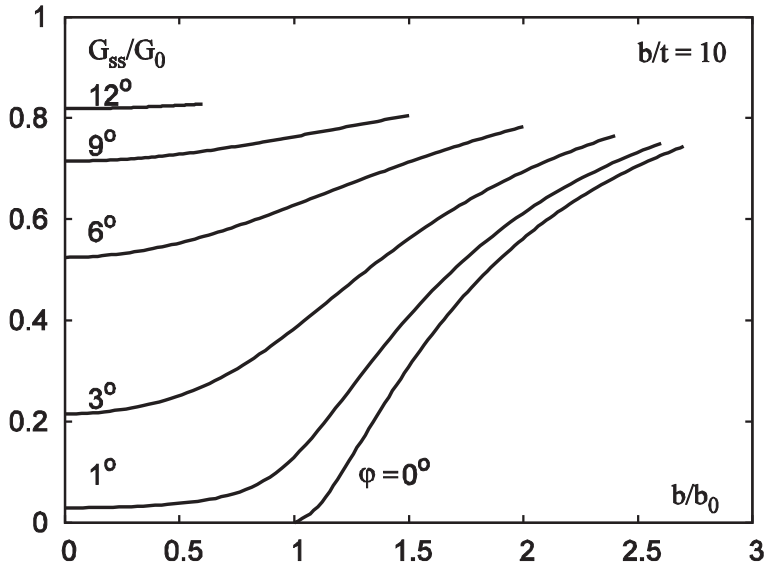

Figure 8: Energy release rate along the front of the delaminated region.

A mixed mode fracture criterion prior to crack closure has been invoked by introducing the criterion in Jensen *et al.* (1990)

$$G = G_c \left(1 - (\lambda_2 - 1)\sin^2\psi\right)^{-1} \tag{24}$$

where the factor λ_2 adjusts the relative contribution of mode 2 to the fracture criterion. Experimental support for the fracture criterion may be found in Cao and Evans (1989), Jensen *et al.* (1990) and Liechti and Chai (1991). A discussion of the relation between the fracture criterion (24) and detailed micro-mechanical models of contact and friction along the crack faces may be found in Evans and Hutchinson (1989) and Jensen (1990). Specifically, the parameter λ_2 could be associated with microscopic parameters for the interface such as the height and angle of surface asperities, coefficient of friction etc. In Tvergaard and Hutchinson (1993) it was shown that also plastic deformation in the layers can explain the mode dependent interface fracture toughness. The effect of imposing a mixed mode interface fracture criterion prior to crack closure will be demonstrated after introduction of an exact asymptotic expression for the fracture mechanical parameters. In the limit $\sigma_0/\sigma_c \to 0$ the expressions for the energy release rates along the sides, G_l, and along the propagating front, G_{ss}, and the mode mixity at the sides, ψ_l, can be obtained in closed form as

$$\frac{G}{G_0} = \frac{\eta^2\left(3+\eta^2\right)}{\left(1+\eta^2\right)^2},\ \frac{G_{ss}}{G_0} = \frac{\eta^2}{1+\eta^2},\ \tan\psi_l = \frac{\eta\tan\omega + \sqrt{3}}{\eta - \sqrt{3}\tan\omega} \tag{25}$$

which will also be used later to illustrate effects of contacting crack faces. The ratio b/t has to exceed some specified value, say 5, for the shell solutions

to be reasonably accurate, which for specific values of φ restricts how small η can be.

By (25) it is seen that the mode mixity exceeds $-90°$ indicating that the crack faces are in contact over distances comparable to the layer thickness if the crack length exceeds a critical value

$$\frac{b}{t} \geq \frac{\sqrt{3}\tan\omega}{\tan\varphi} \tag{26}$$

Whether this critical value is in the range where the shell solution is valid depends both on the elastic mismatch and the angle φ.

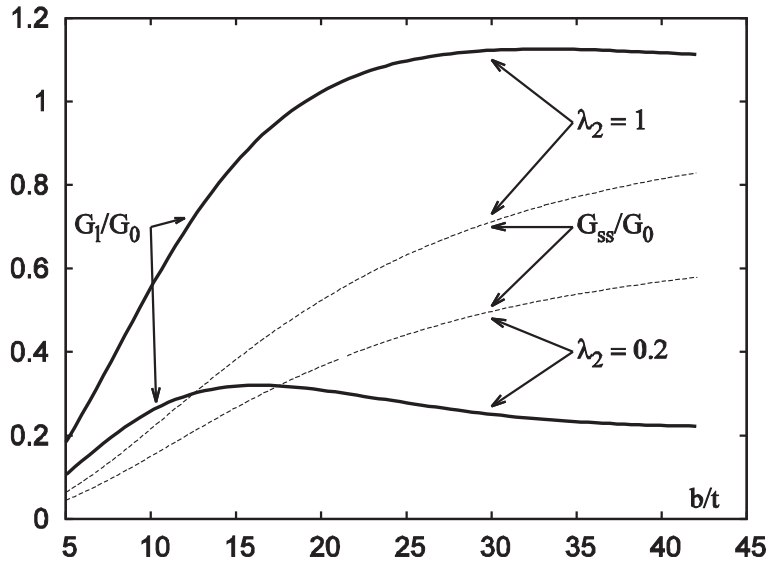

Figure 9: Mode adjusted energy release rate along the sides and the front imposing a mixed mode fracture criterion prior to crack closure. The preferred failure mode is the one with highest energy release rate.

Two sets of curves for G_l and G_{ss} based on (25) and imposing (24) are shown in Fig. 9; one set is for $\lambda_2 = 1$ corresponding to a usual mode independent Griffith fracture criterion, the other set of curves is for $\lambda_2 = 0.2$, which in Jensen *et al.* (1990) gave best agreement with experimental results. The curve has been plotted for $\varphi = 3°$ but as before is valid for other combinations of φ and b/t provided the value of η is the same. The curves are terminated at the point where crack closure occurs. The top solid curve and the top dashed curve are G_l and $G_s s$ for $\lambda_2 = 1$ where it is seen that most energy is always released along the sides in contrast to observations. Like in Hutchinson and Suo (1992) the fact that propagating buckling driven delamination is commonly observed can be explained by imposing a mixed mode fracture criterion. The bottom solid and dashed curves correspond to $\lambda_2 = 0.2$ where it is seen the mode adjusted energy

release rate is highest along the sides at small delamination lengths and along the front at larger delamination indicating a transition of failure modes. By the results in Fig. 7 for the energy release rate it is seen that as the angle φ is increased, the range in which the crack is open and where (24) can be applied narrows considerably. It is for this reason investigated in the following section whether frictional sliding after crack closure occurs alone can explain a change in the failure mode.

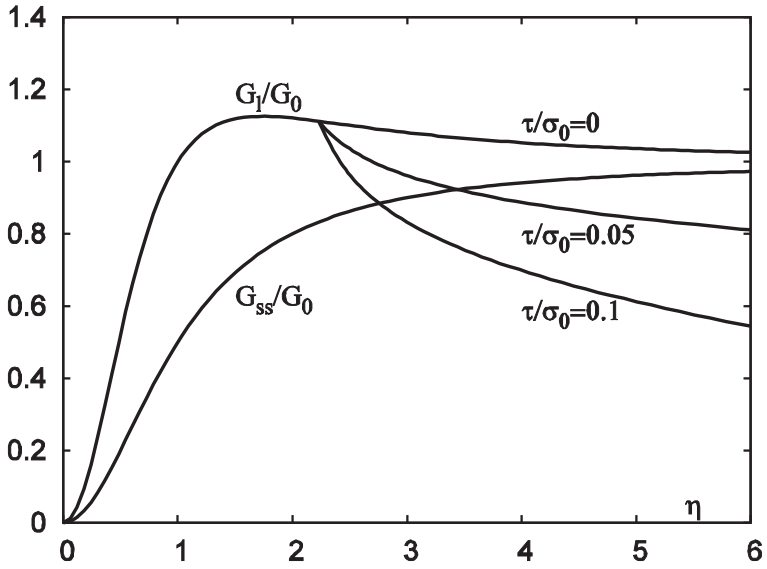

Figure 10: Energy release rate along the sides and the front taking contact and friction into account after crack closure takes place.

For negative values of φ, solutions for the membrane force and the bending moment in cases not resulting in overlap between the layer and the substrate could be found for large initial imperfections of the shape of the delaminated region, only, and the issue will not be pursued further here. The effect of negative curvature i.e. delamination of a layer on the inside of a shell was investigated in Hutchinson (2001) for a cylindrical shell and in Sørensen and Jensen (2008) for a spherical shell. In both cases the energy release rate is lower than for delaminations on the outside of the shell, and the delaminations exist and propagate only for a limited range of parameters. Qualitatively, this is appears to be in agreement with the observations in Fig. 1(c) that the delamination at the inside of the main spar tends to arrest as it approaches the inside corner (the crack opening displacements decrease). And the delamination on the outside of the main spar has increasing crack opening displacements towards the corner.

It should be mentioned that the non-linear von Karman plate equations listed in Section 4, which are the basis for the results presented in this section normally are applied to cases where the in plane displacements of the plate

are of much lower magnitude than the out of plane displacement. For the present problem, unless the angle φ is close to 0°, the symmetry conditions in (12) at $y = b$, induce in-plane displacements of the same order of magnitude as the out-of-plane displacement. In order to verify the accuracy of the results presented in this section, an incremental numerical scheme not based on the assumption that in plane displacements are smaller than out of plane displacements has been set up. The details of this scheme are given in the appendix, and for none of the results presented there were significant disagreements between these results. The numerical scheme given in the appendix has also been applied in an analysis investigating if the centre line of symmetry has a tendency to rotate. In that case symmetry conditions were not imposed at the centre line, but rather a small imperfection in the geometry was introduced leading to an initial rotation of the centre line. During the incremental loading procedure, the rotation of the corner was monitored to see if there were sudden changes indicating a bifurcation into a non-symmetric shape. For the range of parameters investigated there were no indications of such bifurcations.

6 Contacting crack faces

The curves in Figs. 6-8 are terminated when the mode mixity ψ reaches the value -90° indicating contact between the crack faces over distances comparable to the layer thickness. The model used to describe the problem presupposes no contact between the layer and the substrate at the interface crack, which is what is reflected in a restriction for admissible values of ψ. It is seen from the results, that the range of stress values in which solutions exist becomes strongly limited already at small values of the angle φ. The trends in the results for the energy release rates in cases where the mode mixity exceeds the range where large scale contact takes place should, however, be obvious by Figs. 6, 7 and 8.

In cases where there is no friction between the cracks the expressions for G_l and G_{ss} are unaffected by large scale contact as long as it is realised that the crack sides are under pure mode 2 loading conditions. For cases with frictional sliding between the crack faces, the energy release rate is reduced as analysed in Thouless *et al.* (1992) for constant friction and Stringfellow and Freund (1993) for Coulomb friction.

Thouless *et al.* (1992) present their results for buckling driven delamination and edge delaminations in the planar case in a form which here can be applied to the geometry in Fig. 2. Thouless *et al.* (1992) introduce the mode 2 stress intensity factor, K_2, as a linear function of the membrane force, ΔN, and the constant friction stress, τ, and relate M and ΔN through

linear conditions

$$K_2/t^{1/2} = C_1\tau + C_2\Delta N/t$$
$$M/t^2 = C_3\tau + C_4\Delta N/t \tag{27}$$

where the C's are functions of the length of the contact zone between the crack faces, which are tabulated in Thouless *et al.* (1992) using continuous distribution of dislocations. In the present case, M and ΔN are determined by (18)-(20). For a given friction stress, the length of the contact zone can be specified in the second condition in (27), which combined with the exact asymptotic expression (25) in the limit of small stresses leads to a second order equation in η

$$\eta^2\left(C_4 + \frac{\tau}{\sigma_0}C_3\right) - \frac{\eta}{2} + \frac{\tau}{\sigma_0}C_3 = 0 \tag{28}$$

By the solution, the mode 2 stress intensity factor can be obtained by the first of the conditions in (27).

The effects of contacting crack faces on the energy release rates along the side and the front are demonstrated in Fig. 10, which is obtained by combination of the tabulated values of the C's in (27) and the asymptotic expression in (25). A mixed mode fracture criterion is not imposed prior to crack closure, and it seen that frictional sliding due to contacting crack faces alone can explain a transition of the failure mode from propagation along the sides to propagation along the front. A such transition is expected when the curves for G_l and G_{ss} intersect. The plot in Fig. 10 is carried out in the case of no elastic mismatch $\alpha = \beta = 0$. Other values of elastic mismatch parameters would change the values of the C parameters in (27) and the value of the angle ω in (25), which in turn affects the mode adjusted energy release rate in (24) through ψ.

7 Conclusion

An analysis of buckling driven delamination at a sharp corner has been carried out. When the corner angle φ is zero, the problem corresponds to delamination on a flat substrate, where the stress in the layer has to exceed a certain critical value before any deflection of the layer can occur and thus result in loading of the crack front. When assumes a non-zero value, the problem is no longer a bifurcation problem and solutions exist for stresses below the critical load for a plate σ_c. Semi-analytical results for the energy release rate and the mode mixity along the crack front have been obtained by coupling the theory of thin shells to elastic interface fracture mechanics. The results require numerical solution of an implicit equation. Solutions are verified by comparing to pure numerical results using an incremental loading scheme. It has also been checked that bifurcation into non-symmetric deformations at the corner are not expected.

The energy release rate along the propagating crack front is obtained by an assumed path independent integral leading the crack from an initial state far in front of the propagating front to its final state far behind. The path independence relies on an assumption that the released energy during crack propagation is independent of the mixed mode 1, 2 and 3 loading history bringing the crack from its initial to its final state. Steady state crack propagation along the front compared to crack propagation at the sides takes place for the case where the energy release rate is highest. In the limit of infinitely small stresses, analytical results for the energy release rate and mode mixity along the sides as well as the steady state energy release rate along the front have been obtained.

It has been shown that mode dependent interface fracture toughness can explain the existence of steady state delamination. It has been shown that crack closure takes place at sufficient high stress levels like the case for the flat substrate. It has also been shown, that the range of stress values in which the crack is open is strongly limited compared to when $\varphi = 0^\circ$ even for small angles φ.

The analytical results for the fracture mechanical parameters in the limit of small stresses have been combined with previously obtained results for the effects of friction between the crack faces when crack closure occurs. By these results it is shown that effects of frictional sliding of the contacting crack faces in these cases can explain a transition in failure mode from crack propagation along the sides to crack propagation along the front. This means that such failure modes may exist also in systems where the fracture criterion prior to crack closure is mode independent.

Acknowledgements

KDS and JC were supported from the Danish Technical Research Council; KDS through the Framework Programme "Interface Design of Composite Materials" (STVF fund No. 26-03-0160) and JC through the Framework Programme "Efficient Conversion of Renewable Energy using Solid Oxide Fuel Cells" (STVF fund No. 2058-03-0014).

References

Biot, M.A. (1965). *Mechanics of incremental deformation*. Wiley, New York.

Byskov, Esben, Jes Christoffersen, Claus Dencker Christensen and Johannes Sand Poulsen (2002). Kinkband formation in wood and fiber composites—morphology and analysis. *International Journal of Solids and Structures* **39**, 3649–3673.

Cao, H.C. and A.G. Evans (1989). An experimental study of the fracture resistance of bimaterial interface. *Mechanics of Materials* **7**, 295–305.

Chai, H., C.D. Babcock and W.G. Knauss (1981). One dimensional modelling of failure in laminated plates by delamination buckling. *International Journal of Solids and Structures* **17**, 1069–1083.

Evans, A.G. and J.W. Hutchinson (1989). Effects of non-planarity on the mixed mode fracture resistance of bimaterial interfaces. *Acta Materialia* **37**, 909–916.

Faulhaber, S., C. Mercer, M.-W. Moon, J.W. Hutchinson and A.G. Evans (2006). Buckling delamination in compressed multilayers on curved substrates with accompanying ridge cracks. *Journal of the Mechanics and Physics of Solids* **54**, 1004–1028.

Hutchinson, J.W. (2001). Delamination of compressed films on curved substrates. *Journal of the Mechanics and Physics of Solids* **49**, 1847–1864.

Hutchinson, J.W. and Z. Suo (1992). Mixed mode cracking in layered materials. *Advances in Applied Mechanics* **29**, 63–191.

Hutchinson, J.W., M.Y. He and A.G. Evans (2000). The influence of imperfection on the nucleation and propagation of buckling driven delaminations. *Journal of the Mechanics and Physics of Solids* **48**, 709–734.

Jensen, H.M. (1990). Mixed mode interface fracture criteria. *Acta Metallurgia et Materialia* **38**, 2637–2644.

Jensen, H.M. and I. Sheinman (2001). Straight-sided, buckling-driven delamination of thin layers at high stress levels. *International Journal of Fracture* **110**, 371–385.

Jensen, H.M. and I. Sheinman (2002). Numerical analysis of buckling-driven delamination. *International Journal of Solids and Structures* **39**, 3373–3386.

Jensen, H.M., J.W. Hutchinson and K.-S. Kim (1990). Decohesion of a cut prestressed film on a substrate. *International Journal of Solids and Structures* **26**, 1099–1114.

Kyriakides, S. (1994). Propagating instabilities in structures. *Advances in Applied Mechanics* **30**, 67–189.

Liechti, K.M. and Y.-S. Chai (1991). Biaxial loading experiments for determining interfacial fracture toughness. *Journal of Applied Mechanics* **58**, 680–687.

Moon, M.-W., H.M. Jensen, J.W. Hutchinson, K.H. Oh and A.G Evans (2002*a*). The characterization of telephone cord buckling of compressed thin films on substrates. *Journal of the Mechanics and Physics of Solids* **50**, 2355–2377.

Moon, M.-W., J.-W Chung, K.-R. Lee, K.H. Oh, R. Wang and A.G Evans (2002*b*). An experimental study of the influence of imperfections on the buckling of compressed thin films. *Acta Materialia* **50**, 1219–1227.

Mumm, D.R. and A.G. Evans (2000). Kink band formation and band broadening in fiber composites under compressive loading. *Acta Mat.* **43**, 2943–2958.

Niordson, F. (1985). *Shell Theory*. North-Holland.

Persson, Å.H. (2007). High temperature oxidation of slurry coated interconnect alloys. PhD thesis. Technical University of Denmark.

Sørensen, B.F., E. Jørgensen, C.P. Debel, F.M. Jensen, H.M. Jensen, T.K. Jacobsen and K.M. Halling (2004). Improved design of large wind turbinde blade of fibre composites based on studies of scale effetcs (phase 1). Risø Report Risø-R-1390(EN).

Sørensen, K.D. and H.M. Jensen (2008). Buckling-driven delamination in layered spherical shells. *Journal of the Mechanics and Physics of Solids* **56**, 230–240.

Stringfellow, R:G: and L.B. Freund (1993). The effect of interfacial friction on the buckle-driven spontaneous delamination of a compressed thin layer. *International Journal of Solids and Structures* **30**, 1379–1396.

Suo, Z. and J.W. Hutchinson (1990). Interface crack between two elastic layers. *International Journal of Fracture* **43**, 1–18.

Thouless, M.D., J.W. Hutchinson and E.G. Liniger (1992). Plane-strain, buckling-driven delamination of thin layers: Model experiments and mode ii fracture. *Acta Materialia* **40**, 2639–2649.

Tvergaard, V. and J.W. Hutchinson (1993). The influence of plasticity on mixed mode interface toughness. *Journal of the Mechanics and Physics of Solids* **41**, 1119–1135.

Tvergaard, V. and J.W. Hutchinson (2008). Mode iii effects on interface delamination. *Journal of the Mechanics and Physics of Solids* **56**, 215–229.

Appendix

An incremental numerical approach to verify the semi-analytical results in Section 5 has been carried out as outlined below following Byskov *et al.* (2002). A planar beam element with conventions for displacements u and v, arc length s, angle of beam tangent with x-axis θ, shear stress T, normal stress N, and moment M defined in Fig. 11 is introduced. With $\dot{(\,)}$ denoting the increment of a quantity the kinematical relations allowing for arbitrary rotations and strains are

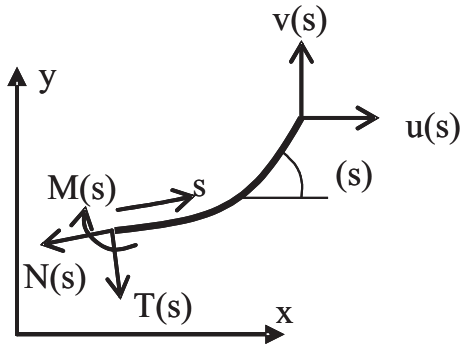

Figure 11: Sketch of sign conventions for displacements and generalised forces for beam element.

$$\frac{du}{ds} = \varepsilon\cos\theta - \dot{\theta}\sin\theta \quad , \quad \frac{dv}{ds} = \varepsilon\sin\theta + \dot{\theta}\cos\theta \tag{29}$$

where ε is the strain rate, which along with the bending rate κ is given by

$$\varepsilon = \frac{d\dot{s}}{ds} \quad , \quad \kappa = \frac{d\dot{\theta}}{ds} \tag{30}$$

The two incremental force equilibrium equations and the moment equilibrium equation are given as

$$\frac{d\dot{T}}{ds} = -\dot{N}\frac{d\theta}{ds} - N\kappa \quad , \quad \frac{d\dot{N}}{ds} = \dot{T}\frac{d\theta}{ds} + T\kappa \quad , \quad \frac{d\dot{M}}{ds} = -\dot{T} - T\varepsilon \tag{31}$$

The constitutive relations assuming linear elasticity are

$$\dot{N} = Et\varepsilon - \dot{\sigma}_0 t \quad , \quad \dot{M} = \frac{1}{12}Et^3\kappa \tag{32}$$

By introducing the curvature k

$$k = \frac{d\theta}{ds} \tag{33}$$

and non-dimensional quantities according to

$$\begin{aligned} \tilde{u} = \frac{u}{t} \quad , \quad \tilde{v} = \frac{v}{t} \quad , \quad \tilde{k} = bk \quad , \quad \tilde{\kappa} = b\kappa \\ \tilde{T} = \frac{T}{Et} \quad , \quad \tilde{N} = \frac{N}{Et} \quad , \quad \eta_1 = \frac{b}{t} \quad , \quad \tilde{s} = \frac{s}{b} \end{aligned} \tag{34}$$

the following six coupled, linear ordinary first-order differential equations are obtained

$$\begin{aligned} \frac{d\tilde{u}}{d\tilde{s}} &= \eta_1 \left(\varepsilon \cos\theta - \dot{\theta} \sin\theta \right) \quad , \quad \frac{d\tilde{v}}{d\tilde{s}} = \eta_1 \left(\varepsilon \sin\theta + \dot{\theta} \cos\theta \right) \quad , \quad \frac{d\dot{\theta}}{d\tilde{s}} = \tilde{\kappa} \\ \frac{d\tilde{\kappa}}{d\tilde{s}} &= -12\eta_1^2 \left(\dot{\tilde{T}} + \tilde{T}\varepsilon \right) \quad , \quad \frac{d\varepsilon}{d\tilde{s}} = \dot{T}\tilde{k} + \tilde{T}\tilde{\kappa} \\ \frac{d\dot{\tilde{T}}}{d\tilde{s}} &= -\left(\varepsilon - \frac{\pi^2}{12\eta_1^2} \left(\frac{\dot{\sigma}_0}{\sigma_c} \right) \right) \tilde{k} - \tilde{N}\tilde{\kappa} \end{aligned} \tag{35}$$

The boundary conditions are clamped at $s = 0$ and either symmetry conditions at the centre $s = b$ or when symmetry is not assumed, clamped conditions at $s = 2b$ i.e.

$$\begin{aligned} \tilde{u}(0) &= \tilde{v}(0) = \dot{\theta}(0) = 0 \quad \text{and} \\ \tilde{u}(1) &= \dot{\tilde{T}}(1) - \left(\frac{\pi^2}{12\eta_1^2} \frac{\dot{\sigma}_0}{\sigma_c} - \varepsilon(1) \right) \tan\varphi = \dot{\theta}(1) = 0 \quad \text{or} \\ \tilde{u}(2) &= \tilde{v}(2) = \dot{\theta}(2) = 0 \end{aligned} \tag{36}$$

The linear set of equations (35) with boundary conditions (36) are integrated numerically.

ON THE SIMULATION OF KINK BANDS IN FIBER REINFORCED COMPOSITES

Kim D. Sørensen*, Lars P. Mikkelsen**
and Henrik M. Jensen*

* Department of Civil Engineering, Aalborg University,
9000 Aalborg, Denmark
** Materials Research Department, Risø,
4000 Roskilde, Denmark

ABSTRACT

Simulations of kink band formation in fiber reinforced composites are carried out using the commercial finite element program ABAQUS. A smeared-out, plane constitutive model for fiber reinforced materials is implemented as a user subroutine, and effects of fiber misalignment on elastic and plastic deformation are studied under plane strain conditions.

Keywords: Kink band, constitutive model, ABAQUS, fiber misalignment

1. INTRODUCTION

Failure by kinking in fiber reinforced composites has been the subject of a number of recent investigations. It has been found that the compressive failure strength is considerably lower than the tensile strength, typically in the order of 50 to 60 percent for carbon fiber composites (Kyriakides et al., 1995). It has also been found that the compressive strength is governed by plastic yielding in the matrix (Budiansky, 1983), and futhermore, that small misalignments of the fibers have a large influence on the compressive strength, see Kyriakides et al. (1995). Several investigations of compression of a fiber reinforced material under the assumption of perfectly aligned fibers have predicted bifurcations stresses much higher than results obtained from experiments. Liu, Fleck and Sutcliffe (2004) include the effect of random waviness of the fibers using a Cosserat smeared-out finite element model.

In Kyriakides et al. (1995) the problem of predicting compressive strength for fiber reinforced materials is approached through an idealized model composite, with individual discretization of fiber and matrix material, and this two-dimensional michromechanical model was later (Kyriakides et al.,1998) extended to a three dimensional model. In these investigations the post-buckling respone is also studied, and it is shown that deformation localizes into well-defined bands of bent fibers.

Kink band formation in fiber reinforced materials was investigatated in Christoffersen and Jensen (1996) and in Jensen and Christoffersen (1997), where a plane constitutive model for perfectly bonded layered materials was introduced. It was found that this model contains essentially the same information in one point of the material as a complete finite element discretization of a representative volume element, like the model introduced in Kyriakides et al. (1995), and furthermore, that the critical stress is highly influenced by fiber volume fraction and the constitutive behavior of the constituents. Another conclusion is that the kink stress is reduced by taking non-linearity of the fibers into account compared to the predicted critical stress assuming linear-elastic fibers.

In the present study, a smeared-out plane constitutive model, as formulated by Christoffersen and Jensen (1996), is implemented as a user subroutine in the finite element program ABAQUS. Effects of fiber misalignment for elastic and plastic response are studied, and qualitatively compared to earlier results.

2. IMPLEMENTATION OF THE CONSTITUTIVE MODEL

For a detailed description of the constitutive model used in these kinkband simulations, see Jensen and Christoffersen (1997) and Christoffersen and Jensen (1996).

2.1 The constitutive model.

The general relations between rates of Cauchy stress and the strain rates in three dimensions are given by

$$\dot{\sigma}_{ij} = L_{ijkl}\epsilon_{kl} \tag{1}$$

where L_{ijkl} are the elastic-plastic tangent moduli. The strain rates are given by

$$\epsilon_{ij} = \tfrac{1}{2}\left(v_{i,j} + v_{j,i}\right) \tag{2}$$

with $v_{i,j}$ denoting the components of the gradient of velocity components v_i.

The two-dimensional constitutive equations implemented in ABAQUS are given in the form

$$\dot{s}_{ij} = C_{ijkl}v_{l,k}, \quad i,\ j,\ k,\ l \in \{1,2\} \tag{3}$$

where $\dot{s}_{ij}$ are components of the nominal stress rate, $v_{i,j}$ are components of the gradient of velocity components v_i, and C_{ijkl} are components of the tensor of nominal moduli, and from this formulation L_{ijkl} is found by the relation

$$L_{ijkl} = C_{ijkl} + \tfrac{1}{2}\delta_{il}\sigma_{kj} + \tfrac{1}{2}\delta_{ik}\sigma_{lj} + \tfrac{1}{2}\sigma_{il}\delta_{kj} - \tfrac{1}{2}\sigma_{ik}\delta_{lj}, \quad i,\ j,\ k,\ l \in \{1,2\} \tag{4}$$

by futhermore using the assumption $\tau_{ij} \approx \sigma_{ij}$, with τ_{ij} being components of Kirchoff stress.

The components of the tensor of nominal moduli C_{ijkl} are found from a mixture of fiber and matrix properties.

The constitutive model is based on three assumptions:

- Material lines parallel with the fibers are subject to a common stretching and rotation

- Planes parallel with the fibers transmit identical tractions
- The material of the constituents is elastic or elastic-plastic

The first of these assumptions correspond to a Voigt estimate for effective material properties whereas the second corresponds to a Reuss estimate. The third assumption is a standard specification of time independant materials.

The expressions for C_{ijkl}, the components of the tensor of nominal moduli, can be found in Christoffersen and Jensen (1996).

2.2 The behavior of the constituents.

For both constituents we have the relations

$$\dot{s}^c_{ij} = C^c_{ijkl} v^c_{l,k}, \tag{5}$$

similar to equation 3. Furthermore, both materials are assumed to be characterized by a power-law hardening with isotropical hardening. The power-law is given by

$$\epsilon = \begin{cases} \frac{\sigma}{E} & , \ \sigma \leq \sigma_y \\ \frac{\sigma_y}{E}\left[\frac{1}{n}\left(\frac{\sigma}{\sigma_y}\right)^n - \frac{1}{n} + 1\right] & , \ \sigma > \sigma_y \end{cases} \tag{6}$$

where σ_y is the yield stress of the material and n the hardening parameter. From this relation the tangentmodulus E_t is found, and subsequently the values of L^c_{ijkl}.

In the kink-band simulations in the present paper, yielding only occurs in the matrix material, and thus the fibers are treated as linear elastic.

2.3 ABAQUS implementation.

The user subroutine UMAT in ABAQUS is used to implement the material behavior of the composite. In this routine, stresses in fibers and matrix are updated within each increment, and the elastic-plastic moduli are calculated by mixture of the properties of the constituents. The moduli L_{ijkl} are determined from equation 4 and this value is returned to ABAQUS from UMAT. ABAQUS uses an updated Lagrangian formulation.

The model is implemented as a plane strain model, but can also be formulated for plane stress situations. In the present study, the fiber volume fraction is assumed to remain constant throughout the deformation.

Further details regarding the implementation of a constitutive model in ABAQUS can be found in Dunne and Petrinic (2005).

3. RESULTS

In this section, results for simulation of kink-band formation, and the response of compression of a single element, are presented. In the simulations, a rectangular block of fiber reinforced material, as shown in Fig. 1, is analyzed. The block is loaded under plane strain conditions, and has the dimensions $L = 10$ and $H = 3$ with the fiber direction outside the

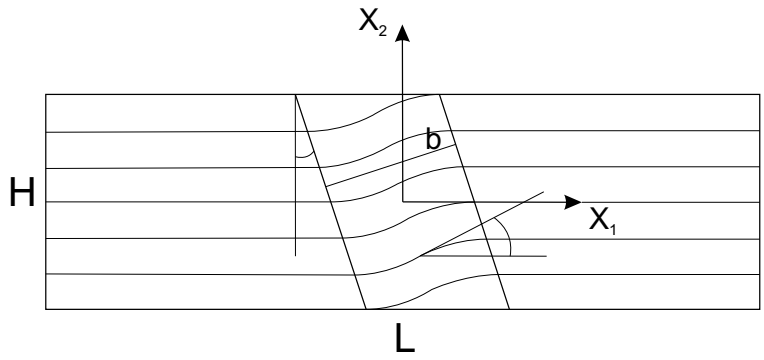

Fig. 1: Kink band geometry

kink band coinciding with the x_1-axis. Furthermore, the displacements u_1 and u_2 satisfy the boundary conditions

$$u_1 = 0 \; on \; x_1 = -\tfrac{L}{2} \tag{7}$$

$$u_2 = 0 \; on \; (x_1, x_2) = \left(-\tfrac{L}{2}, -\tfrac{H}{2}\right) \tag{8}$$

The width of the imperfection is b and β is the angle of the kink band. Inside the kink band the fibers are assumed to be at an angle ϕ, and this imperfection is given by the expression:

$$\phi\left(x_1, x_2\right) = \tfrac{1}{2}\phi_m \left[\cos\left(\frac{2\pi\cos\beta}{b}\left(x_1 + x_2\tan\beta\right)\right) + 1\right] \tag{9}$$

where ϕ_m is the value of the angle in the middle of the kink-band. In all simulations, the values $b = 2$ and $\beta = 5^\circ$ are used.

The material parameters used in these simulations are found in Kyriakides et al. (1995), with superscripts f and m denoting fiber and matrix respectively:

$$\nu^f = 0.263, \; \nu^m = 0.356, \; \frac{\sigma_y^f}{E^f} = 0.019, \; \frac{\sigma_y^m}{E^m} = 0.013 \tag{10}$$

In all simulations, a fiber volume fraction of $c^f = 0.6$ is being used. The hardening parameters are chosen to be $n^m = 4.5$ and $n^f = 2.5$, so the power-law curve closely resembles the Ramberg-Osgood curve used in Jensen and Christoffersen (1997), and results are obtained for $E^f/E^m = 35$ and $E^f/E^m = 100$.

The dotted green curve in Fig. 2 shows the material response under compression of an element of the fiber reinforced material. In Fig. 2, the plastic deformation of the matrix material is suppressed. The material response is modeled using one 4-node element with 2×2 Gauss integration points. The fibers are given a small initial homogenous inclination of 1°. During the compressive deformation the fiber inclination will increase, resulting in a lower overall stiffness of the composite material. Nevertheless, for a stiffness ratio of the fiber/matrix system given by $E^f/E^m = 35$ the behavior is rather linear, whereas a stiffness ratio of $E^f/E^m = 100$ will result in a much more pronounced non-linear material response. However, even for this stiffness ratio the material will not experience a material softening behavior. Therefore, a localized deformation state in the rectangular block (Fig. 1) is not expected and is not found. Instead of a localized deformation state, an imperfection insensitive overall Euler buckling mode is developed as shown in Fig. 3. The red curve in Fig. 2

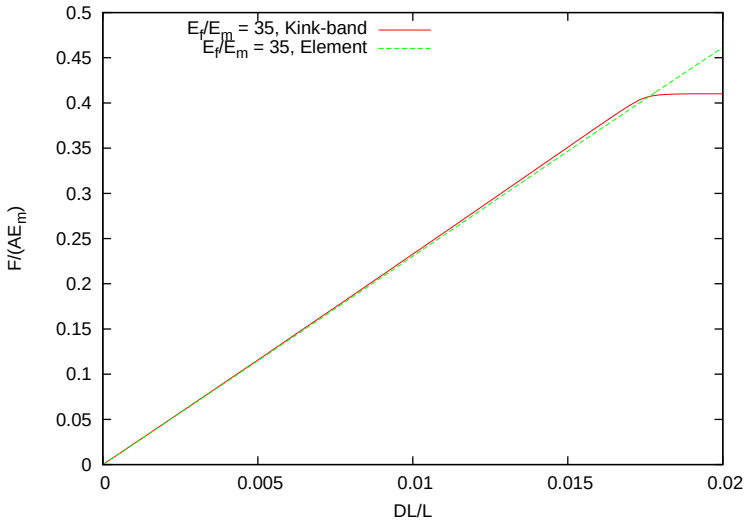

Fig. 2: Elastic deformation

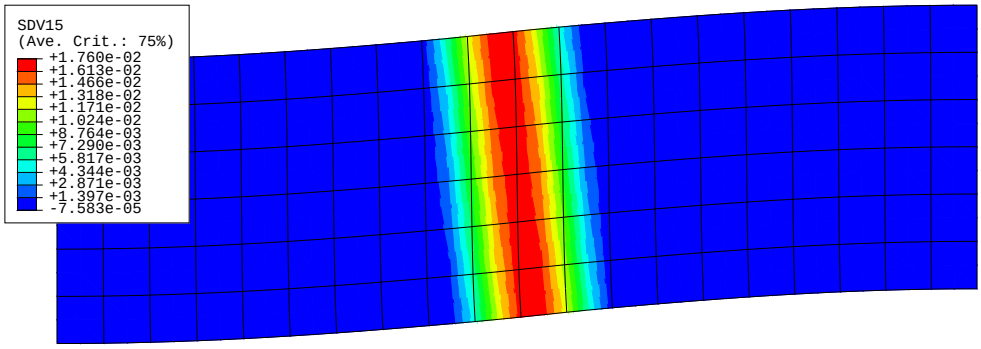

Fig. 3: Contourplot of imperfection

shows the corresponding load versus shortening curve for a rectangular block, indicating a maximum load carrying capacity of approximately $F/(AE^m) = 0.42$. In addition to the deformed mesh, Fig. 3 shows a contourplot of the initial prescribed misalignment of the fibers, with a maximum value of $\phi_m = 0.0176\ rad$ at the center of the kink band, corresponding to an imperfection of $\phi_m = 1°$.

In Fig. 4, the load-displacement curves for one single element, Fig. 4a, and for a block of material, Fig. 4b, are given for the stiffness ratio of the fiber/matrix system $E^f/E^m = 35$. In contrast to Fig. 2, plastic yielding occurs in the following simulation in the matrix material. During compressive loading it can be seen from Fig. 4a, that the smeared out model show extensive material softening and actually also snap-back behavior. Consequently the deformation state in the rectangular block localizes into a kink-band as shown in Fig. 5. The load-displacement curves are linear until a kink stress is reached and for sufficiently small angles of fiber misalignment, the phenomenon of snap-back occurs. From Fig. 4 it can be seen that the critical stress is very sensitive to the initial fiber-misalignment. For instance, for the kink-band formation in the block of material the critical stress almost doubles when the maximum angle of fiber-misalignment ϕ_m is reduced from $5°$ to $2°$.

A contour plot of the effective plastic strains in the matrix material during kink band

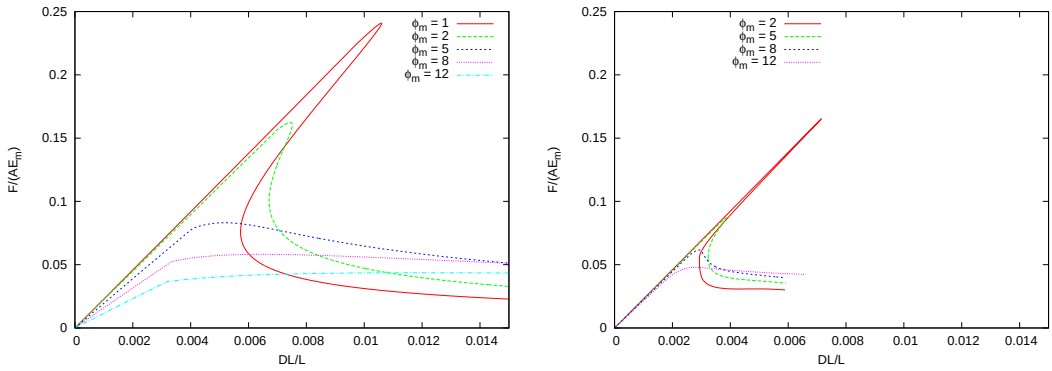

Fig. 4: Plastic deformation $E^f/E^m = 35$

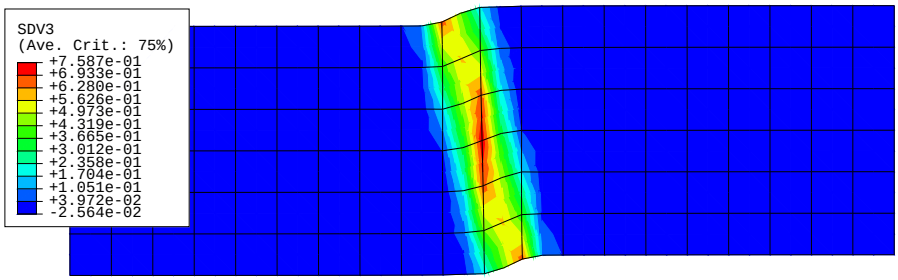

Fig. 5: Contour plot of effective plastic strain in the matrix material

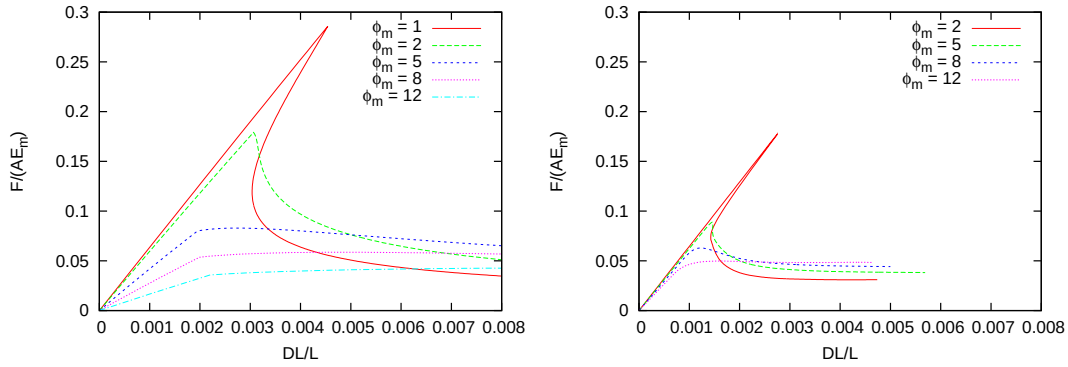

Fig. 6: Plastic deformation $E^f/E^m = 100$

formation is shown in Fig. 5.

The load-displacement curves for one single element and for a block of material, are shown in Fig. 6 for the stiffness ratio of the fiber/matrix system $E^f/E^m = 100$. These curves demonstrate a behavior similar to the one where $E^f/E^m = 35$. The implementation of the constitutive model does not include a material length-scale, and consequently the solutions show strong mesh dependency. This is illustrated in Fig. 7 which shows the load-displacement curves using four different meshes. All curves are found using the fiber misalignment variation (9) with $\phi_m = 8°$. Similar to what is obtained by e.g. (Pamin, 1994) a more brittle post-localization behavior are obtained when the mesh is refined. From Fig. 8 it can be seen that the kink-band formation occurs in one row of elements. Not only the

post-necking behavior, but also the load carrying capacity is seen to be influenced by the mesh size.

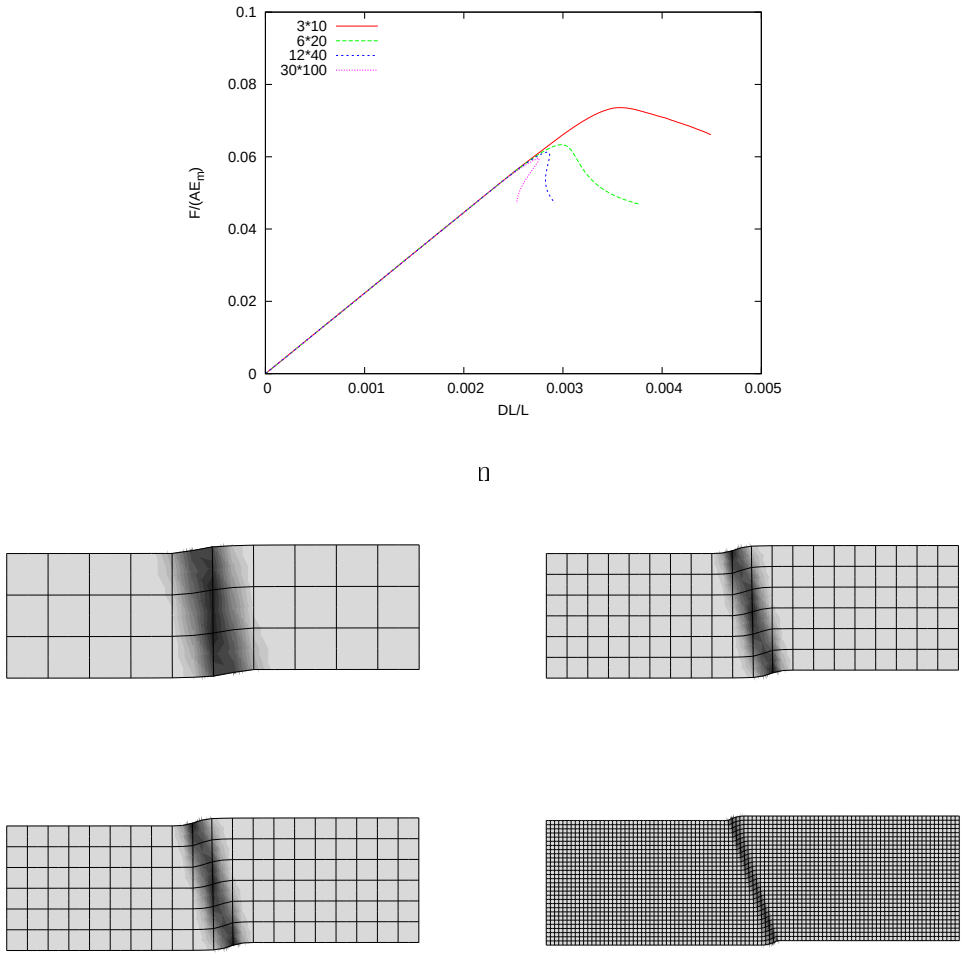

Fig. 8: Kink band mesh dependency

4. DISCUSSION

A plane constitutive model for fiber reinforced composites is implemented in ABAQUS as a user subroutine. It is demonstrated that the model qualitatively produces similar behavior as a micro-mechanical model, with regards to kink band development.The implementation of the model in ABAQUS does not include a material length-scale and therefore the kink-band will show strong mesh dependency. The implementation of the smeared-out composite material model in a finite element model has some immediately future applications, for instance kink-band development in more complex structures, such as a plate with a hole subject to compression. Other possible application is simulation of competing compressive failure mechanisms such as buckling and kink-band development in large fiber composite structures.

ACKNOWLEDGEMENT

The work has been financial supported by the Danish Technical Research Counsil through the project 'Interface Design of Composite Materials'.

REFERENCES

Budiansky, B. (1993). Micromechanics. Computers & Structures 16, 3-12.

Christoffersen, J., and Jensen, H.M. (1996). Kinkband analysis accounting for the microstructure of fiber reinforced materials. Mechanics of Materials 24, 305-315

Dunne, F., and Petrinic, N. (2005). Introduction to Computational Plasticity. Oxford University Press.

Hsu, S.-Y., Vogler, T.J., and Kyriakides, S. (1998). Compressive Strength Predictions for Fiber Composites. Journal of Applied Mechanics 65

Jensen, H.M., and Christoffersen, J. (1997). Kink Band Formation in Fiber Reinforced Materials. J. Mech. Phys. Solids 45, 1121-1136.

Kyriakides, S., Arseculeratne, R., Perry, E. J. and Liechti, K. M. (1995). On the compressive failure of fiber reinforced composites. Int. J. Solids Struct. 32, 689-738.

Liu, D., Fleck, N. A., and Sutcliffe, M. P. F. (2004). Compressive Strength of Fibre Composites with Random Fibre Waviness. J. Mech. Phys. Solids 52, 1481-1505.

Pamin, J.K. (1994). Gradient-dependent plasticity in numerical simulation of localization phenomena. PhD-thesis, Delft University Press, The Netherlands.

Pane, I. and Jensen, H.M. (2004) Plane strain bifurcation and its relation to kinkband formation in layered materials. European Journal of Mechanics A/Solids 23, 359-371

Implementation of a Constitutive Model in ABAQUS

Kim D. Sørensen Lars P. Mikkelsen* Henrik M. Jensen**

Department of Civil Engineering
Aalborg University
Sohngaardsholmsvej 57, DK-9000 Aalborg, Denmark

*Materials Research Department
Risø,
DK-4000 Roskilde, Denmark

**Aarhus Graduate School of Engineering
University of Aarhus
Dalgas Avenue 4, DK-8000 Århus C, Denmark

Abstract

A constitutive model for fiber reinforced composite materials has been implemented in ABAQUS. The model has been developed to study kink band formation, and applications to cases where this formation occurs are used as examples to demonstrate the model, although this is not a general restriction. The development of the user subroutine for implementing the model in ABAQUS is discussed in detail. Special emphasis is placed on the performance of ABAQUS with the model with respect to mesh dependence of the results.

1 Introduction

Fiber composites loaded in compression parallel to the fibers may fail by localization of strains into kink bands. Structural components based on composite materials, which are subject to changing load histories, are often designed with this failure mode as the most critical. Fig. 1 shows an idealization of the kink band geometry.

The formation of kink bands was initially studied in geology. One of the first papers on kink band formation in fiber composites was Rosen (1965) where a linear elastic analysis was carried out treating the fiber/matrix interaction by a planar model of beams on an elastic foundation. The critical

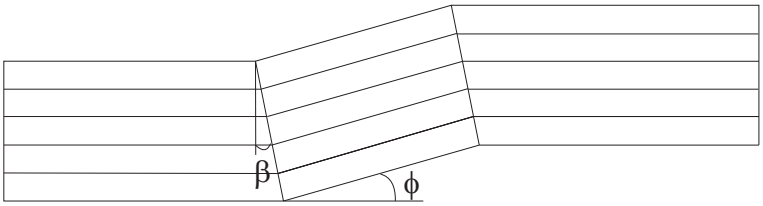

Figure 1: Idealization of kink band geometry with kink band orientation β and fiber rotation ϕ.

stress for kink band formation was estimated as

$$\sigma_{11} = G \tag{1}$$

where G is the elastic shear modulus of the composite material. Later Argon (1972) formulated a planar model, which emphazised the importance of two effects not taken into account in Rosen's analysis: Misalignments of fibers relative to the direction of loading, and plastic deformation of matrix material. Budiansky (1983) unified the approaches of Rosen (1965) and Argon (1972), which allowed for later extensions to multi axial loading conditions etc. see for instance Fleck and Budiansky (1991) and Slaughter *et al.* (1993). The critical stress for kink band formation was obtained as

$$\sigma_{11} - \sigma_{22} + G + 2\sigma_{12}\tan\beta + E_T \tan^2\beta = 0 \tag{2}$$

where E_T is the transverse modulus of the composite. The works of Argon (1972), Budiansky (1983) and Fleck and Budiansky (1991) had shown that fiber misalignments and plastic deformation was important for kink band formation and a constitutive model was developed in Christoffersen and Jensen (1996), which allowed for these effects. The conditions for kink band formation were modelled as loss of ellipticity of the governing incremental equilibrium equations Rice (1976). In the limit of infinitely stiff fibers, an exact solution for the critical stress for kink band formation could be obtained, which when specialised to $\beta = 0$ results in

$$\sigma_{11} - \sigma_{22} + \frac{1}{c^m}\left(L^m_{1212} - \frac{\sigma^m_{11} - \sigma_{22}}{2}\right) = 0 \tag{3}$$

where L_{ijkl} are incremental moduli for the matrix material relating Jaumann rates of Kirchhoff stresses to strain rates as explained in greater detail in the following section.

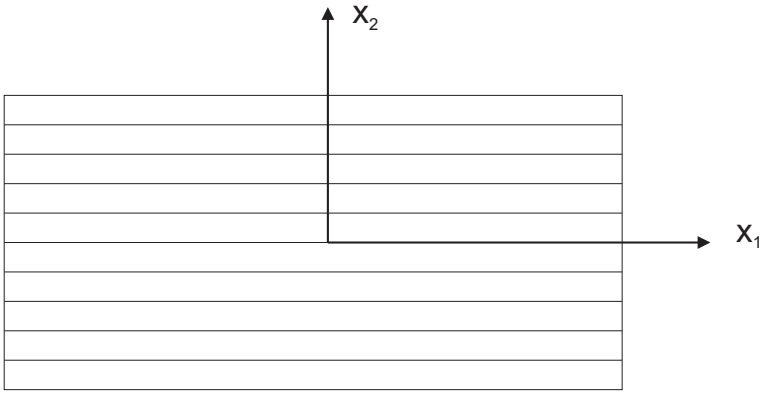

Figure 2: Block of planar composite material with alternating layers of matrix and fiber material.

2 Constitutive Model and Implementation

2.1 The Constitutive Model

A planar model is formulated for the composite material in Fig. 2 based on the assumptions that the fibers and the matrix material are described by time-independent plasticity theories relating Jaumann rates of Kirchhoff stresses $\hat{\tau}_{ij}$ to strain rates ε_{ij} ($\varepsilon_{ij} = \frac{1}{2}(v_{i,j} + v_{j,i})$ with v_i as displacements and a comma denoting partial differentiation) in the form

$$\begin{aligned} \hat{\tau}^f_{ij} = L^f_{ijkl}\varepsilon^f_{kl} \quad \text{or} \quad \varepsilon^f_{ij} = M^f_{ijkl}\hat{\tau}^f_{kl} \quad \text{and} \\ \hat{\tau}^m_{ij} = L^m_{ijkl}\varepsilon^m_{kl} \quad \text{or} \quad \varepsilon^m_{ij} = M^m_{ijkl}\hat{\tau}^m_{kl} \end{aligned} \tag{4}$$

where the superscripts refer to fibers or matrix material, and in the following constitutive properties without a superscript denote composite properties. In (4), L_{ijkl} denotes the tensor of instantaneous moduli and M_{ijkl} denotes the tensor of instantaneous compliances, and furthermore, the summation convention is adopted for repeated index. In the applications we set Kirchhoff stresses equal to Cauchy stresses and thus assume that local changes in density due to elastic deformations are negligible.

Two classical models for calculating the constitutive response of the composite material for small strain and small rotations are obtained by assuming identical strains in the fibers and matrix (the Voigt model) or by assuming identical stress is the fiber and the matrix (the Reuss model) leading to

$$\begin{aligned} L_{ijkl} &= c^f L^f_{ijkl} + c^m L^m_{ijkl} \text{ (Voigt)} \\ M_{ijkl} &= c^f M^f_{ijkl} + c^m M^m_{ijkl} \text{ (Reuss)} \end{aligned} \tag{5}$$

where c^f and c^m denote relative volume fractions of fibers and matrix material. For unidirectional fiber composites, the Voigt model is reasonable for

properties in the fiber direction, while the Reuss model is reasonable in the perpendicular direction.

When introducing the constitutive relations, which the present work is based on, valid for finite strains and rotations, it is convenient to formulate the constitutive relations as the relationship between nominal stress rates and displacement gradient $v_{i,j}$ (with a comma denoting partial differentiation) in the form

$$\dot{s}_{ij} = C_{ijkl} v_{l,k}, \quad i,\ j,\ k,\ l \in \{1,2\} \tag{6}$$

The following relations hold between L_{ijkl} and C_{ijkl}

$$L_{ijkl} = C_{ijkl} + \tfrac{1}{2}\delta_{il}\sigma_{kj} + \tfrac{1}{2}\delta_{ik}\sigma_{lj} + \tfrac{1}{2}\sigma_{il}\delta_{kj} - \tfrac{1}{2}\sigma_{ik}\delta_{lj}, \quad i,\ j,\ k,\ l \in \{1,2\} \tag{7}$$

Here, σ_{ij} denotes the Cauchy stress tensor. Let us introduce the following alternative notation for the constitutive equations (6).

$$\dot{\boldsymbol{s}}_\alpha = \boldsymbol{C}_{\alpha\beta}\boldsymbol{v}_{,\beta}, \quad \alpha,\beta \in \{1,2\} \tag{8}$$

so that the vectors $\dot{\boldsymbol{s}}_\alpha$ and $\boldsymbol{v}$ contain the componenets of the nominal stress rates and the displacements according to

$$\dot{\boldsymbol{s}}_1 = \begin{pmatrix} \dot{s}_{11} \\ \dot{s}_{12} \end{pmatrix} \quad , \quad \dot{\boldsymbol{s}}_2 = \begin{pmatrix} \dot{s}_{21} \\ \dot{s}_{22} \end{pmatrix} \quad , \quad \boldsymbol{v} = \begin{pmatrix} v_1 \\ v_2 \end{pmatrix} \tag{9}$$

and the matrices $\boldsymbol{C}_{\alpha\beta}$ are given by

$$\begin{aligned} \boldsymbol{C}_{11} &= \begin{pmatrix} C_{1111} & C_{1112} \\ C_{1211} & C_{1212} \end{pmatrix} \quad \boldsymbol{C}_{12} = \begin{pmatrix} C_{1121} & C_{1122} \\ C_{1221} & C_{1222} \end{pmatrix} \\ \boldsymbol{C}_{21} &= \begin{pmatrix} C_{2111} & C_{2112} \\ C_{2211} & C_{2212} \end{pmatrix} \quad \boldsymbol{C}_{22} = \begin{pmatrix} C_{2121} & C_{2122} \\ C_{2221} & C_{2222} \end{pmatrix} \end{aligned} \tag{10}$$

The fibers are aligned with the x_1-axis as indicated in Fig. 2. A compromise between the assumptions in the Voigt and Reuss models is introduced by assuming that material lines parallel with the fibers are subject to a common stretching and rotation, and planes parallel with the fibers transmit identical tractions. According to this,

$$\begin{aligned} \boldsymbol{v}^f_{,1} &= \boldsymbol{v}^m_{,1} = \boldsymbol{v}_{,1} \\ \dot{\boldsymbol{s}}^f_2 &= \dot{\boldsymbol{s}}^m_2 = \dot{\boldsymbol{s}}_2 \end{aligned} \tag{11}$$

Furthermore,

$$\begin{aligned} c^f \boldsymbol{v}^f_{,2} + c^m \boldsymbol{v}^m_{,2} &= \boldsymbol{v}_{,2} \\ c^f \dot{\boldsymbol{s}}^f_1 + c^m \dot{\boldsymbol{s}}^m_1 &= \dot{\boldsymbol{s}}_1 \end{aligned} \tag{12}$$

It was shown in Christoffersen and Jensen (1996) that equations (11) and (12) along with (8) for the constituents allowed the composite moduli to be written in the form

$$\boldsymbol{C}_{\alpha\beta} = c^f \boldsymbol{C}^f_{\alpha\beta} + c^m \boldsymbol{C}^m_{\alpha\beta} - c^f c^m \left(\boldsymbol{C}^f_{\alpha 2} - \boldsymbol{C}^m_{\alpha 2}\right) \boldsymbol{C}^{*-1}_{22} \left(\boldsymbol{C}^f_{2\beta} - \boldsymbol{C}^m_{2\beta}\right) \tag{13}$$

where

$$\boldsymbol{C}^*_{22} = \left(c^m \boldsymbol{C}^f_{22} + c^f \boldsymbol{C}^m_{22}\right) \tag{14}$$

It was also shown that the moduli L_{ijkl} in (7) with C_{ijkl} given by (13) satisfy the symmetries

$$L_{ijkl} = L_{jikl} = L_{ijlk} \tag{15}$$

as required by objectivity, and that Betti symmetry is preserved by the model, i.e.

$$C^f_{ijkl} = C^f_{klij} \quad \text{and} \quad C^m_{ijkl} = C^m_{klij} \quad \Rightarrow \quad C_{ijkl} = C_{klij} \tag{16}$$

The constitutive relations given by (13) form the basis for the present study. Note that the first two terms in (13) can be considered as a generalisation of the Voigt model (5) to finite strains, and that the last term is a correction to this due to the static conditions in (11) and (12).

Each constituent may now be described by arbitrary time-independent plasticity theories. Here, J_2-flow theory is used to model the behavior of both constituents. Experimental results in Kyriakides *et al.* (1995) showed indications of relative weak fiber nonlinearities. The effects of this were investigated in Jensen and Christoffersen (1997) showing some influence on the critical stress for kink band initiation. The J_2-flow theory for the matrix can be formulated as the following incrementally linear relation between Jaumann rates of Kirchhoff stresses and strains (McMeeking and Rice (1975))

$$\begin{aligned} \hat{\tau}_{ij} &= L_{ijkl} \varepsilon_{kl} \\ L_{ijkl} &= G\left(\delta_{ik}\delta_{jl} + \delta_{il}\delta_{jk}\right) + \left(K - \tfrac{2}{3}G\right)\delta_{ij}\delta_{kl} - \tfrac{4}{3}\left(G - G_t\right) m_{ij} m_{kl} \end{aligned} \tag{17}$$

where superscript $()^m$ for the matrix has been omitted and δ_{ij} denotes the Kronecker delta. In (17), G and K are the elastic shear modulus and bulk modulus and G_t is the shear tangent modulus, which along with m_{ij} are given by

$$G = \frac{E}{2\left(1+\nu\right)} \quad , \quad K = \frac{E}{3\left(1-2\nu\right)} \quad , \quad \frac{1}{G_t} = \frac{3}{E_t} - \frac{1-2\nu}{E} \tag{18}$$

and

$$m_{ij} = \frac{1}{2\sigma_{eq}} \left(\sigma_{ij} - \frac{1}{3}\delta_{ij}\sigma_{kk}\right) \tag{19}$$

Here, E_t is the uniaxial tangent modulus, which requires a uniaxial true stress *vs.* logarithmic strain to be specified. This is given by

$$\epsilon = \begin{cases} \dfrac{\sigma}{E} & , \ \sigma \leq \sigma_y \\ \dfrac{\sigma_y}{E}\left[\dfrac{1}{n}\left(\dfrac{\sigma}{\sigma_y}\right)^n - \dfrac{1}{n} + 1\right] & , \ \sigma > \sigma_y \end{cases} \tag{20}$$

Furthermore, in (18) the effective von Mises' stress is given by

$$\sigma_{eq} = \sqrt{\frac{3}{2}\sigma_{ij}\sigma_{ij} - \frac{1}{2}\sigma_{ii}\sigma_{jj}} \tag{21}$$

In the following section the implementation of the model in ABAQUS is described. This implementation is an alternative to the application of the model in Pane and Jensen (2004) and to the individual discretization of fiber and matrix material described in Hsu *et al.* (1998).

2.2 User Subroutine UMAT

For a more detailed description on how to implement a constitutive model in ABAQUS, see Dunne and Petrinic (2005).

The subroutine UMAT (User MATerial) is written in FORTRAN and is used to define the constitutive behavior of a material. ABAQUS provides the deformation gradient, total strains and strain increments and the subroutine must then return the material Jacobian matrix $\partial\Delta\sigma/\partial\Delta\varepsilon$ for the constitutive model along with updated stresses. In this case the material behavior of the composite is simulated by mixing the properties of 2 materials each described by a powerhardening law.

The UMAT subroutine used in the present work contains the following steps:

1. Calculate the gradient of velocity from deformation gradient. The deformation gradient F is provided by ABAQUS and the velocity gradient, which describes the spatial rate of the velocity, is found from $v_{i,j} = \dot{F}_{ik}F^{-1}_{kj}$
2. Calculate the effective von Mises' stress for matrix and fiber according to (21)
3. Calculate tangent modulus from the uniaxial true stress *vs.* logarithmic strain curve, see (20)
4. Calculate L^f_{ijkl} and L^m_{ijkl} according to (17)
5. Calculate C_{ijkl} from (7) and (13)

6. Calculate stress increments, see Jensen and Christoffersen (1997)

$$\dot{\sigma_{ij}} = C_{ijkl} v_{l,k} - \sigma_{ij} v_{k,k} + v_{i,k} \sigma_{kj} \tag{22}$$

7. Update stresses
8. Update yield stress
9. Update plastic strains
10. Return state variables, see the following subsection
11. Return material Jacobian matrix $\partial \Delta\sigma / \partial \Delta\varepsilon$

All variables are updated using a forward Euler procedure.

2.2.1 List of Solution-dependant variables

The solution-dependant variables are variables that are updated as the analysis progresses. For instance, in order to be able to return the material Jacobian and to update the overall stresses in the composite material, it is necessary to keep track of the individual stresses in the fiber and matrix material. The UMAT utilizes a total of 16 state variables, passed from ABAQUS through the array STATEV(NSTATV), each containing imformation about every integration point. The state variables are:

- The updated yield stresses of the fiber and matrix materials - both modelled as power hardening materials
- The effective plastic strain in fiber and matrix
- β^f and β^m - two variables which will have the value 1 or 0 depending on if the material yields or not
- The stresses in the matrix material, σ^m_{11}, σ^m_{22}, σ^m_{33}, σ^m_{12}
- The stresses in the fiber material, σ^f_{11}, σ^f_{22}, σ^f_{33}, σ^f_{12}
- The initial direction of the fibers and the current rotation

2.2.2 List of Material Constants

To the matrix and fiber material 9 material properties are associated: 2 Young's moduli, E_m and E_f, 2 Poisson's ratios, ν^m and ν^f, 2 initial yield stresses, σ^m_y and σ^f_y, 2 hardening parameters, n^m and n^f and finally the fiber volume fraction c^f. These properties are passed to UMAT by ABAQUS in the array PROPS(NPROPS). In the input-file, the keyword *USER MATERIAL is used to specify material constants. In the present study, the fiber volume fraction is assumed to remain constant $c^f = 0.6$ throughout the deformation.

2.2.3 User Subroutine ORIENT

The ABAQUS user subroutine ORIENT is used for defining local material directions. In the kink band analysis described in the following section, parameters describing the geometry of the kink band are placed in a datafile which is being read from the ORIENT subroutine. In ORIENT these parameters, B, ϕ_m, α and β are subsequently used to calculate the initial local fiber direction. The subroutine is called by ABAQUS at the start of the analysis at each material point.

3 Results

The constitutive model described in the previous section has been used to simulate the formation of kink bands in fiber reinforced composites. It is important to note that here, the fibers are assumed elastic.

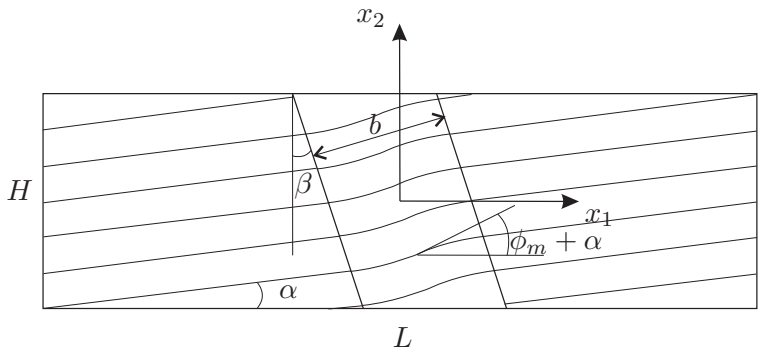

Figure 3: Kink Band Geometry.

The kink band geometry is sketched in Fig. 3. A block of material, see Fig. 2, is subject to compressive stresses under plane strain conditions. The block has the dimensions height $H = 3$ and length $L = 10$ and in a band of width b and at an angle β the direction of the fibers is given a small imperfection. The direction of the fibers outside the band is given by the angle α and inside the kink band the fibers are assumed to be at an angle ϕ, and this angle is given by the expression:

$$\phi\left(x_1, x_2\right) = \tfrac{1}{2}\phi_m \left[\cos\left(\frac{2\pi\cos\beta}{b}\left(x_1 + x_2\tan\beta\right)\right) + 1\right] + \alpha \qquad (23)$$

so that a small imperfection is added to the fiber angle α inside the band, and ϕ_m is the value of the imperfection in the middle of the kink band. Furthermore, the displacements u_1 and u_2 satisfy the boundary conditions

$$u_1 = 0 \quad \text{on} \quad x_1 = -\tfrac{L}{2} \qquad (24)$$

$$u_2 = 0 \quad \text{on} \quad (x_1, x_2) = \left(-\tfrac{L}{2}, -\tfrac{H}{2}\right) \tag{25}$$

In the following, the width of the kink band has the value $b = 2$, and in all simulations the fiber volume fraction is 0.6. Futhermore, analysis has been restricted to two different fiber/matrix stiffness ratios, $E^f/E^m = 35$ and $E^f/E^m = 100$, which qualitatively correspond to a glass-fiber reinforced polymer and a carbon-fiber reinforced polymer, respectively.

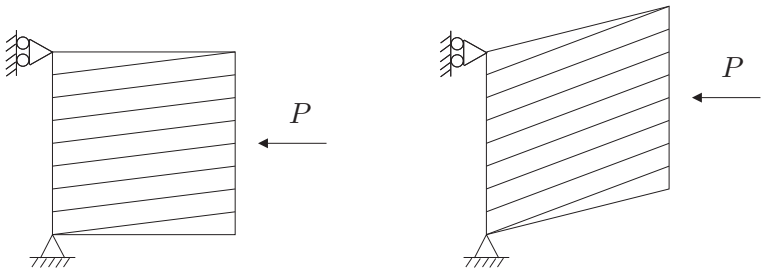

Figure 4: Deformation of a Single Element.

First of all, the deformation of a single element is investigated. The element is a 4 node plane strain element (CPE4) and the initial fiber angle is constant throughout the element. Load *vs.* displacement curves for one single element are shown in Fig. 5. Curves are shown for various angles α of the fiber misalignment and for the two different stiffness ratios of the fiber/matrix system. For sufficiently small fiber misalignments the response is linear until a critical load is reached after which material softening and snap-back behavior is observed.

The maximum loading capacity is summarized in Fig. 6. Even though both constituents are modelled as hardening materials, the composite shows extensive softening behavior after the maximum loading capacity is reached with snap-back behavior for small initial fiber inclinations as shown in Fig. 5. The snap-back behavior is in the finite element code ABAQUS modelled using the Riks method. In experimental measurements a snap-back material behavior would manifest as a dynamic material response. A detailed description of the Riks method can be found in Crisfield (1991).

The observed overall composite material softening which is required for strain localization in structural components is caused by an interaction of the non-linear response of the matrix material with an increasing rotation of the fibers during compression as indicated in Fig. 6. I.e., during compression, the block of material will, in addition to increasing axial compression, show an increasing shearing tendency in the direction of increasing fiber rotation. For the cases studied here, if the matrix material plasticity is suppressed so both composite constitutes follow a linear elastic material response, the fiber rotation itself does not cause material softening.

The development of the deformation of one element is further illustrated in Fig. 7. This figure shows the vertical displacement u_2 *vs.* the horizontal

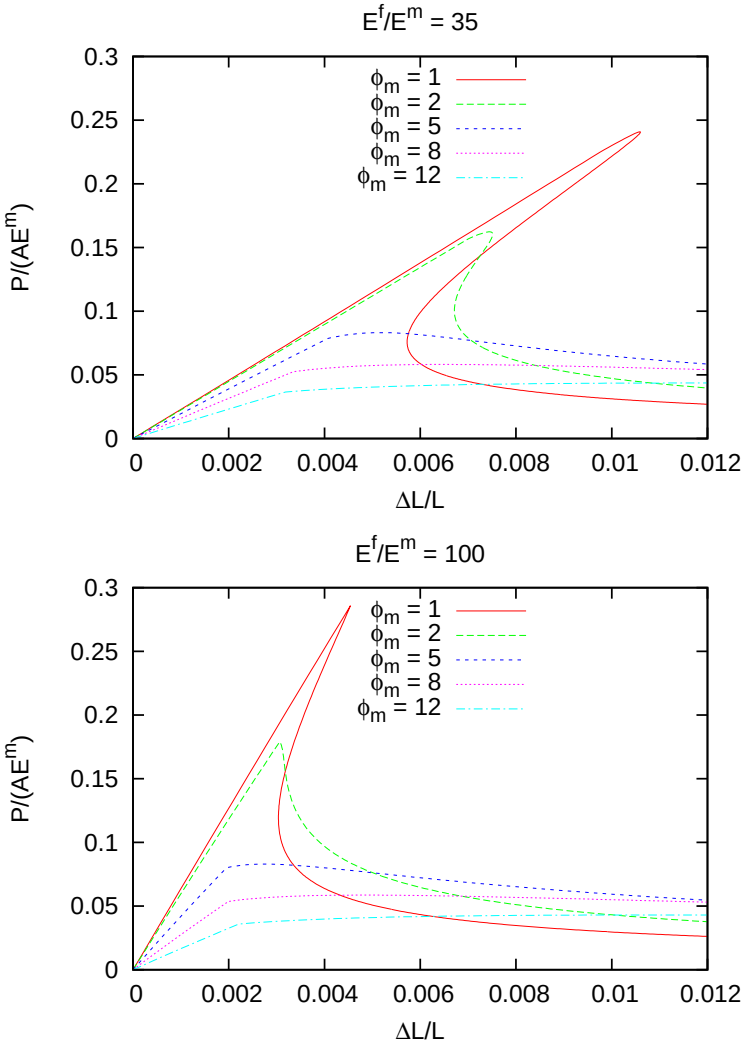

Figure 5: Plastic Deformation of 1 Element.

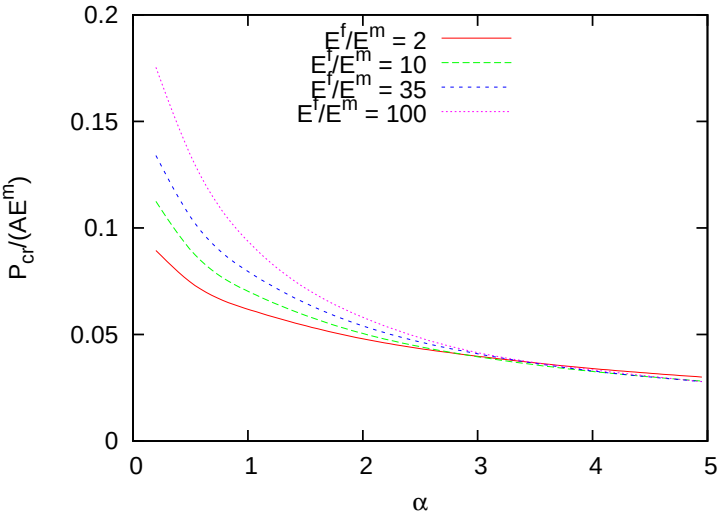

Figure 6: Peak Load, 1 Element.

displacement u_1 for node No. 2 (the lower right corner) in Fig. 4 for the case where the fiber angle is $\alpha = 1°$ and $E^f/E^m = 100$). The results show a shift in the direction of the displacement vector from initially equal amounts of the two displacement components towards displacement mainly in the vertical direction.

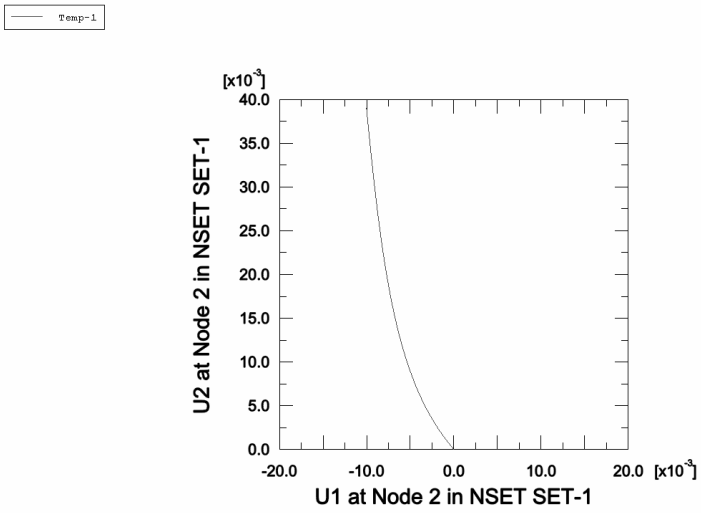

Figure 7: u2 *vs.* u1.

This concludes the study based on the performance of a single element. The following calculations are performed using at first 6*20 8-node plane

strain (CPE8) elements. In Fig. 8 normalized load *vs.* end shortening curves are shown for the low fiber to matrix ratio, i.e. glass fibers above and the high ratio, i.e. carbon fibers below. Calculations are carried out for different values of the fiber imperfection angle ϕ_m and outside the band the fibers are aligned with the x_1-axis, i.e. $\alpha = 0$. As also shown in previous studies, the peak load is highly sensitive to the misalignment of the fibers. At a sufficiently large imperfection angle, the peak load disappears and the composite fails by another mechanism. After the peak load material softening occurs and the curves eventually converge and the previous load history has insignificant effects.

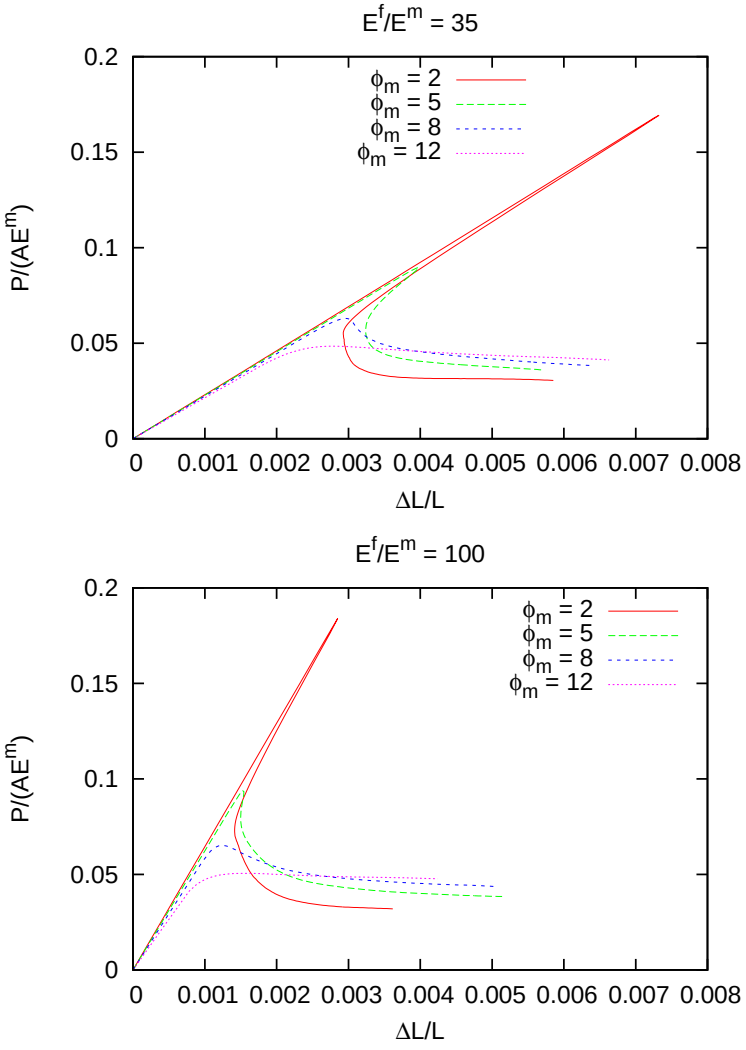

Figure 8: Plastic deformation, Kink Band Formation.

A contourplot of the plastic strain in the kink band for the case $E^f/E^m =$

35 is shown in Fig. 9. The figure shows the tendency for strains to localize into a band inclined relative to the load and fiber direction. The deformations remain almost homogeneous outside the localized band.

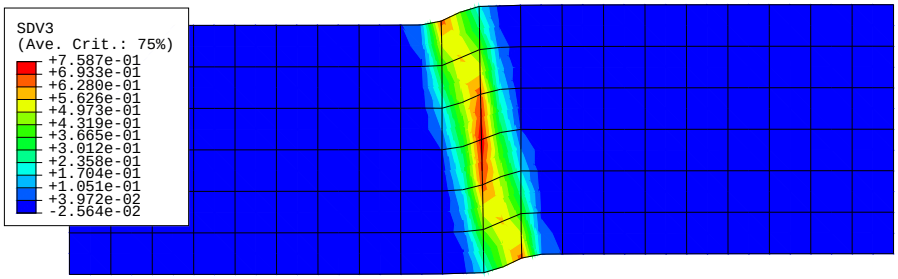

Figure 9: Contourplot of plastic strain.

The peak load is sensitive to a number of parameters. The sensitivity to the misalignment has been demonstrated and the non-linear response of the matrix material can also play a role. In Fig. 10 the load *vs.* end shortening curve is shown for a linear elastic response of the matrix, corresponding to $n^m = 1$.

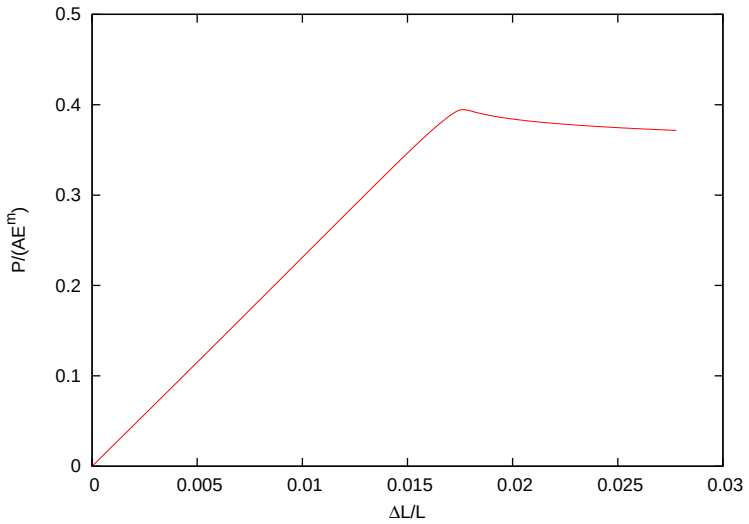

Figure 10: Load *vs.* end shortening curve. The matrix material is assumed to be linear elastic.

It is seen that a peak load results also in this case, and load *vs.* end shortening curves are shown in Fig. 11 for different values of the hardening exponent n^m for the matrix. In Fig. 10 and 11 a mesh consisting of 12*40 CPE8 elements is used, fiber imperfection angle is $\phi_m = 3^\circ$ and $E^f/E^m =$

35.

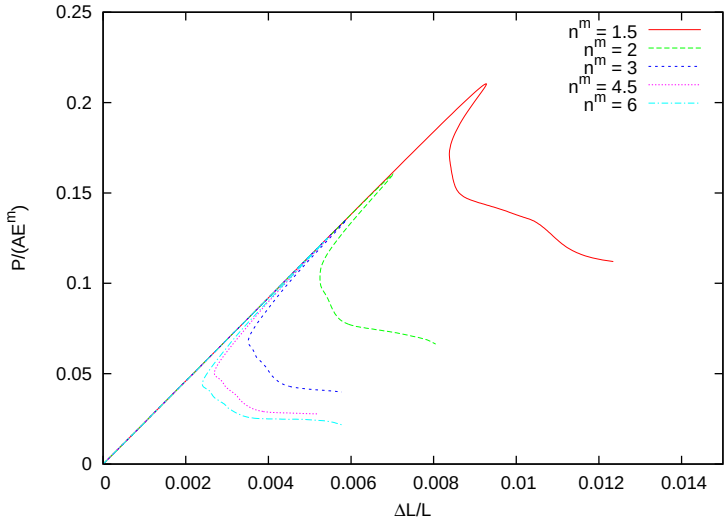

Figure 11: Load *vs.* end shortening curves for different values of matrix hardening parameter n^m.

The peak stress and the post critical response is seen to be sensitive to the hardening exponent in certain regimes. The peak stress as a function of the hardening exponent n^m and $\phi_m = 3^\circ$ is shown in Fig. 12, where the peak load initially drops by a large amount until convergence towards an elastic-perfectly plastic response of the matrix is achieved.

The peak load is less sensitive to the kink band inclination angle, β. In Fig. 13, the critical load as a function of β is shown for three different misalignment angles. The peak stress is seen to vary only moderately with the angle, β, while the angle ϕ_m plays a more significant role. Again, the mesh is 12*40 CPE8 elements.

The effect of the applied load not being in the same direction as the fibers is studied by changing the value of α. Load-deformation curves for various α are given in Fig. 14. The fiber angle is $\phi = 2^\circ$, $E^f/E^m = 35$ and the mesh consists of 6*20 CPE8 elements. It is seen that the snap-back effect only exists for small angles and that the load-deformation curves cease to have a peak value when the value of α increases.

A material length-scale is not included in the implementation of the constitutive model and as a consequence, the width of the kink band is undetermined and mesh dependent. As a result of this, the rate of convergence of load *vs.* end-shortening curves, see Fig. 15, with decreasing element size in the mesh is somewhat slow, especially in the immediate post kinking regime. The peak stress and the response far into the post critical regime seem to converge faster.

Fig. 16 shows contourplots of the effective plastic strain in the 4 different

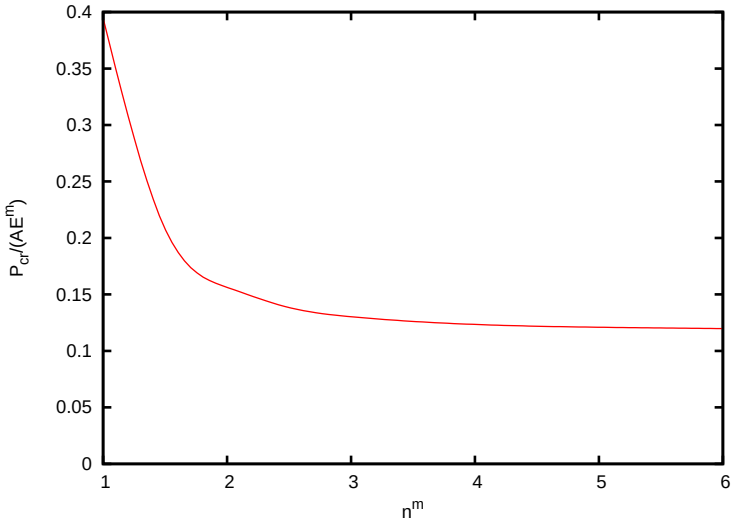

Figure 12: Peak load *vs.* hardening parameter n^m.

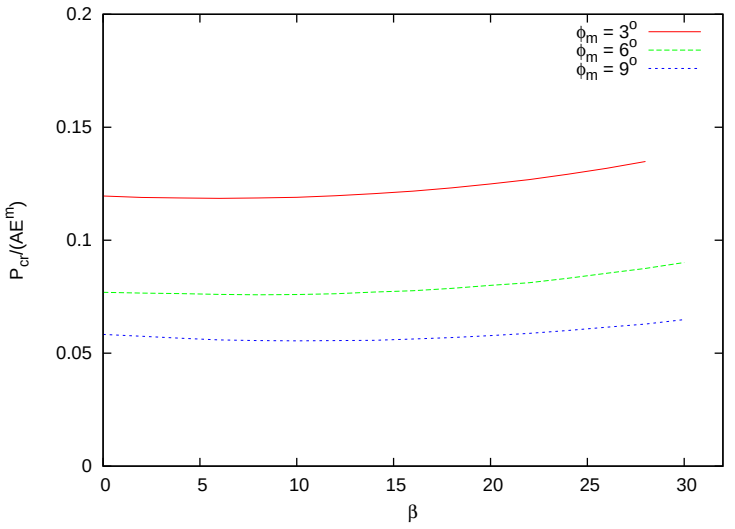

Figure 13: Peak load *vs.* β.

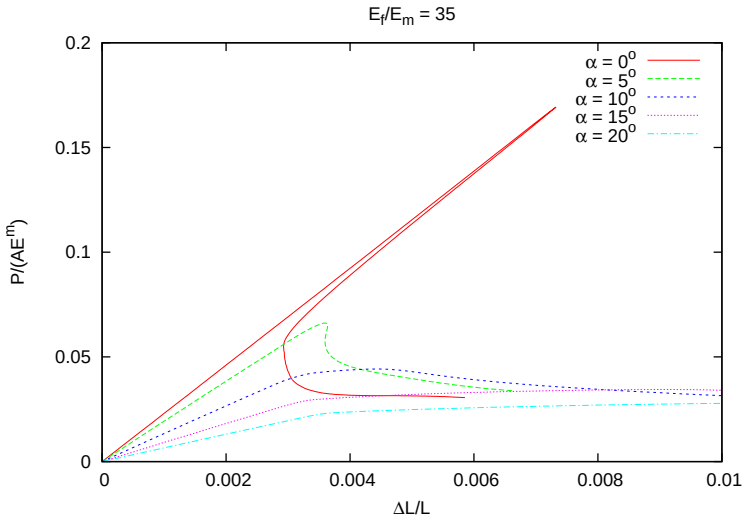

Figure 14: Load-deformation curves for various α.

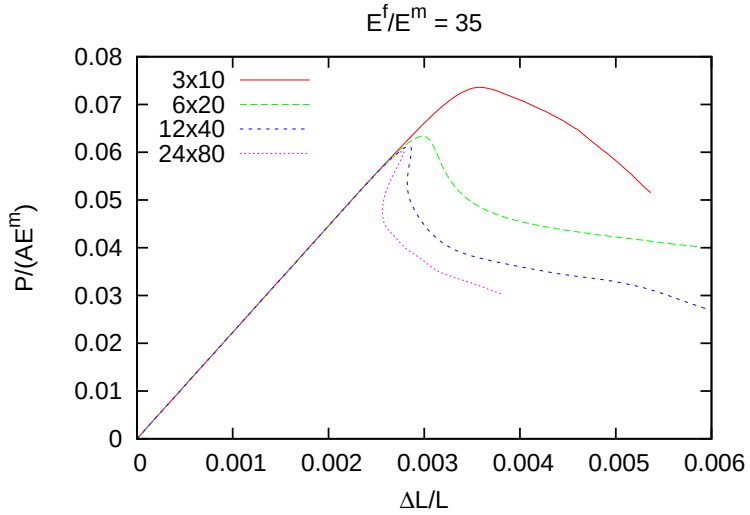

Figure 15: Load *vs.* end shortening curves for different element sizes.

meshes used in the mesh-dependency studies. It is seen how the width of the localized band decreases as the size of the elements decreases.

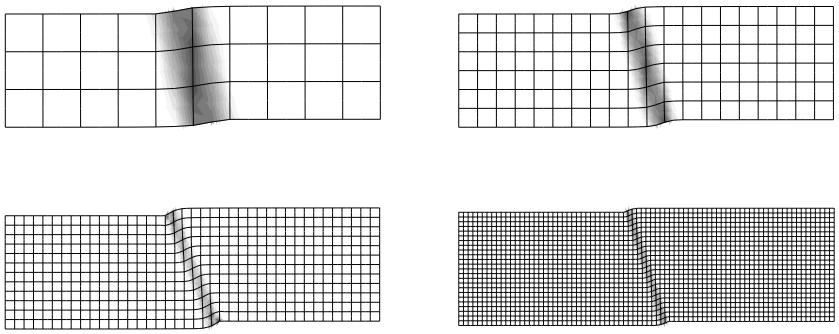

Figure 16: Four different deformed meshes with contour plot of effective plastic strains included.

Up until this point all results have been produced using a mesh consisting of rectangular elements. To investigate how a 'distorted' mesh affects the results, a mesh as shown in Fig. 17 is introduced. The elements (12*40 CPE8R elements) are aligned with the initial imperfection at an angle of $\beta = 8°$. The results are shown in Fig. 18 and Fig. 19 where the load-deformation curves for a 'regular' and a 'distorted' mesh are compared.

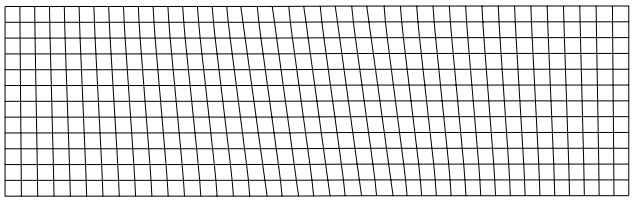

Figure 17: Distorted mesh.

In Fig. 18 the fiber angle is $\phi = 4°$ and $E^f/E^m = 35$, in Fig. 19 the fiber angle is $\phi = 5°$ and $E^f/E^m = 100$. The critical load is apparently unaffected by the change of the mesh but the immidiate post-kinking behavior is seen to be different.

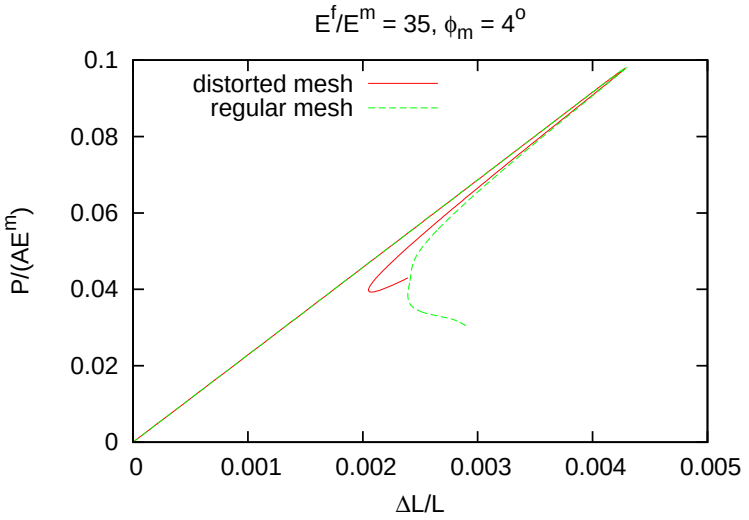

Figure 18: Load *vs.* deformation for regular and distorted mesh.

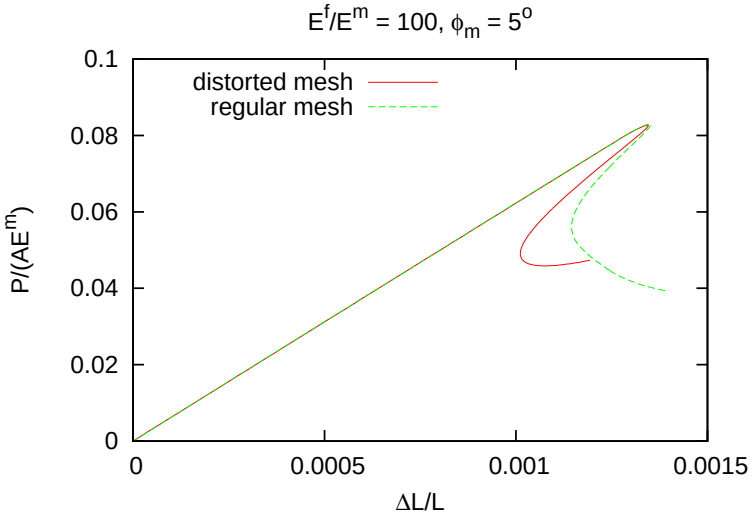

Figure 19: Load *vs.* deformation for regular and distorted mesh.

4 Discussion and Conclusion

A plane constitutive model for fiber reinforced composites has been implemented in ABAQUS as a user subroutine. The model has been tested under cases where failure by kink band formation is a relevant mechanism. At first it is verified that the model predicts a reasonable behavior for a single finite element. The behavior of a rectangular block of material divided into a number of finite elements is then investigated. The focus in this study is on the performance of the model when implemented in ABAQUS with respect to reliability and rate of convergence. In agreement with previous results, it is seen that the critical stress for kink band formation is rather insensitive to the initial kink band orientation and that the kink band undergoes a distinct rotation in the post critical regime. In the model, a continuous field may be specified for the initial fiber orientation. This field can vary with the spatial components to mimic real defects in the production of laminated structures. The imperfection of the composite material applied in the present study is an assumed band of material of a specified width in which the fiber orientation gradually changes from the orientation outside the band to a maximum deviation from this and back to the original orientation again. The band may be arbitrarily oriented relative to the fiber direction. No variation of fiber rotations has been assumed in the direction of the band although this is not a general restriction in the model.

The constitutive model has no intrinsic length scale and consequently the width of the kink band is undetermined and mesh dependent. As a result the rate of convergence of load *vs.* end-shortening curves with decreasing finite element mesh size is somewhat slow especially in the immediate post kinking regime. The peak stress and the response far into the post critical regime seem to converge faster. It is demonstrated that an initial alignment of the finite element mesh in the direction of the orientation of the kink band may have the effect of increasing the rate of convergence.

The model is applied in a study of the effect of initial misalignment of the fiber and load direction. This effect has previously been studied in an approximate manner by imposing a fixed linear combination of compressive and shear stresses out side the kink band. The effect of initial misalignments is very distinct on the peak stress where the critical stress at 10° misalignment is reduced to roughly 1/4 the critical stress for compression in the fiber direction at a fixed band of imperfections. At a misalignment of 15° and above the peak in the stress *vs.* end shortening response vanishes and the composite structure fails by another mechanism.

The model is expected to have some immediate applications such as kink band formation in plates with holes or other, more complex, structural components. Also, the model can be used to study competing compressive failure mechanisms such as buckling and kink band formation in fiber composite based structures.

Acknowledgements

The work has been financial supported by the Danish Technical Research Counsil through the project 'Interface Design of Composite Materials' (STVF fund no. 26-03-0160).

References

Argon, A.S. (1972). Fracture of composites. *Treatise on Material Science and Technology* **1**, 79–114. Academic Press, New York.

Budiansky, B. (1983). Micromechanics. *Computers and Structures* **16**, 3–12.

Christoffersen, J. and H.M. Jensen (1996). Kink band analysis accounting for the microstructure of fiber reinforced materials. *Mechanics of Materials* **24**, 305–315.

Crisfield, M.A. (1991). *Non-linear Finite Element Analysis of Solids and Structures*. John Wiley and Sons.

Dunne, Fionn and Nik Petrinic (2005). *Introduction to Computational Plasticity*. Oxford University Press.

Fleck, N.A. and B. Budiansky (1991). Compressive failure of fibre composites due to microbuckling. *Proc. 3rd Symp. on Inelastic Deformation of Composite Materials* pp. 235–273. Springer Verlag, New York.

Hsu, S.Y., T.J. Vogler and S. Kyriakides (1998). Compressive strength predictions for fiber composites. *Journal of Applied Mechanics* **65**, 7–16.

Jensen, H.M. and J. Christoffersen (1997). Kink band formation in fiber reinforced materials. *Journal of the Mechanics and Physics of Solids* **45**, 1121–1136.

Kyriakides, S., R. Arseculeratne, E.J. Perry and K.M. Liechti (1995). On the compressive failure of fiber reinforced composites. *International Journal of Solids and Structures* **32**, 689–738.

McMeeking, R.M. and J.R. Rice (1975). Finite-element formulations for problems of large elastic-plastic deformation. *International Journal of Solids and Structures* **11**, 601–616.

Pane, I. and H.M. Jensen (2004). Plane strain bifurcation and its relation to kinkband formation in layered materials. *European Journal of Mechanics and Solids* **23**, 359–371.

Rice, J.R. (1976). The localization of plastic deformation. In: *Theoretical and Applied Mechanics* (W.T. Koiter, Ed.). North-Holland, Delft. pp. 207–220.

Rosen, B.W. (1965). Mechanics of composite strengthening. *Fiber Composite Materials*. Am. Soc. Metals Seminar, Ch.3.

Slaughter, W.S., N.A. Fleck and B. Budiansky (1993). Compressive failure of fiber composites: The roles of multiaxial loading and creep. *Journal of Engineering Materials and Technology* **115**, 308–313.